Exploration of Europa's Interior Using Electromagnetic Induction

Inaugural-Dissertation

zur Erlangung des Doktorgrades
der Mathematisch-Naturwissenschaftlichen Fakultät
der Universität zu Köln

vorgelegt von

Jason Winkenstern

aus Gelsenkirchen

Köln
2025

Berichterstatter:	Prof. Dr. Joachim Saur
(Gutachter)	Prof. Dr. Bülent Tezkan
Tag der mündlichen Prüfung:	07.02.2025

"O second moon, we, too, are made
of water, of vast and beckoning seas."
- Ada Limón

Abstract

Jupiter's icy satellite Europa is expected to host a global subsurface ocean underneath its icy crust. This notion was supported by magnetic field measurements, in which the electromagnetic response of Europa to Jupiter's magnetic field has been discovered. Since then, magnetic field measurements have been used to probe Europa's interior, as its induction response is a function of the ocean's depth, thickness, and electrical conductivity. While Europa's subsurface ocean is commonly modelled as a radially symmetric layer, it is expected to be asymmetric in nature, both on a global scale due to tidal deformation, but also on local scales due to fractures and partial water melt in the icy crust.

In this work, we investigate the detectability of water melt entrapped inside Europa's icy crust with magnetic sounding. For that, we first construct an analytical, iterative approach to solve the coupled induction between the global ocean and a local water reservoir. We find that the reservoir is strongly coupled to the ocean, i.e., its induction response to the ocean's induced dipole must be considered to accurately describe the overall induction response of the ocean-reservoir system. The ocean is weakly coupled to the reservoir, i.e., we can neglect its induction response to the reservoir's dipole within our prescribed precision. In this study, two scenarios are considered, a hypothetical flyby at 25 km altitude above Europa's surface and measurements directly at the surface. At 25 km altitude, reservoirs are not expected to be detectable, as their small induction signature falls off rapidly and could be obscured by small-scale fluctuations arising from plasma interactions in Europa's vicinity. At the surface, reservoirs could be detected by employing a network of at least two magnetometers, where one is placed directly above the region of interest, and a second right outside that region to resolve the spatial variability of the reservoir's induction response. Assuming a detectability limit of approximately 2 nT, derived from the strength of the small-scale fluctuations in magnetic field measurements, reservoirs with a radius larger than 8 km can be resolved, assuming a conductivity of 30 S/m. At larger radii, the necessary conductivity decreases, with 5 S/m required for a 20 km reservoir. Since the measurements would be taken at a fixed position, measuring over a long time period could allow us to better resolve periodic signals such as the reservoir's induction

response, potentially enabling the detection of smaller and less conductive reservoirs.

The characterization of Europa's subsurface ocean with electromagnetic induction results in a fairly unconstrained parameter space. This is partially due to the non-uniqueness of the induction method itself, but also due to the complexity of Europa's magnetic field environment, which is additionally perturbed by plasma interactions between the Jovian magnetosphere and Europa's atmosphere. In addition, the magnetospheric field of Jupiter along the spacecraft's trajectory is not exactly known, resulting in an unknown 'background' that is perturbed by the ocean's induction response and the plasma interactions.

The second part of this thesis characterizes the uncertainties originating from the individual models for the inducing field, the plasma interaction, and the Jovian background field. These uncertainties propagate into the ocean's properties, restricting our ability to constrain the parameter space span by the ocean's depth, thickness, and electrical conductivity. We perform a chi-squared analysis, in which the squared deviation between the modelled magnetic field and the observed magnetic field is weighted against the model uncertainty. From this approach, uncertainties of the ocean properties are derived in the form of a range, i.e., we provide upper and lower limits for the depth, thickness, and conductivity. As this method cannot provide a lower limit on the ocean's depth, additional constraints from crater simulations are taken into account, with a minimum depth of 20 km. Here, we find a minimum conductivity of 0.45 S/m and a minimum thickness of 3.5 km. No upper limit of the conductivity or thickness could be resolved with the induction method, as the induction amplitude eventually reaches saturation. For the depth, our analysis yields an upper limit of approximately 90 km, above which the induction response generated within the ocean does not appropriately reproduce the observations.

In addition, the robustness of the method is tested. For that, we apply small changes to individual model parameters and compare the resulting limits against the reference model. Here, we find that the interval length used to calculate the polynomial fit to the Jovian background field has the most noticeable effect on the resulting limits on the ocean properties. This notion emphasizes the relevance of the background fit in the exploration of Europa's subsurface ocean with electromagnetic induction.

Contents

List of Figures

List of Tables

1

Introduction

The Jovian satellite Europa is a primary target for the study of ocean worlds. Harbored below its icy surface layer, the moon is expected to host a global subsurface ocean of liquid water. This discovery was made during the Galileo mission, a spacecraft that was in Jupiter orbit from 1995 to 2003 and performed multiple close encounters (flybys) at Europa, as well the other Galilean satellites — Io, Ganymede, and Callisto. The spacecraft was, among other instruments, equipped with a magnetometer, which continuously measured the magnetic field along the spacecraft's trajectory. In the direct vicinity of Europa, the spacecraft measured strong perturbations in the magnetic field, which have been attributed to interactions between the icy satellite and its host planet. Primarily, an electromagnetic response is generated in a shallow, electrically conducting layer below the surface, for which the only appropriate geological interpretation is a saline subsurface ocean (Kivelson et al., 1997, 1999, 2000). In addition, plasma interactions between the Jovian magnetosphere and Europa's atmosphere further perturb the magnetic field environment (Neubauer, 1998). Similar perturbations have been measured around Callisto (Khurana et al., 1997), Ganymede (Kivelson et al., 1996a)[1], as well as Io (Kivelson et al., 1996b), making the Jovian system a crucial example of moon-magnetosphere interactions.

The principle of electromagnetic induction has since then been used to characterize Europa's interior, as the induced magnetic field is a function of the ocean's properties, i.e., its depth, thickness, and electrical conductivity (e.g., Parkinson, 1983; Saur et al., 2009). Early studies used simple models for Europa's interior, assuming spherical symmetry, and suggested only qualitatively derived constraints, i.e., visually from fitting an induced field to the data, for the ocean's properties (Zimmer et al., 2000; Schilling et al., 2007). The values estimated in these studies result in a fairly unconstrained parameter space, leaving Europa's interior structure an open question to this day. Since then, quantitative methods to constrain Europa's subsurface ocean have been developed (Biersteker et al., 2023;

[1] Ganymede additionally has its own intrinsic magnetic field.

Petricca et al., 2023). Further development to model Europa's interior was done by Styczinski et al. (2022), who introduced a solution to describe the electromagnetic response of a subsurface ocean with variable outer radius, i.e., an icy crust with variable thickness that is likely to exist due to longitudinal and latitudinal variations in tidal heating (Tobie et al., 2003). Additional irregularities from the spherically symmetric model can occur due to localized melt in Europa's icy crust, creating small water reservoirs which are suggested to be involved in the formation of surface disruptions (Schmidt et al., 2011), as well as tentative cryovolcanism (Sparks et al., 2017; Lesage et al., 2020).

In this work, we investigate whether liquid water reservoirs entrapped in Europa's icy crust can be detected using the principle of electromagnetic induction. For that, we first describe the Jovian magnetosphere and its icy satellite Europa in Chapter 2, providing the necessary information to further motivate our research and put it into context with the current state of the knowledge about Europa. In Chapter 3, we introduce the theoretical framework of electromagnetic induction that is required to understand the method and the results. There, we also present an analytical approach that has been developed to describe the coupling feedback introduced by two neighboring conductors, such as is the case for our model of Europa's interior, where we assume a radially symmetric, global subsurface ocean accompanied by a separate, spherical reservoir of liquid water. Chapter 4 presents the study published in Winkenstern and Saur (2023). There, we first highlight the physics of a coupled induction system and the coupling strength between Europa's ocean and a reservoir. Afterward, we investigate the detectability during a hypothetical flyby at 25 km altitude, as the Europa Clipper spacecraft will perform multiple flybys at that altitude during its tour. We additionally study the detectability at the surface, motivating a potential lander mission on Europa.

The second part of this thesis, Chapter 5, presents a study in which quantitative constraints of the ocean properties are derived. For that, we perform an inversion to fit the modelled magnetic field to spacecraft observations, where we use the uncertainties introduced by the models to describe the individual contributions to Europa's magnetic field environment — the Jovian background field, the ocean's induction response, and the magnetic field due to plasma interaction at Europa. We present estimates for the three considered model uncertainties and perform a chi-squared analysis within a prescribed 3D parameter space of ocean depth, thickness, and conductivity, which weights the squared deviation between the modelled and observed magnetic field against the overall uncertainty. Finally, we present and discuss the resulting constraints, providing additional context with existing estimates for the ocean depth derived from other techniques. Chapter 6 closes this thesis with concluding remarks.

2

Europa and the Jovian System

Jupiter's icy moon Europa is the second innermost Galilean satellite. This group of four natural satellites was discovered by Galileo Galilei and Simon Marius independently in 1610. They are the four largest satellites of Jupiter and, with increasing orbital distance, named: Io, Europa, Ganymede, and Callisto. With a mean radius of $R_\mathrm{E} = 1561\,\mathrm{km}$ (Nimmo et al., 2007), Europa is the smallest of the Galilean satellites. It resides at an orbital distance of approximately 9.4 Jupiter radii R_J (Jupiter's equatorial radius $R_\mathrm{J} = 71492\,\mathrm{km}$), and is thus embedded in Jupiter's inner magnetosphere. Europa responds to the time-varying component of Jupiter's magnetospheric field in the form of electromagnetic induction. Additionally, Europa is continuously bombarded by energized ions and electrons that populate the magnetosphere, causing surface weathering, as well as ionizing its atmosphere. Capturing the physics of these interactions is pivotal to our understanding of Europa. In this chapter, the Jovian magnetosphere will be introduced, especially with regard to its influence on Europa. Afterward, we will describe the current understanding of Europa's atmosphere and surface. Finally, we will present the current knowledge on Europa's interior, putting an emphasis on the extent of its outer H_2O layer and the partition into frozen and liquid parts.

2.1 Jupiter's Magnetosphere

Jupiter is the source of the largest planetary magnetosphere in the solar system. At an orbital distance of $5.9\,R_\mathrm{J}$, Io acts as the strongest plasma source within the Jovian magnetosphere (Bolton et al., 2015), producing ions of its SO_2 atmosphere, such as S^+, S^{++}, O^+, and more. This ion population forms the Io plasma torus, which corotates with the Jovian magnetosphere and constantly sweeps over Io (Bagenal, 1994). However, parts of that population move radially outward, which results in iogenic material populating the entire magnetosphere (Saur et al., 2004), eventually forming the Jovian plasma sheet around the magnetic equator. At Europa's orbital distance, the plasma sheet is trapped near the centrifugal equator, which is tilted by approximately 7° with respect to the rotational equator (Bagenal & Dols, 2020).

The dipole component of Jupiter's intrinsic field is tilted by 10.25° with respect to its rotational axis (Connerney et al., 2022). In Europa's rest frame, Jupiter and its magnetic field rotate with a period of $T = 11.23\,\mathrm{h}$, compared to Europa's orbital period of approximately 85 h. This means that, similar to Io, Europa's trailing hemisphere is constantly bombarded by the ambient plasma environment. Furthermore, Europa's distance to the plasma sheet oscillates throughout one synodic rotation period. This varying plasma environment has an effect on Europa's magnetic field environment, and strong magnetic field anomalies near the plasma sheet are likely to obscure magnetic field perturbations generated within Europa, i.e., in its subsurface ocean (e.g., Kivelson et al., 1997).

2.2 Europa

Here, we introduce the icy satellite Europa and review the current state of the research that is relevant to understand the motivation of our research presented in this thesis. For that, we first cover Europa's atmosphere, moving inward to surface observations and information about its interior thereafter. We emphasize the information retrieved from electromagnetic induction, as that is the method with which we aim to study Europa's interior.

2.2.1 Europa's Atmosphere

Through HST observations in the ultraviolet (UV) an oxygen atmosphere at Europa has been detected with molecular oxygen O_2 being the dominant species (Hall et al., 1995). The observed emissions at 130.4 nm and 135.6 nm result from electron-impact dissociation, originating from magnetospheric electrons bombarding Europa's atmosphere. Further HST observations of the trailing hemisphere revealed a stable H_2O atmosphere around the subsolar point (Roth, 2021). Cervantes and Saur (2022) combined these HST observations with magnetometer measurements recorded during Galileo's E12 flyby to constrain Europa's atmosphere, yielding column densities of $1.2 \cdot 10^{14}\,\mathrm{cm}^{-2}$ for O_2 and $1.5 \cdot 10^{15} - 2.2 \cdot 10^{15}\,\mathrm{cm}^{-2}$ for H_2O.

Europa's O_2 atmosphere is non-uniform across its global structure. An asymmetry between Europa's leading and trailing hemisphere has been observed (Hansen et al., 2005), shaped by the plasma interactions between the icy moon and the Jovian magnetosphere. Plainaki et al. (2013) demonstrate a spatial variability of Europa's O_2 atmosphere based on solar illumination, as a higher surface temperature around the subsolar point increases the yield of released O_2. Such a day-night asymmetry has also been used in a study by Addison et al. (2024) to describe the magnetic field measurements during Juno's only flyby at Europa in September 2022. However, their model suggests a significantly weaker atmosphere on the night side, with a column density in the order of $10^9\,\mathrm{cm}^{-2}$. It is worth noting that this study does not consider electron beams which have been detected during the flyby and further perturb the magnetic field (Allegrini et al., 2024).

Local variabilities in atmospheric densities could exist in the form of water vapor plumes, releasing additional material into Europa's atmosphere. Local enhancements of line emissions in the UV above Europa's limb have been implied to result from plume activity. Such events, however, were not present in every considered HST campaign (Roth et al., 2014; Sparks et al., 2016). Strong, local magnetic field perturbations measured with the Galileo spacecraft were discussed to arise from a putative plume crossing during the E12 flyby (Jia et al., 2018), as well as the E26 flyby (Blöcker et al., 2016; Arnold et al., 2019). Outgassing of endogenic material has been discovered to occur on Saturn's icy satellite Enceladus (Hansen et al., 2006). Plume activity on Europa is of great interest due to the direct link to the subsurface ocean's composition, marking one of the science goals of the Europa Clipper mission (Pappalardo et al., 2024).

2.2.2 Surface Observations

Images of Europa's surface in the visible spectrum, for example Figure 2.1, reveal a vast number of geological features, which can be categorized into geological units (e.g., Greeley et al., 2000; Leonard et al., 2018). One striking unit are curvilinear bands with a darker appearance, likely due to a higher concentration of non-ice material compared to the surrounding surface (Leonard et al., 2024). These bands are expected to form as the icy surface is pulled apart, owing to lateral surface motions analogous to plate tectonics on Earth (e.g., Smith et al., 1979; Collins et al., 2022).

In an environment completely shielded from external processes, the upwelling of endogenic material due to fractures in the ice would enable us to infer the composition of Europa's subsurface ocean[1]. However, the bombardment of Europa's surface with electrons and iogenic ions drives radiolytic processes, in which the surface material is broken down and new compounds are formed (Carlson et al., 1999). This surface weathering imposes a challenge on the ability to conclusively interpret surface measurements in an interior context.

Another distinct feature observable on Europa's surface are chaos regions (Figure 2.2). These areas of heavily disrupted ice stick out from their surrounding surface due to their exhibited topography. Together with band material, they form the two dominating geological units on Europa (Greenberg et al., 1999). The formation mechanism is not exactly known. Initial theories suggested a melt-through model, where non-uniform tidal heating causes localized thinning of the icy crust overlying Europa's subsurface ocean, creating a surface depression above the local melt. The icy crust can then melt completely, exposing a liquid layer to the surface, which eventually refreezes, causing the surface to rise again and create a dome-shaped structure (Greenberg et al., 1999). Other models for the formation of chaos regions include cryovolcanism (Greeley et al., 1998), as well as local water melt entrapped within Europa's icy crust (Schmidt et al., 2011). Even though the

[1] A thorough introduction to Europa's subsurface ocean and its discovery will follow in Section 2.2.3.

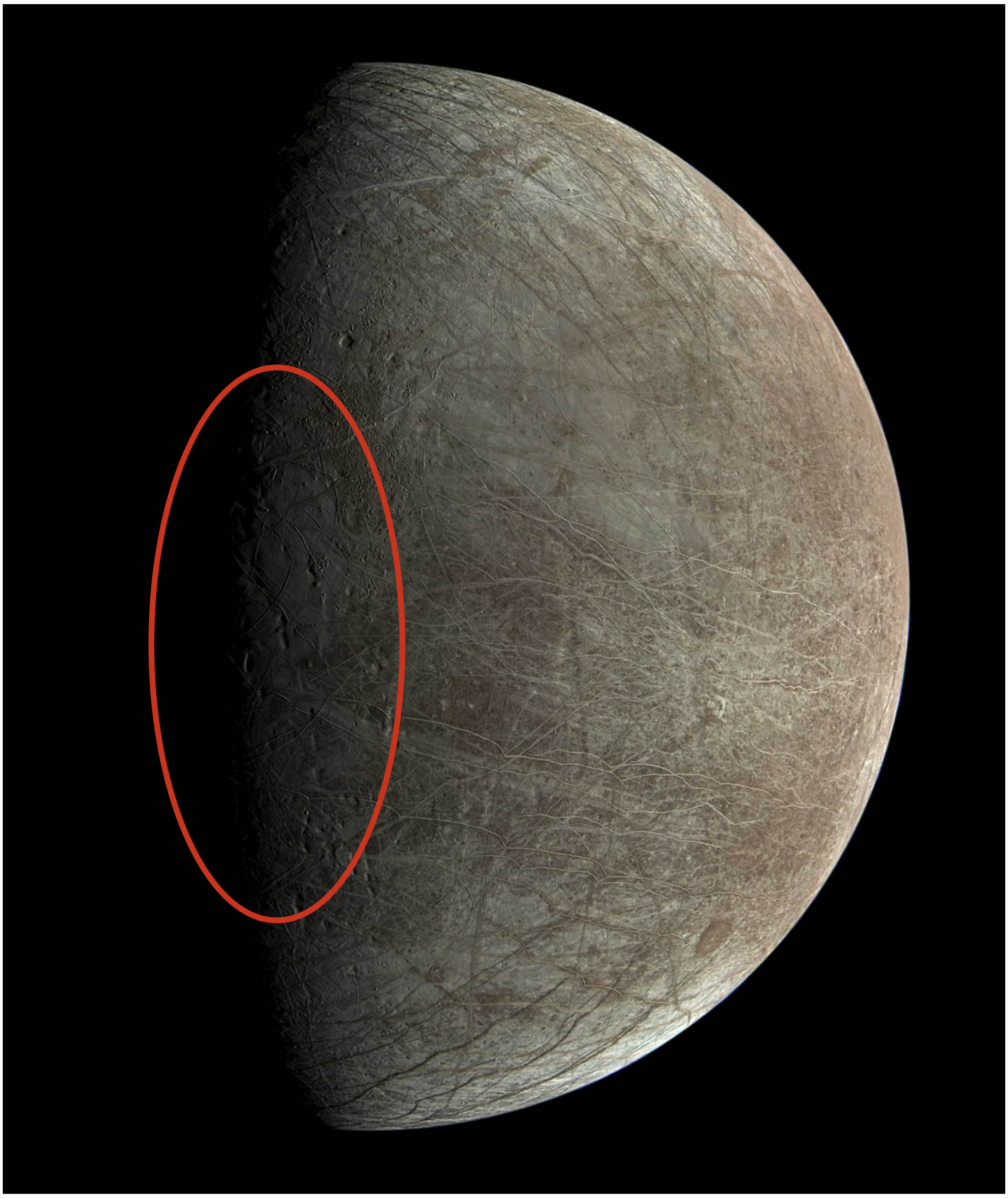

Figure 2.1: Image of Europa taken by the JunoCam at an altitude of 1521 km. Dark bands cover Europa's surface, possibly owing their color to radiolysis of endogenic material that has been exposed to the surface during the formation of these curvilinear structures. At the day-night boundary, Annwn Regio can be seen, roughly enclosed in the red ellipse. This large-scale chaos region could potentially have formed above a shallow source of liquid water, i.e., in the form of entrapped water melt. The dark circular spot at the bottom right is the Callanish crater. North is upward. Credit: NASA / JPL-Caltech / SwRI / MSSS / Björn Jónsson

precise mechanism is not known, all proposed models agree on the potential exposure of endogenic material during the formation of chaos.

Inferred from near-infrared absorption spectra, a magnesium sulfate dominated interior has been suggested in early studies (McCord et al., 1998; Dalton et al., 2005). It was, however, argued that the observed sulfur bearing compounds are a result of iogenic sulfur impinging on Europa's icy surface, thus not being representative of endogenic material (Brown & Hand, 2013). Observations made with the Space Telescope Imaging Spectrograph installed on HST show a distinct absorption feature at 450 nm, mapping to large-scale chaos regions on Europa's leading hemisphere (Trumbo et al., 2019). This absorption feature is in agreement with laboratory measurements of irradiated NaCl at 100 K (Poston et al., 2017). As the detection of NaCl occurred on leading hemisphere chaos, shielded from the plasma bombardment on Europa's trailing hemisphere, it was concluded that NaCl is of endogenic origin and potentially the dominant species in Europa's subsurface ocean. Understanding the composition of Europa's subsurface ocean is an important question in today's research, as various saline, aqueous solutions have different electrical conductivities at the same salinity. Knowing the constituents that drive the electrical conductivity of Europa's ocean would thus narrow down the range of possible salinities for a given electrical conductivity inferred from magnetic sounding.

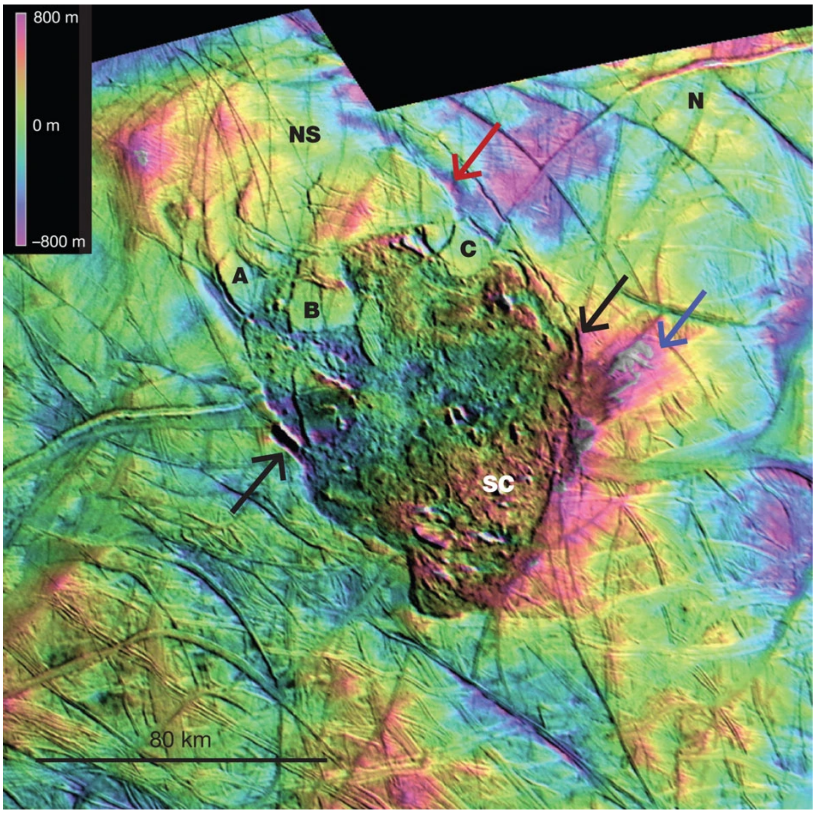

Figure 2.2: Topography of the Thera Macula chaos region as shown in Schmidt et al. (2011), Figure 2. This image highlights the irregularity of chaos regions compared to the surrounding plains material.

The recent detection of CO_2 with the James Webb Telescope NIRSpec (Near-Infrared Spectrograph) coincides with the presence of young chaos regions on Europa's leading hemisphere, indicating an internal source of carbon (Trumbo & Brown, 2023; Villanueva et al., 2023). Whether the carbon already exists as CO_2 or any other, potentially organic, material, cannot be decisively concluded from the measurements. There was, however, no significant detection of organics in the NIRSpec data. The detection of carbon bearing material is of great astrobiological interest due to carbon being a keystone to life as we know it (Catling, 2013). In addition, CO_2 can increase the electrical conductivity of Europa's subsurface ocean (Castillo-Rogez et al., 2022).

2.2.3 Europa's Interior

In the 1990s, the Galileo spacecraft entered the Jupiter system, performing multiple close encounters at Europa and the other Galilean satellites. Gravitational measurements, supported by Earth-based radio measurements using the Deep Space Network, found a differentiated subsurface composed of an outer H_2O shell and an underlying silicate mantle. This H_2O shell extends down to $80 - 200\,\mathrm{km}$, however, a distinction between frozen and potentially liquid parts was not possible on the basis of these measurements alone (Anderson et al., 1998). Galileo's magnetometer recorded crucial data to improve our understanding of Europa's interior. As Galileo passed by Europa, large perturbations were measured in the otherwise slowly changing magnetic field of the Jovian magnetosphere. In particular, these perturbations were strongest around the time of closest approach (Figure 2.3). As Jupiter rotates, its magnetic field will change its orientation with respect to Europa. These temporal variabilities induce eddy currents in a conductive layer, which in turn generate a secondary magnetic field, also referred to as induced magnetic field or induction response. In Europa's case, the only geological interpretation for these perturbations is a shallow, saline subsurface ocean (Khurana et al., 1998; Kivelson et al., 1999). The existence of an intrinsic magnetic field has been ruled out when Galileo went into its extended mission and performed a flyby at Europa where the orientation of the background field was in anti-phase relative to the E04 and E14 flybys (Kivelson et al., 2000). Induced magnetic fields are also generated in Europa's putative iron core, their surface strength however is an order of magnitude smaller than the ocean's induced magnetic field in the presence of a conductive ocean (Seufert et al., 2011).

Galileo's magnetometer measurements provided strong evidence for the existence of a global subsurface ocean below Europa's icy crust. Since the quantities governing the induced field, induction amplitude A and phase shift ϕ^{ph}, are functions of the ocean's depth d, thickness h, and electrical conductivity σ, magnetic field measurements can be used to probe Europa's interior, specifically its ocean. Although this method has been used in several studies, the characteristics of Europa's ocean remain not fully constrained. Zimmer et al. (2000) provided a lower limit for the ocean's induction amplitude of $A \geq 0.7$, equalling to a conductivity $\sigma \geq 0.06\,\mathrm{S/m}$, assuming Europa's ocean is directly at the surface. Schilling et al. (2007) constrained the conductivity to be larger than $0.5\,\mathrm{S/m}$, assuming an ocean with $100\,\mathrm{km}$ thickness below a $25\,\mathrm{km}$ thick icy crust. For a thin ocean, $h = 25\,\mathrm{km}$, they concluded that conductivities above $1\,\mathrm{S/m}$ are required. An upper limit

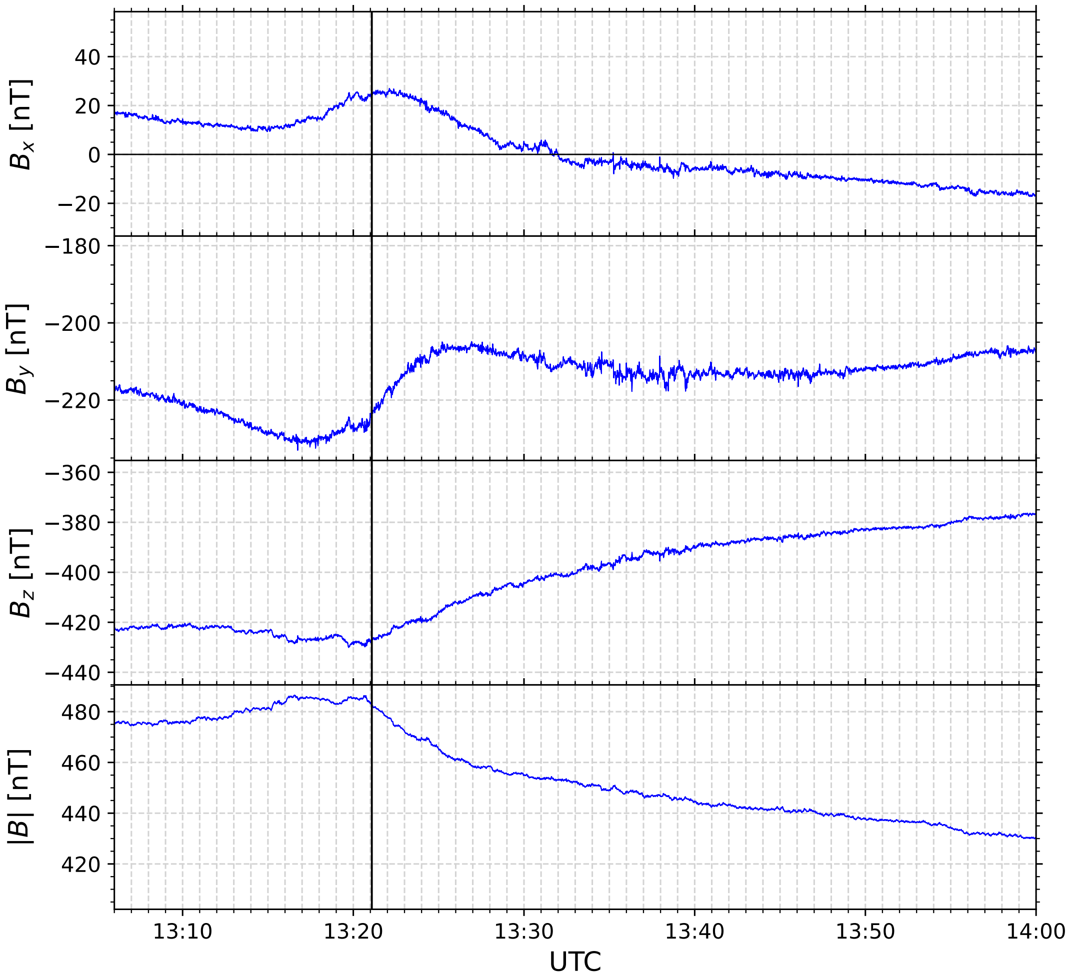

Figure 2.3: Magnetometer measurements for Galileo's E14 flyby. The magnetic field components are given in EPhiO coordinates, where z is parallel to Jupiter's rotation axis, y points toward Jupiter in a plane perpendicular to z, and x completes the right-handed system (approximately aligning with corotational flow). The vertical black line indicates the time of closest approach (C/A), which occurred at an altitude of 1648 km.

on the conductivity cannot be derived from the measurements, as the induction amplitude goes into saturation at approximately 5 S/m. It is worth noting that these constraints are derived visually from fitting induction models with various input parameters to the measurements. Schilling et al. (2004) performed a joint inversion of four Galileo flybys, suggesting an induction amplitude of $A = 0.98 \pm 0.02$. The given uncertainty does not consider model uncertainties and is likely an underestimation. Quantitative claims about the ocean's characteristics, especially about their uncertainty or range, require us to consider the uncertainties of the various components included in the modelled magnetic field (see Chapter 5).

Aside from magnetic sounding, other methods are used to estimate the ocean's depth. Modelling the tidal heating Europa experiences due to its eccentric orbit yields an ice shell thickness ranging from 12-25 km (Tobie et al., 2003; Walker & Rhoden, 2022). Impact craters on Europa's surface provide additional estimates on the icy crust's thickness, as the formation of certain crater features, such as central peaks, depends on whether the impactor reached the ocean. A study of the depth-to-diameter slope shows that Europa's icy crust is at least 19-25 km thick (Schenk, 2002). Simulation of impact craters provide a significantly lower limit of 4 km (Turtle & Pierazzo, 2001). A recent study focussed on Europa's two multiring basins, Callanish and Tyre, and simulated impacts that would form such craters, stating that the icy crust's thickness must be above 20 km to reproduce the observed structures (Wakita et al., 2024).

3

Electromagnetic Induction

In this work, Europa's magnetic field environment is used as a window into its interior. In particular, the electromagnetic responses of Europa's subsurface ocean, as well as putative water reservoirs within its icy crust to Jupiter's magnetic field, are of interest. This chapter provides the theoretical background of electromagnetic induction. In the following, the induced magnetic fields of two neighboring conductors will be considered. In such a scenario, a coupling feedback between the two conducting bodies occurs, for which an analytical approach has been developed. After presenting our approach to describe coupled fields, we shortly discuss the numerical implementation with regard to the precision of this method.

3.1 Fundamentals

This section provides the necessary tools to describe magnetic fields. Here, the description differs between conducting bodies with finite conductivity $\sigma \neq 0$ and insulating medium with $\sigma = 0$. At the boundary between two layers of varying conductivity, certain conditions must be applied to ensure physical validity of the magnetic field description across the entire domain. These boundary conditions will be presented for the models considered in our work. From the resulting boundary equations, a relationship between the inducing and induced field can be derived. In particular, this relation governs the induction amplitude A and phase shift ϕ^{ph} of the induced field.

3.1.1 Induction Equation

Electromagnetic induction describes the generation of electric fields $\mathbf{E}$ driven by time-varying magnetic fields $\mathbf{B} = \mathbf{B}(t)$. This statement is described by Faraday's law

$$\nabla \times \mathbf{E} = -\dot{\mathbf{B}}. \tag{3.1}$$

In a medium with electrical conductivity $\sigma \neq 0$, the resulting currents generate magnetic fields, as described by Ampere's law

$$\nabla \times \mathbf{B} = \mu_0 \mathbf{j} + \frac{1}{c^2}\dot{\mathbf{E}}, \tag{3.2}$$

where $\mathbf{j}$ are the electric currents and c is the speed of light in vacuum. Assuming that the conductivity is isotropic and constant, Ohm's law can be written in its simplest form as

$$\mathbf{j} = \sigma \mathbf{E}. \tag{3.3}$$

Further writing the time-variable part of the electric field as $\mathbf{E}(\mathbf{r}, t) = \mathbf{E}(\mathbf{r})e^{-i\omega t}$, Ampere's law can be rewritten as

$$\nabla \times \mathbf{B} = \left(\mu_0 \sigma - i\frac{\omega}{c^2}\right)\mathbf{E}. \tag{3.4}$$

This form of Ampere's law assumes the relative magnetic permeability μ_r to be approximately one, which holds for most para- and diamagnetic materials, so that $\mu = \mu_r \mu_0 \approx \mu_0$. The RHS of Equation (3.2) is composed of conductive and displacement currents. The latter arises from temporal variabilities in the electric field and can be neglected if the following inequality holds

$$\omega \ll \mu_0 \sigma c^2. \tag{3.5}$$

In Europa's rest frame, Jupiter's magnetic field is rotating at a period of $T = 11.23\,\text{h}$, equivalent to Jupiter's synodic rotation period. Thus, for conductivities $\sigma \gg 10^{-15}\,\text{S/m}$, the displacement currents can be neglected. The expected conductivity of Europa's subsurface ocean is orders of magnitude above that lower limit. With this approximation, Ampere's law reduces to

$$\nabla \times \mathbf{B} = \mu_0 \sigma \mathbf{E}. \tag{3.6}$$

By taking the curl, we can plug in Faraday's law to the RHS of the equation

$$\nabla \times [\nabla \times \mathbf{B}] = -\mu_0 \sigma \dot{\mathbf{B}}. \tag{3.7}$$

We can use the vector identity $\nabla \times [\nabla \times \vec{B}] = \nabla(\nabla \cdot \mathbf{B}) - \triangle \mathbf{B}$, which reduces to $-\triangle \mathbf{B}$. The first term vanishes, as there are no magnetic monopoles, meaning $\nabla \cdot \mathbf{B} = 0$. Thus follows

$$\triangle \mathbf{B} = \mu_0 \sigma \dot{\mathbf{B}}. \tag{3.8}$$

Equation (3.8) is known as the induction equation. It is linear in $\mathbf{B}$ and has to be solved if we aim to describe the magnetic field in a conducting body.

3.1.2 Magnetic Field in a Non-Conducting Medium, $\sigma = 0$

Throughout this thesis, it is assumed that outside Europa's subsurface ocean (and water reservoirs in Chapter 4), the electrical conductivity is $\sigma = 0$. In these regions, Ampere's Law reads $\nabla \times \mathbf{B} = 0$, from which follows the existence of a gradient potential for $\mathbf{B} = -\nabla\Phi$. From the non-existence of magnetic monopoles, $\nabla \cdot \mathbf{B} = 0$, follows

$$\nabla \cdot (\nabla\Phi) = \triangle\Phi = 0, \tag{3.9}$$

which is known as the Laplace equation. In spherical coordinates (r, θ, ϕ) with radius r, colatitude θ, and longitude ϕ, the general solution of the Laplace equation reads

$$\Phi(r,\theta,\phi) = a \sum_{l=1}^{\infty} \sum_{m=0}^{l} \left(B_{\mathrm{e},l} \left(\frac{r}{a}\right)^{l} + B_{\mathrm{i},l} \left(\frac{a}{r}\right)^{l+1} \right) Y_l^m(\theta,\phi), \tag{3.10}$$

with complex external (e) and internal (i) coefficients $B_{\mathrm{e},l}$ and $B_{\mathrm{i},l}$, reference radius a, and spherical harmonics

$$Y_l^m(\theta,\phi) = P_l^m(\cos\theta) e^{im\phi}, \tag{3.11}$$

where $P_l^m(\cos\theta)$ are the associated Legendre polynomials of degree l and order m. Note that the magnetic field coefficients are specific to the degree l. A derivation of the solution can be found in Appendix A. The components of the magnetic field are given as the negative gradient of the magnetic field potential, Equation (3.10), and read

$$\begin{aligned}
B_r(r,\theta,\phi) &= -\sum_{l=1}^{\infty} \sum_{m=0}^{l} \left(l B_{\mathrm{e},l} \left(\frac{r}{a}\right)^{l-1} - (l+1) B_{\mathrm{i},l} \left(\frac{a}{r}\right)^{l+2} \right) Y_l^m(\theta,\phi) \\
B_\theta(r,\theta,\phi) &= -\sum_{l=1}^{\infty} \sum_{m=0}^{l} \left(B_{\mathrm{e},l} \left(\frac{r}{a}\right)^{l-1} + B_{\mathrm{i},l} \left(\frac{a}{r}\right)^{l+2} \right) \partial_\theta Y_l^m(\theta,\phi) \\
B_\phi(r,\theta,\phi) &= -\frac{1}{\sin\theta} \sum_{l=1}^{\infty} \sum_{m=0}^{l} \left(B_{\mathrm{e},l} \left(\frac{r}{a}\right)^{l-1} + B_{\mathrm{i},l} \left(\frac{a}{r}\right)^{l+2} \right) \partial_\phi Y_l^m(\theta,\phi).
\end{aligned} \tag{3.12}$$

3.1.3 Magnetic Field in a Conducting Medium, $\sigma \neq 0$

In a conducting medium with constant conductivity $\sigma \neq 0$, Equation (3.8) must be solved for the magnetic field. First, we transform into frequency domain, as any function of time can be represented by a superposition of sine waves with various frequencies (see Parkinson, 1983). Since the induction equation is linear, it suffices to solve for a single frequency ω, as a superposition of solutions is also a solution. We describe the magnetic field as the real part of

$$\mathbf{B}(\mathbf{r},t) = \mathbf{B}(\mathbf{r}) e^{-i\omega t}, \tag{3.13}$$

with which the induction equation takes the form

$$\triangle \mathbf{B} = -k^2 \mathbf{B}, \tag{3.14}$$

where $k^2 = i\omega\sigma\mu_0$ is the complex wave number. This equation is known as the Helmholtz equation and, in spherical coordinates, is solved for the spherical Bessel functions $j_l(z) = \sqrt{\pi/2z} J_{l+1/2}(z)$ (Abramowitz & Stegun, 1972), as well as $j_{-l}(z) = \sqrt{\pi/2z} J_{-l-1/2}(z)$ of degree l and complex argument $z = rk$. The components of the magnetic field read

$$\begin{aligned}
B_r(r,\theta,\phi) &= \frac{1}{r} \left(C j_l(rk) + D j_{-l}(rk) \right) l(l+1) Y_l^m(\theta,\phi) \\
B_\theta(r,\theta,\phi) &= \frac{1}{r} \left(C \frac{\mathrm{d}}{\mathrm{d}r} \left(r j_l(rk) \right) + D \frac{\mathrm{d}}{\mathrm{d}r} \left(r j_{-l}(rk) \right) \right) \partial_\theta Y_l^m(\theta,\phi) \\
B_\phi(r,\theta,\phi) &= \frac{1}{r\sin\theta} \left(C \frac{\mathrm{d}}{\mathrm{d}r} \left(r j_l(rk) \right) + D \frac{\mathrm{d}}{\mathrm{d}r} \left(r j_{-l}(rk) \right) \right) \partial_\phi Y_l^m(\theta,\phi).
\end{aligned} \tag{3.15}$$

A full derivation can be found in Appendix B. Equations (3.12) and (3.15) equip us with the necessary framework to describe the magnetic fields across the entire system, i.e., inside Europa's subsurface ocean, where the conductivity is finite, and anywhere else, where we assume a conductivity of zero.

3.1.4 Boundary Conditions

To ensure that our solutions for the magnetic field are physically consistent across the entire system, certain boundary conditions must be met at any boundary between two layers of varying conductivity:

i. The normal component of the magnetic field must be continuous at the boundary.

ii. The magnetic field must be finite at the center of the conductive body.

iii. At great distances, the magnetic field must be approximately equal to the external field.

In this work, we consider two models for the conductive body, (i) a homogeneous sphere to represent water reservoirs within Europa's icy crust and (ii) a spherical layer to represent Europa's subsurface ocean (Figure 3.1). As the number of boundaries varies between the two models, the solutions are unique to each case and must be calculated separately.

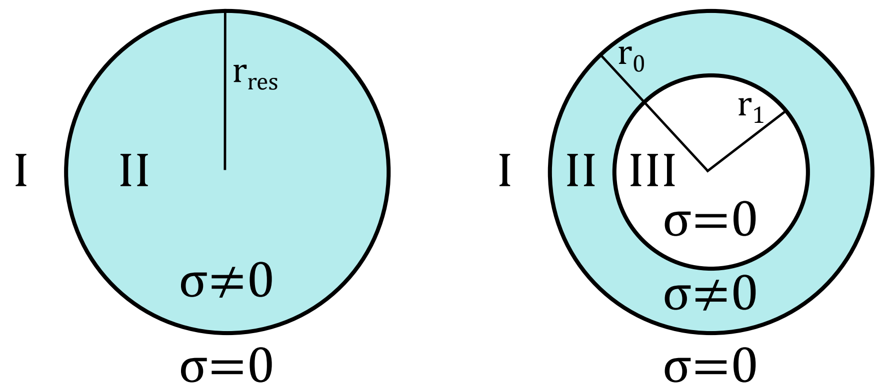

Figure 3.1: A sketch of the two models for conducting bodies (blue) considered in this work, as well as the partition into the respective subdomains. (Left) A homogeneous sphere with radius r_{res} surrounded by an insulating medium. (Right) A spherical layer with inner radius r_1 and outer radius r_0, surrounded by two subdomains with conductivity $\sigma = 0$.

Homogeneous Sphere

We describe the magnetic field inside a homogeneous sphere, e.g., a reservoir with radius r_{res} and constant conductivity σ_{res}, using Equation (3.15). As this problem is radially symmetric, an inducing field of degree l and order m only induces a magnetic field of the same degree and order. Thus, to improve readability, we omit the sums and consider only a single degree and order in the following. Here, we must note that as we reach the reservoir's center

$$\lim_{rk_{\mathrm{res}}\to 0} j_{-l}(rk_{\mathrm{res}}) \to \infty, \; l > 0, \tag{3.16}$$

which breaks the second boundary condition, thus D must be zero. From the first boundary condition follows

$$\begin{aligned} B_r^{(\mathrm{I})}\Big|_{r=r_{\mathrm{res}}} &= B_r^{(\mathrm{II})}\Big|_{r=r_{\mathrm{res}}} \\ B_\theta^{(\mathrm{I})}\Big|_{r=r_{\mathrm{res}}} &= B_\theta^{(\mathrm{II})}\Big|_{r=r_{\mathrm{res}}}, \end{aligned} \tag{3.17}$$

where (I) describes the region outside and (II) inside the reservoir. The second equation is a result of $\mu \approx \mu_0$, in which case the tangential component must be continuous as well. Applying our descriptions of the magnetic fields, the boundary conditions yield

$$\begin{aligned} -(lB_{\mathrm{e},l} - (l+1)B_{\mathrm{i},l}) &= \frac{C}{r_{\mathrm{res}}} l(l+1) j_l(r_{\mathrm{res}}k_{\mathrm{res}}) \\ -(B_{\mathrm{e},l} + B_{\mathrm{i},l}) &= \frac{C}{r_{\mathrm{res}}} \frac{\mathrm{d}}{\mathrm{d}r}(r j_l(rk_{\mathrm{res}}))\Big|_{r=r_{\mathrm{res}}}. \end{aligned} \tag{3.18}$$

From that system of equations we can derive the ratio of the magnetic field coefficients, which governs the strength of the induction response

$$\left(\frac{B_{\mathrm{i}}}{B_{\mathrm{e}}}\right)_l = -\frac{l}{l+1} \frac{J_{l+3/2}(r_{\mathrm{res}}k_{\mathrm{res}})}{J_{l-1/2}(r_{\mathrm{res}}k_{\mathrm{res}})}. \tag{3.19}$$

Spherical Layer

Consider a spherical layer of finite conductivity surrounded by two insulating layers. Such a three-layer model is commonly used to describe Europa's interior (e.g., Zimmer et al., 2000; Saur et al., 2009), i.e., an icy crust (I), subsurface ocean (II), and mantle/core material (III). We use Equation (3.12) to describe the magnetic field in (I) and (III), noting that in (III), $B_{\mathrm{i},l}^{(\mathrm{III})} = 0$, as the term would approach infinity for $r \to 0$. Since this model has two boundaries, applying Equation (3.17) yields two additional equations to account for the boundary between (II) and (III)

$$\begin{aligned} -lB_{\mathrm{e},l}^{(\mathrm{III})} &= \frac{l(l+1)}{r_1}\left(Cj_l(r_1k) + Dj_{-l}(r_1k)\right) \\ -B_{\mathrm{e},l}^{(\mathrm{III})} &= \frac{1}{r_1}\left(C\frac{\mathrm{d}}{\mathrm{d}r}\left(rj_l(rk)\right)\Big|_{r=r_1} + D\frac{\mathrm{d}}{\mathrm{d}r}\left(rj_{-l}(rk)\right)\Big|_{r=r_1}\right) \\ -(lB_{\mathrm{e},l}^{(\mathrm{I})} - (l+1)B_{\mathrm{i},l}^{(\mathrm{I})}) &= \frac{l(l+1)}{r_0}\left(Cj_l(r_0k) + Dj_{-l}(r_0k)\right) \\ -(B_{\mathrm{e},l}^{(\mathrm{I})} + B_{\mathrm{i},l}^{(\mathrm{I})}) &= \frac{1}{r_0}\left(C\frac{\mathrm{d}}{\mathrm{d}r}\left(rj_l(rk)\right)\Big|_{r=r_0} + D\frac{\mathrm{d}}{\mathrm{d}r}\left(rj_{-l}(rk)\right)\Big|_{r=r_0}\right). \end{aligned} \tag{3.20}$$

As before, we derive the ratio from the complex magnetic field coefficients as (omitting the (I) superscript)

$$\left(\frac{B_\mathrm{i}}{B_\mathrm{e}}\right)_l = -\frac{l}{l+1}\frac{\xi J_{l+3/2}(r_0 k) - J_{-l-3/2}(r_0 k)}{\xi J_{l-1/2}(r_0 k) - J_{-l+1/2}(r_0 k)}, \tag{3.21}$$

with

$$\xi = \frac{r_1 k J_{-l-3/2}(r_1 k)}{(2l+1) J_{l+1/2}(r_1 k) - r_1 k J_{l-1/2}(r_1 k)}. \tag{3.22}$$

Thorough derivations of Equations (3.19) and (3.21) are presented in Appendix C.

3.1.5 Q-Response and Gauss Coefficients

The ratio between induced and inducing field coefficients $(B_\mathrm{i}/B_\mathrm{e})_l$ can be used to calculate the induction response to an inducing field. The ratio is also known as the Q-response and is given as

$$Q_l = \left(\frac{B_\mathrm{i}}{B_\mathrm{e}}\right)_l = A_l e^{i\phi_l^\mathrm{ph}}. \tag{3.23}$$

From this equation, the induction amplitude and phase shift can be directly calculated as the absolute and argument of the Q-response

$$\begin{aligned} A_l &= \mathrm{abs}\left(\frac{B_\mathrm{i}}{B_\mathrm{e}}\right)_l \\ \phi_l^\mathrm{ph} &= \arg\left(\frac{B_\mathrm{i}}{B_\mathrm{e}}\right)_l. \end{aligned} \tag{3.24}$$

Note that our definition of the wave number k^2 differs from the commonly used $k^2 = -i\omega\sigma\mu_0$ (see, e.g., Zimmer et al., 2000; Arridge and Eggington, 2021). This definition is adapted from the often cited Parkinson (1983), and should arrive at the *modified* spherical Bessel equation. The inconsistent use of the standard spherical Bessel functions results in the complex conjugate expression for $B_{\mathrm{i},l}/B_{\mathrm{e},l}$ and thus a positive phase shift, which the authors negate by a sign change in subsequent calculations. The definition in this work results in a negative phase in the range of $-\pi/2 \leq \phi_l^\mathrm{ph} \leq 0$. The induction amplitude A_l can assume values between 0 and $l/(l+1)$. In the literature, it is common practice to represent the induction amplitude as $A = A_l l/(l+1)$, in which case it ranges from 0 to 1. A perfectly conducting body has an induction amplitude of $A = 1$ and phase shift $\phi_l^\mathrm{ph} = 0$. For a poorly conductive, small sphere, i.e., for small values of the complex argument rk, the induction amplitude can be Taylor approximated as

$$A \approx \frac{r^2\omega\sigma\mu_0}{15}. \tag{3.25}$$

While the complex field coefficients have been used to derive descriptions for the induction amplitude and phase shift, the magnetic field itself is usually represented in external Gauss coefficients (q_l^m, s_l^m) and internal Gauss coefficients (g_l^m, h_l^m). In this work, we use external Gauss coefficients to describe the inducing field and internal Gauss coefficients for the induced field. We can split up the full solution of the Laplace equation into an inducing field potential

$$\Psi(r,\theta,\phi,t) = a\sum_{l=1}^{\infty}\sum_{m=0}^{l}\left(\frac{r}{a}\right)^{l} P_l^m(\cos\theta)\left(q_l^m\cos m\phi + s_l^m\sin m\phi\right)e^{-i\omega t} \tag{3.26}$$

and an induced field potential

$$\Phi(r,\theta,\phi,t) = a\sum_{l=1}^{\infty}\sum_{m=0}^{l}\left(\frac{a}{r}\right)^{l+1} P_l^m(\cos\theta)\left(g_l^m\cos m\phi + h_l^m\sin m\phi\right)e^{-i\omega t}. \tag{3.27}$$

Here, the real description of the spherical harmonics is used. At the surface of the conducting body, $r = a$, the induced field potential can be calculated using the Q-response, Equation (3.23), where we consider each degree l separately

$$\begin{aligned}\Phi_l(r,\theta,\phi,t) &= Q_l\Psi_l(r,\theta,\phi,t)\\ &= aA_l e^{i\phi_l^{\mathrm{ph}}}\sum_{m=0}^{l} P_l^m(\cos\theta)\left(q_l^m\cos m\phi + s_l^m\sin m\phi\right)e^{-i\omega t}\\ &= a\sum_{m=0}^{l} P_l^m(\cos\theta)\left(A_l q_l^m\cos m\phi + A_l s_l^m\sin m\phi\right)e^{-i(\omega t-\phi_l^{\mathrm{ph}})}.\end{aligned} \tag{3.28}$$

From this expression follows, that internal and external Gauss coefficients are related via

$$\begin{Bmatrix} g_l^m \\ h_l^m \end{Bmatrix} = A_l \begin{Bmatrix} q_l^m \\ s_l^m \end{Bmatrix}. \tag{3.29}$$

Furthermore, the induced field lags behind the inducing field by a factor $\phi_l^{\mathrm{ph}}/\omega$. It is also worth noting that, as the phase shift is a function of the degree l, each multipole moment of the induced field has its individual temporal lag.

3.2 Coupled Induction Response

In the previous section, we have learned about the relationship between external and internal Gauss coefficients, as well as the temporal delay of the induction response due to a phase shift $\phi_l^{\mathrm{ph}} \neq 0$. We calculated the Q-response for a homogeneous sphere and a spherical layer of constant conductivity. In both cases, spherical symmetry is required, or else the derived equations would not apply. In this section, we will consider two neighboring conducting bodies. As their induced fields, excited by a temporally variable primary magnetic field, are also time-varying, they will act as inducing fields on the other conducting body, respectively. This process enables a coupling mechanism between the two bodies, which must be taken into account to describe the magnetic field in their vicinity.

The relevance of such a scenario becomes apparent when considering potential water melt in Europa's icy crust. As introduced in Section 2.2.2, such melt features could be involved in the formation of chaos regions. Disconnected from Europa's ocean, such reservoirs of liquid water would generate their own induction response to the Jovian magnetic field. The global subsurface ocean would induce additional fields inside the local water reservoir and vice versa. While the approach developed in this section applies to any case of two neighboring bodies, we will put an emphasis on the case of a local water reservoir and a global subsurface ocean (Figure 3.2). The approach to solve the coupled induction has also been published in Winkenstern and Saur (2023).

In the following, we will present the first iterations of the induced fields. Here, we introduce the iteration step n and represent Gauss coefficients in the following way, $\left((g_l^m)^{(n)}, (h_l^m)^{(n)}\right)$, for the internal Gauss coefficients of degree l, order m, and iteration step n. In this notation, $n = 1$ corresponds to the induced field excited by the time-varying component of the Jovian magnetospheric field, $n = 2$ are the induced fields generated by the former induced fields, and so on.

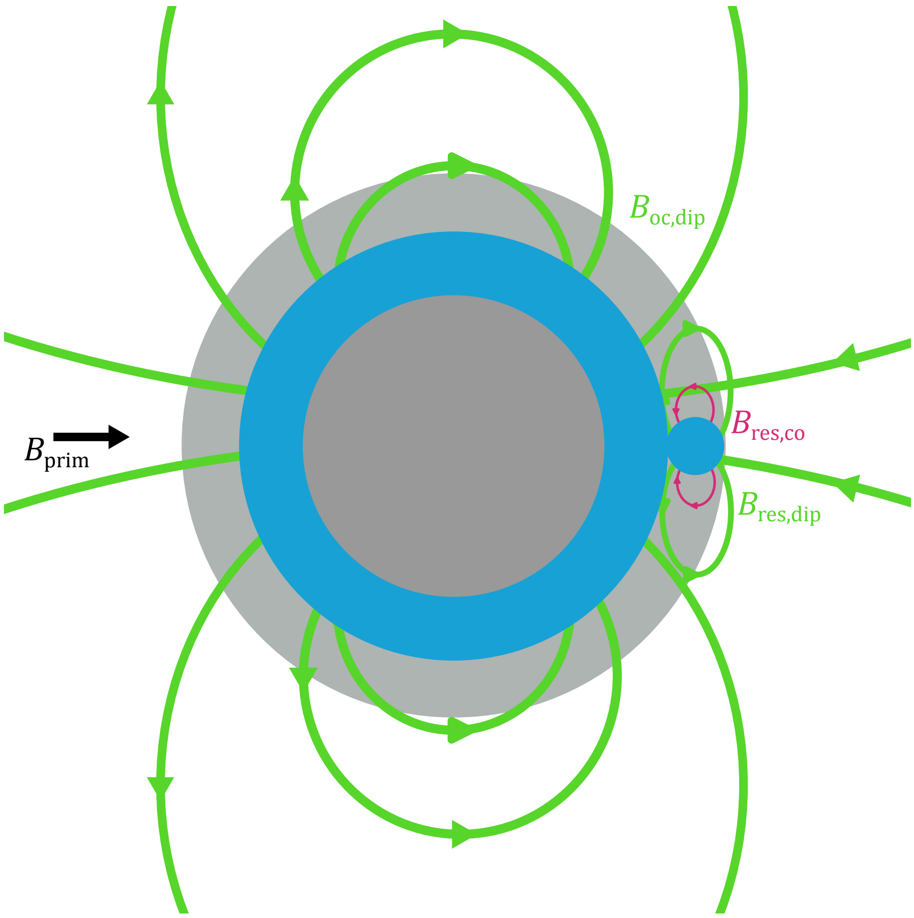

Figure 3.2: Sketch of Europa's interior considered in this section, as shown in Winkenstern and Saur (2023). Embedded in a primary field $\mathbf{B}_{\mathrm{prim}}$, a dipole is induced in both the ocean and reservoir, respectively, represented by green field lines. The induced dipoles act as inducing fields, resulting in coupled induction responses (purple).

3.2.1 Calculating the Induced Dipole, $n = 1$

As we assume the Jovian magnetospheric field is homogeneous in Europa's vicinity, the induction response is a pure dipole (Saur et al., 2009), i.e., only Gauss coefficients of degree $l = 1$ are induced. Due to the homogeneity, the external Gauss coefficients of the Jovian field $\mathbf{B}_\mathrm{J}(t) = (B_{\mathrm{J},x}(t), B_{\mathrm{J},y}(t), B_{\mathrm{J},z}(t))$ are $q_\mathrm{J} = q_1^1(t) = -B_{\mathrm{J},x}(t)$ and $s_\mathrm{J} = s_1^1(t) = -B_{\mathrm{J},y}(t)$, respectively. We assume that $q_1^0 = 0$, as temporal variabilities in the B_z-component are negligible (Kivelson et al., 1999), confining Jupiter's inducing field to the xy-plane. Embedding the temporal variability of the magnetic field into the Gauss coefficients, for example $q_l^m(t) = q_l^m e^{-i\omega t}$, we obtain the induced field at a time t from the external coefficients at an earlier time $t + \phi_1^{\mathrm{ph}}/\omega$ as

$$\begin{Bmatrix} (g_1^1)^{(1)}(t) \\ (h_1^1)^{(1)}(t) \end{Bmatrix} = A_1 \begin{Bmatrix} q_\mathrm{J}(t + \phi_1^{\mathrm{ph}}/\omega) \\ s_\mathrm{J}(t + \phi_1^{\mathrm{ph}}/\omega) \end{Bmatrix}, \tag{3.30}$$

for the ocean and reservoir, respectively. From that, the induced field potentials can be calculated, where we employ two coordinate systems, one with center in Europa, (r, θ, ϕ), to describe the ocean's induced fields, and a second with center in the reservoir, (r', θ', ϕ'), to describe its induced fields

$$\begin{aligned} \Phi_{\mathrm{oc}}^{(1)}(r,\theta,\phi,t) &= r_0 \left(\frac{r_0}{r}\right)^2 \sin\theta \left(\left(g_1^1\right)_{\mathrm{oc}}^{(1)}(t)\cos\phi + \left(h_1^1\right)_{\mathrm{oc}}^{(1)}(t)\sin\phi \right) \\ \Phi_{\mathrm{res}}^{(1)}(r',\theta',\phi',t) &= r_{\mathrm{res}} \left(\frac{r_{\mathrm{res}}}{r'}\right)^2 \sin\theta' \left(\left(g_1^1\right)_{\mathrm{res}}^{(1)}(t)\cos\phi' + \left(h_1^1\right)_{\mathrm{res}}^{(1)}(t)\sin\phi' \right), \end{aligned} \tag{3.31}$$

where r_0 is the ocean's outer radius r_{res} the reservoir's radius.

3.2.2 Solving the Coupling Feedback

In the next iteration step, $n = 2$, we have to account for higher degrees in the potential description, as the inducing fields cannot be assumed to be homogeneous anymore. If we were to continue the calculation from the prior iteration step, with internal Gauss coefficients at the time t, we would obtain the internal Gauss coefficients of the second iteration at a later time $t - \phi_l^{\mathrm{ph}}/\omega$. We are, however, interested in the total induction response at one time t. Thus, we must first calculate the external coefficients of the Jovian field at a time $t + (\phi_{1,\mathrm{oc}}^{\mathrm{ph}} + \phi_{l,\mathrm{res}}^{\mathrm{ph}})/\omega$ to obtain the ocean's internal Gauss coefficients of first iteration as

$$\begin{Bmatrix} (g_1^1)_{\mathrm{oc}}^{(1)}(t + \phi_{l,\mathrm{res}}^{\mathrm{ph}}/\omega) \\ (h_1^1)_{\mathrm{oc}}^{(1)}(t + \phi_{l,\mathrm{res}}^{\mathrm{ph}}/\omega) \end{Bmatrix} = A_{1,\mathrm{oc}} \begin{Bmatrix} q_\mathrm{J}(t + (\phi_{1,\mathrm{oc}}^{\mathrm{ph}} + \phi_{l,\mathrm{res}}^{\mathrm{ph}})/\omega) \\ s_\mathrm{J}(t + (\phi_{1,\mathrm{oc}}^{\mathrm{ph}} + \phi_{l,\mathrm{res}}^{\mathrm{ph}})/\omega) \end{Bmatrix}, \tag{3.32}$$

from which the induced field potential $\Phi_{\mathrm{oc}}^{(1)}(r, \theta, \phi, t + \phi_{l,\mathrm{res}}^{\mathrm{ph}})$ can be obtained, analogous to Equation (3.31). To calculate the external Gauss coefficients and describe the ocean's induced dipole as an inducing field, the radial component of the magnetic field across the reservoir's surface is required. The ocean's induced field $\mathbf{B}_{\mathrm{oc}}^{(1)}$, however, is given in Europa-centered coordinates. In this reference frame, the reservoir is not spherically symmetric. Thus, it is required to first transform the ocean's induction response into reservoir-centered coordinates $\mathbf{B}_{\mathrm{oc}}^{(1)}(r', \theta', \phi')$. A detailed description of the coordinate transformation is given in Appendix D. After performing the transformation, we can use the radial component of the ocean's induction response across the reservoir's surface $B_{\mathrm{oc},r'}^{(1)}(r' = r_{\mathrm{res}}, \theta', \phi')$ to calculate the corresponding external Gauss coefficients via

$$\begin{aligned}\begin{Bmatrix} (q_l^m)_{\mathrm{oc}}^{(1)}\left(t + \phi_{l,\mathrm{res}}^{\mathrm{ph}}/\omega\right) \\ (s_l^m)_{\mathrm{oc}}^{(1)}\left(t + \phi_{l,\mathrm{res}}^{\mathrm{ph}}/\omega\right) \end{Bmatrix} = &- \frac{2l+1}{4\pi l} \\ &\int_0^{\pi}\int_0^{2\pi} \mathrm{d}\phi'\mathrm{d}\theta' \sin\theta' P_l^m(\cos\theta') B_{\mathrm{oc},r'}^{(1)}(\theta', \phi') \begin{Bmatrix} \cos m\phi' \\ \sin m\phi' \end{Bmatrix}.\end{aligned} \tag{3.33}$$

As before, we can use the relationship between internal and external Gauss coefficients to obtain the reservoir's induction response of iteration $n = 2$

$$\begin{Bmatrix} (g_l^m)_{\mathrm{res}}^{(2)}(t) \\ (h_l^m)_{\mathrm{res}}^{(2)}(t) \end{Bmatrix} = A_{l,\mathrm{res}} \begin{Bmatrix} (q_l^m)_{\mathrm{oc}}^{(1)}\left(t + \phi_{l,\mathrm{res}}^{\mathrm{ph}}/\omega\right) \\ (s_l^m)_{\mathrm{oc}}^{(1)}\left(t + \phi_{l,\mathrm{res}}^{\mathrm{ph}}/\omega\right) \end{Bmatrix}, \tag{3.34}$$

as well as the resulting induced field potential

$$\begin{aligned}\Phi_{\mathrm{res}}^{(2)}(r', \theta', \phi', t) = r_{\mathrm{res}} &\sum_{l=1}^{l_{\max}} \sum_{m=0}^{l} \left(\frac{r_{\mathrm{res}}}{r'}\right)^{l+1} P_l^m(\cos\theta') \\ &\left((g_l^m)_{\mathrm{res}}^{(2)}(t)\cos m\phi' + (h_l^m)_{\mathrm{res}}^{(2)}(t)\sin m\phi'\right).\end{aligned} \tag{3.35}$$

Analogously, the ocean's induced potential $\Phi_{\mathrm{oc}}^{(2)}(r, \theta, \phi, t)$ due to the reservoir's induced dipole $\mathbf{B}_{\mathrm{res}}^{(1)}$ can be calculated by following the above steps. Note that the sum over degree l does not go to infinity, but rather up to a prescribed degree $l_{\max}$ due to numerical limitations. The choice of the maximum degree is a compromise between accurately describing the physical processes and runtime, and will be discussed in Section 3.2.3.

Calculating the induction response of iteration step $n = 3$ adds an additional layer of complexity. Before, only the internal coefficients $(g_1^1)^{(1)}$ and $(h_1^1)^{(1)}$ had to be considered to obtain the inducing field and its external Gauss coefficients $(q_l^m)^{(1)}$ and $(s_l^m)^{(1)}$, respectively. Since the induction response of second iteration is not a pure dipole, each multipole moment generates its own full set of external Gauss coefficients after coordinate transformation. We label those external Gauss coefficients $(q_{l'}^m)^{(2)}$ and $(s_{l'}^m)^{(2)}$, with $l' \in [1, 2, ..., l_{\max}]$. We follow the same steps as in iteration step $n = 2$, calculating external Gauss coefficients for each degree of $(g_l^m)^{(2)}$ and $(h_l^m)^{(2)}$, which results in $l_{\max}$ subsets of external Gauss coefficients $(q_{l'}^m)^{(2)}$ and $(s_{l'}^m)^{(2)}$, each corresponding to a specific multipole moment. The overall external Gauss coefficients are obtained by taking the sum over all subsets

$$\begin{aligned}(q_l^m)^{(2)} &= \sum_{l'=1}^{l_{\max}} (q_{l'}^m)^{(2)} \\ (s_l^m)^{(2)} &= \sum_{l'=1}^{l_{\max}} (s_{l'}^m)^{(2)}.\end{aligned} \tag{3.36}$$

With each additional iteration, the induced field is further delayed by a factor determined by the phase lag of each individual degree $\phi_l^{\mathrm{ph}}/\omega$. Assuming an induction amplitude $A < 1$, with each iteration the induced field is bound to be weaker than its inducing field. This effect is additionally increased by the distance term r^{-l-1} in the magnetic field potential. The continuous decrease of the inducing field strength eventually results in a convergence to the full solution, where additional iteration steps add negligible contributions to the overall description of the induction response.

3.2.3 Numerical Precision

In its most precise form, the magnetic field potential is a sum over $l \in [1, 2, ..., \infty)$. In the numerical implementation, the transformed radial component of the magnetic field is thus only approximated by a finite set of Gauss coefficients. To assess the maximum degree l_{max}, we calculate the root-mean-square (RMS) between the transformed radial component $B_{r,\mathrm{transformed}}$ and its Gauss description $B_{r,\mathrm{gauss}}$ across the reservoir's surface

$$RMS = \sqrt{\frac{\sum_{i,j} \left(B_{r,\mathrm{transformed}}(\theta_i, \phi_j) - B_{r,\mathrm{gauss}}(\theta_i, \phi_j)\right)^2}{N_{ij}}}, \tag{3.37}$$

where N_{ij} is the number of grid points. As the magnetic field strength lies in the order of 400 nT, with perturbations in the range of 10 to 100 nT, we prescribe a precision of 10^{-2} nT, below which the RMS must lie to obtain a sufficiently accurate solution. Signatures and deviations below this limit will likely not be resolved with magnetometer measurements and provide no detectable information. Figure 3.3 shows the RMS as a function of maximum degree l_{max} used for the Gauss description of the radial component and was used to assess the necessary maximum degree for an RMS below 10^{-2} nT. For this assessment, the largest reservoir considered in this study ($r_{\mathrm{res}} = 20$ km) was used, as the inhomogeneity of the inducing field increases with the size of the reservoir. From the figure, we derive $l_{\mathrm{max}} = 3$. Figure 3.4 compares the transformed radial component of the ocean's induction response $B_{\mathrm{oc},r'}^{(1)}$ against its Gauss description up to degree 3. We see, that the inducing field is well represented across the reservoir's surface by its Gauss representation with $l_{\mathrm{max}} = 3$.

3.2.4 Mauersberger-Lowes Spectrum

As previously mentioned, the coupling feedback converges after a certain amount of iteration steps, as each coupled induction response is weaker than the previous one. To control the required number of iterations to describe the induction coupling with a prescribed precision, we introduce the Mauersberger-Lowes spectrum, which shows the magnetic power per degree and iteration $(R_l)^{(n)}$ as (Langel & Estes, 1982)

$$(R_l)^{(n)} = (l+1) \sum_{m=0}^{l} \left[\left((g_l^m)^{(n)}\right)^2 + \left((h_l^m)^{(n)}\right)^2 \right]. \tag{3.38}$$

Considering the previously prescribed precision of 10^{-2} nT for the overall induction, for a dipole this value correlates to a magnetic power on the order of $10^{-4}\,\mathrm{nT}^2$. Thus, iterations where the magnetic power lies below $10^{-4}\,\mathrm{nT}^2$ for all degrees are excluded.

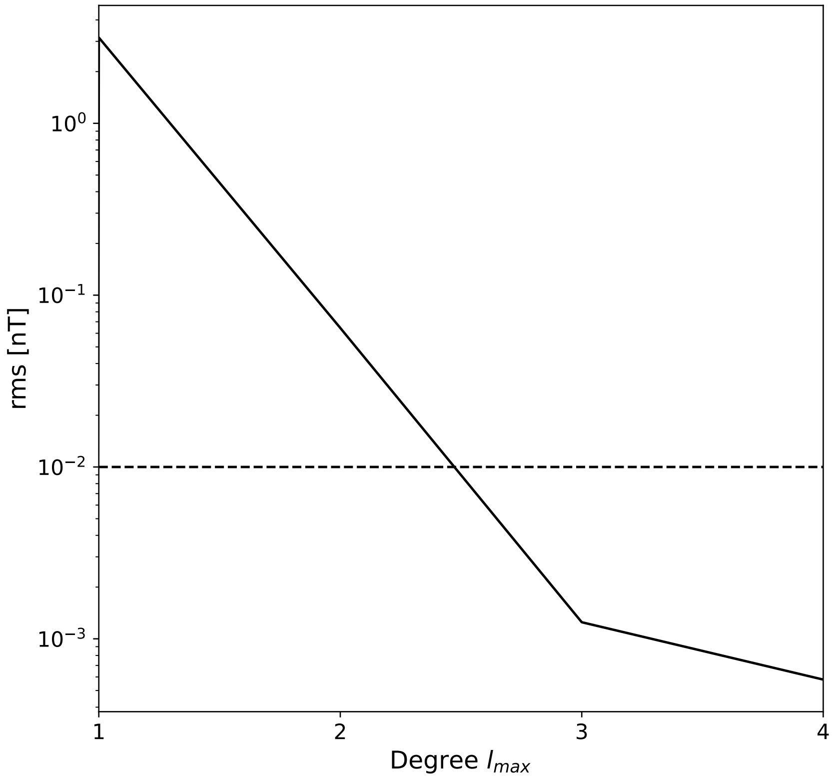

Figure 3.3: RMS according to Equation (3.37) as a function of maximum degree $l_{\max}$ used in the Gauss description of the magnetic field potential. The dashed line indicates the required precision of 10^{-2} nT. The calculation of the RMS was performed across the reservoir's surface with radius $r_{\text{res}} = 20$ km and conductivity $\sigma_{\text{res}} = 30$ S/m.

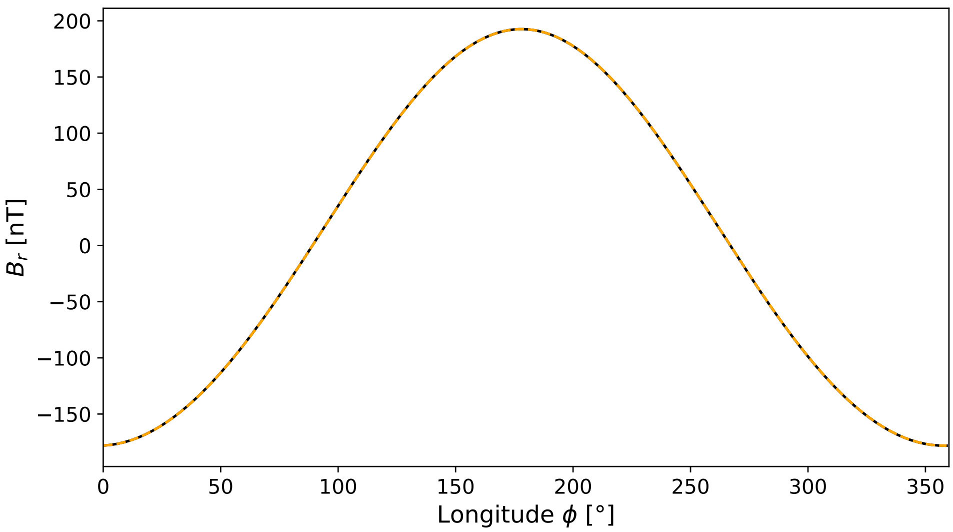

Figure 3.4: Transformed radial component of the ocean's induction response across the reservoir's surface at $\theta = 90°$ (black, solid) and its Gauss representation with $l_{\max} = 3$ (orange, dashed) as a function of longitude ϕ.

4

Detectability of Liquid Water Reservoirs

This chapter presents the study published in Winkenstern and Saur (2023), which investigates the potential detectability of local water melt entrapped in Europa's icy crust. Such water melt could be involved in the formation of chaos regions, though the exact formation mechanism of these disrupted ice regions is not exactly known. The underlying assumption is that the reservoir is disconnected from the global subsurface ocean, creating its own induction response. As both induced fields generated within the ocean and reservoir are time-varying fields, they will also act as inducing fields on the water body, respectively. This enables a coupling mechanism between ocean and reservoir, which must be taken into account to accurately describe the system. The theoretical background of the coupled induction is introduced in Section 3.2. The study is based on an idea proposed by Joachim Saur and has been developed together from there on. The original manuscript was fully written by Jason Winkenstern and revised with the co-author and referees, except Section 4.3.5, which was written by Joachim Saur. Sections 1 and 2 (Introduction and Methods) of the publication are not included in this chapter to avoid redundancy.

4.1 Model Implementation

In this section, we describe the model setup and its implementation. First, the equation for the inducing field is introduced, followed by a discussion of existing values for the ice shell thickness and the ocean's conductivity to motivate the prescribed parameter space of reservoir radii and conductivities. Finally, we explore additional inducing periodic signals in Europa's rest frame and the reservoir's induction response at those compared to the synodic rotation period.

4.1.1 Inducing Background Field

We approximate the inducing part of the Jovian background field $\mathbf{B}_\mathrm{J}(t)$ to be elliptically polarized (see Figure 1 in Khurana et al., 1998) with

$$\begin{aligned} B_{\mathrm{J},x}(t) &= B_{0,x}\cos(\omega t + \phi_x^{\mathrm{ph}}) \\ B_{\mathrm{J},y}(t) &= B_{0,y}\cos(\omega t + \phi_y^{\mathrm{ph}}) \\ B_{\mathrm{J},z}(t) &= 0, \end{aligned} \tag{4.1}$$

in Europa IAU coordinates, where $\mathbf{B}_0 = (-217, 64, 0)\,\mathrm{nT}$, $\phi_x^{\mathrm{ph}} = 0$, and $\phi_y^{\mathrm{ph}} = -\pi/2$. Note that the magnetic field in Khurana et al. (1998) is given in EPhiO coordinates, which correspond approximately to $x \to y$ and $y \to -x$ in IAU coordinates. For the purpose of this paper, we neglect the small misalignment of unit vector directions in EPhiO and Europa IAU coordinates. We will choose $\omega t_{\mathrm{obs}} = \pi$ in Section 4.2, where we show the results of our coupled model. This choice leads to the maximum background field for our induction studies.

4.1.2 Geometric Parameters

As chaos terrain is mostly found near equatorial regions (Greenberg et al., 1999), we assume a reservoir position in the xy-plane. We choose a position parallel to the x-axis, which also aligns with the magnetic background field at the chosen time. As the main focus of this work lies on the induction signature of a reservoir of different sizes and conductivities, the ocean's induction amplitude remains constant to ensure similar induction responses throughout the study. We assume a fixed sea floor depth of 150 km, corresponding to an inner radius $r_1 = 1410\,\mathrm{km}$[1]. The outer radius will be changed accordingly to the radius of the reservoir so that the reservoir spans across the entire icy crust, but still does not overlap with the global ocean. In this way, our study gives an upper limit to the expected small signals. The only exceptions to this geometry are Figures 4.2 and 4.3, where a small gap is added to highlight additional effects of the ocean-reservoir system. As changing the outer radius effects the ocean's induction amplitude, its conductivity must be adjusted accordingly (see Section 4.1.4). It should be noted that while this method keeps the induction amplitude constant, this does not hold true for the phase shift. We will consider reservoir radii ranging from $5-20\,\mathrm{km}$, accordingly to crust thicknesses found in literature.

4.1.3 Ice Shell Thickness

The thickness of Europa's icy crust is a crucial parameter in the description of its induction response, as the ratio $(r_0/r_\mathrm{m})^3$ governing the induced dipole field is larger for a shallow ocean compared to a deep one, resulting in a stronger induced magnetic field around Europa. Different methods have been used to infer the crust's thickness, yielding varying estimates. A range of those estimates is summarized in Table 4.1. It is noteworthy that, as a consequence of the non-uniqueness of the induction problem and unknown conductivity, the bounds found with the induction method are less constraining than other methods.

[1] In this manuscript, $R_\mathrm{E} = 1560\,\mathrm{km}$ was used for Europa's radius.

Table 4.1: A collection of literature values for the ice shell thickness h.

h /km	Reference	Method
≤ 15	Hand and Chyba (2007)	Induction
≤ 100	Zimmer et al. (2000)	Induction
≥ 4	Turtle and Pierazzo (2001)	Impact crater modelling
$5-10$	Silber and Johnson (2017)	Impact crater modelling
> 19	Schenk (2002)	Impact crater observation
$20-25$	Tobie et al. (2003)	Tidal dissipation model
≤ 3	Lee et al. (2005)	Cycloid crack formation
≈ 25	Prockter et al. (2000)	Crustal cycling

4.1.4 Electrical Conductivity

The electrical conductivity driven by dissolved ions can generally be expressed as a function of pressure, temperature, and concentration of the respective salt (McCleskey et al., 2012; Pan et al., 2020, 2021). A key issue about Europa's ocean is the uncertainty about its chemical composition (McKinnon & Zolensky, 2003; Ligier et al., 2016; Trumbo et al., 2019, 2022). As recent UV observations favor an ocean composition rich in sodium chloride, we focus on the conductivity range achieved with it. Hand and Chyba (2007) inferred conductivities of up to $30\,\mathrm{S/m}$. It should, however, be noted that they used a fit for sea salt, of which the main contributor is sodium chloride at approximately 90%. For our parameter study, values ranging from $0.5-30\,\mathrm{S/m}$ will be considered for the reservoir, covering a low conductivity limit as well as the conductivity at saturation. As we vary the ocean's outer radius, keeping a fixed ocean conductivity σ_{oc} throughout all simulations would result in different induction amplitudes for the ocean and thus influence the reservoir's induction differently between individual runs. Thus, we adapt the conductivity of the ocean so that the induction amplitude remains constant at $A_{\mathrm{oc}} = 0.91$. This is done by computing the induction amplitude prior to the study and adjusting the conductivity until A_{oc} reaches 0.91, corresponding to a conductivity of $\sigma_{\mathrm{oc}} \approx 0.5 \pm 0.1\,\mathrm{S/m}$ for ocean thicknesses in the range of $110-140\,\mathrm{km}$, which has been derived in Schilling et al. (2007). Other values for the ocean's conductivity are plausible, as is evident by the broad conductivity range found in literature cited within this section. This is due to the non-uniqueness of the problem, where different choices for the ocean's thickness, depth, and conductivity can result in the same induction amplitude.

4.1.5 Frequency of the Inducing Field

In addition to Jupiter's synodic rotation period, Europa is subject to further periodicities with various magnetic field amplitudes, which allow for electromagnetic sounding at multiple frequencies (Seufert et al., 2011). This is of particular interest for the detection of a shallow reservoir, as its induction amplitude increases with frequency, for example, higher order harmonics of Jupiter's synodic period at $5.62\,\mathrm{h}$ and $3.33\,\mathrm{h}$, respectively. However, the amplitudes of the inducing field at those frequencies are one to two orders of magnitudes lower compared to the amplitude at the $11.23\,\mathrm{h}$ period, resulting in an overall weaker induction response at these frequencies. This is shown in Figure 4.1, where the reservoir's induction response in spherical coordinates is given for various periodicities. In addition to the synodic periods, we also present the induction signals at 85.22 h and 641.90 h, corresponding to Europa's orbital period and the solar rotation period. The induced fields resulting from these signals are weaker. Thus, we will only consider the magnetic fields induced by the synodic period $T = 11.23$ h throughout calculations in this work.

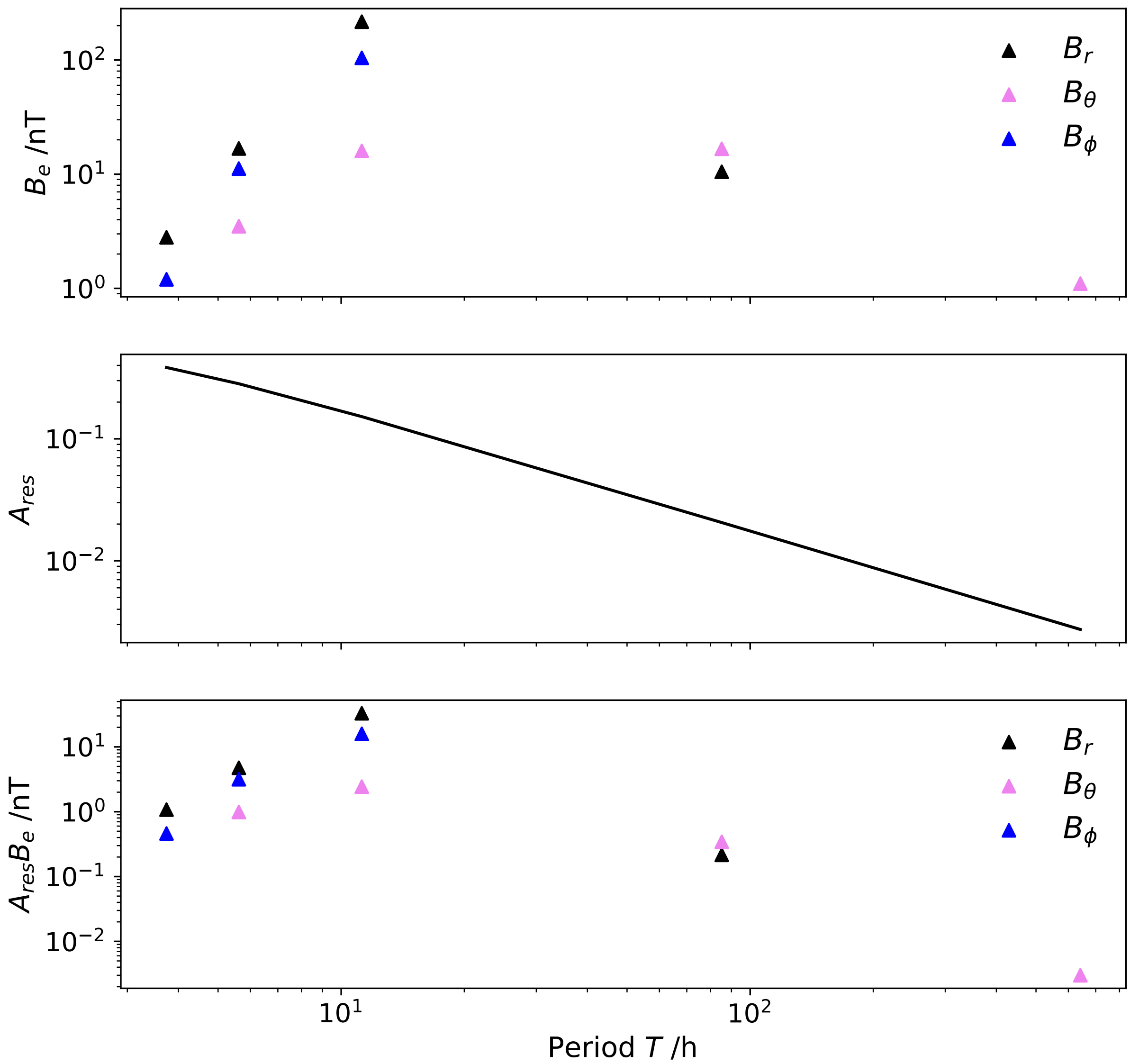

Figure 4.1: Magnetic field amplitudes of the periodic signals in System III coordinates (top). Induction response of a 20 km-diameter reservoir ($\sigma_{res} = 10$ S/m) as a function of period (middle). Resulting induction responses of the reservoir to the magnetic field amplitudes at their respective periods (bottom).

4.2 Results

To highlight the effects of the coupled induction, we present the physics in the illustrative case of a perfectly conducting ocean and reservoir, before showing the effects of coupled induction in finite cases. Afterward, we investigate the detectability of reservoirs with radii and conductivities discussed in Sections 4.1.2 and 4.1.4 at 25 km altitude and at the surface.

4.2.1 Physics of the Coupled System

Figure 4.2 visualizes the magnetic field components in the xy-plane in the vicinity of a perfectly conducting reservoir, with and without coupling effects. It is apparent that only with consideration of coupled induction, the reservoir behaves like a perfectly conducting body, i.e., the inducing field does not penetrate the body. We added a small gap between the ocean and reservoir in the example shown in Figure 4.2. This is to highlight that in addition to not permitting the magnetic field to penetrate the conducting bodies, due to $\sigma \to \infty$, the area between reservoir and ocean is also nearly completely shielded from the magnetic field at a close distance.

In a realistic scenario, the ocean's and reservoir's induction amplitudes are smaller than one. In addition to this, their phase shift is non-zero, resulting in induction responses that are no longer antiparallel to the inducing field, which is shown in Figure 4.3. Here, the total magnetic field is stronger than in the perfectly conducting case due to the weaker induction response and the xy-components are not aligned along the y-axis as a result of the phase shift.

4.2.2 Coupling Interaction Strength

To obtain a sufficiently accurate and numerically efficient description of the coupling processes, it is important to look at the contributions of each coupling iteration. Figure 4.4 shows the Mauersberger-Lowes spectrum calculated with Equation (3.38) for both the ocean and reservoir induced fields up to the first coupled field (iteration step $n = 2$). For the ocean, the main contribution is generated by the dipole response to the Jovian background field with a magnetic power of approximately $10^4\,\mathrm{nT}^2$. Due to the geometry, the reservoir induces higher degrees in the ocean, where the power reaches a maximum of approximately $10^{-6}\,\mathrm{nT}^2$ at degree $l = 7$ and decreases thereafter. Compared to the dipole term of first iteration $n = 1$ with $10^4\,\mathrm{nT}^2$, the coupling from the ocean to the reservoir, i.e., the induced field of second iteration $n = 2$, is negligible, with a radial component in the order of $10^{-2}\,\mathrm{nT}$ at the surface of the reservoir. It is thus excluded in any further calculations and results, as such weak induced fields will not be detectable.

The reservoir's induction response of first iteration $n = 1$ is the dipole response to Jupiter's background field, and thus only has a degree $l = 1$ contribution. The magnetic power of the induced dipole in the reservoir is around two orders of magnitude smaller than the ocean's induction response. This is a direct consequence of the reservoir's small extension

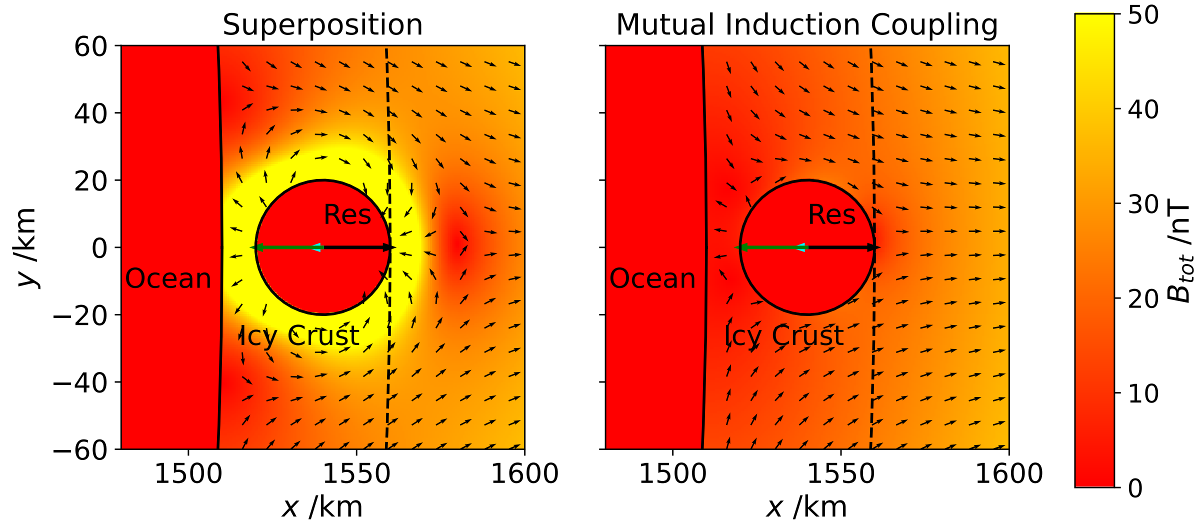

Figure 4.2: Magnetic field components in the xy-plane in the ocean-reservoir environment with radius $r_{\mathrm{res}} = 20\,\mathrm{km}$, assuming both ocean and reservoir are perfectly conducting. The left panel shows the vector field only after the first iteration, i.e., a superposition of the induced dipole fields in the ocean and reservoir, whereas the right panel visualizes the field after coupling iteration $n = 2$. The arrows representing the magnetic field are normalized in length and do not represent the strength of the magnetic field, which is instead color coded in the background. The arrows in the center indicate the orientations of the background field (black), ocean induced field (green), and reservoir induced field (cyan), where the length indicates the strength relative to the background field. The dashed black line visualizes the surface boundary.

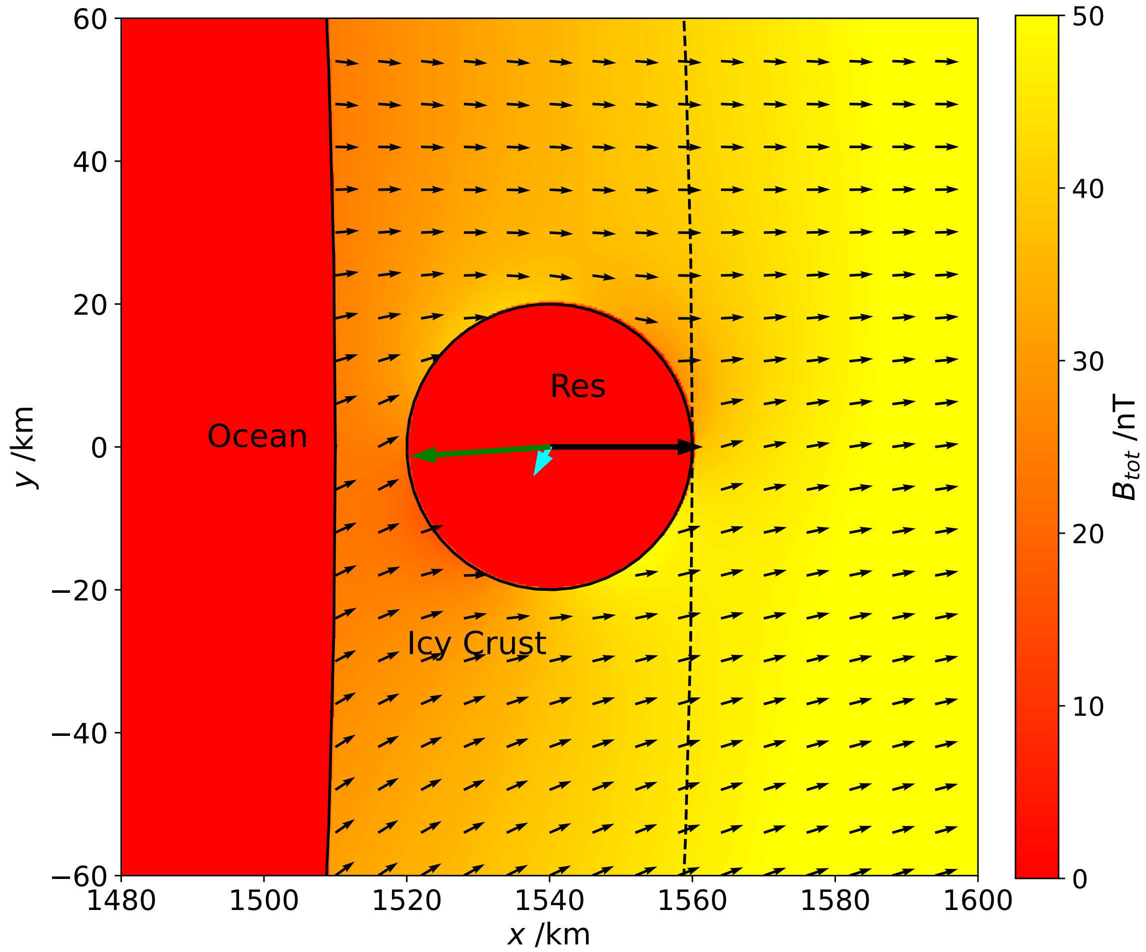

Figure 4.3: Magnetic field components in the xy-plane in the ocean-reservoir environment after mutual induction coupling for a reservoir with radius $r_{\mathrm{res}} = 20\,\mathrm{km}$ and finite conductivity $\sigma_{\mathrm{res}} = 30\,\mathrm{S/m}$, where the induction response of the system follows Equation (4.2). The arrows representing the magnetic field are normalized in length and do not represent the strength of the magnetic field, which is instead color coded in the background. The arrows in the center indicate the orientations of the background field (black), ocean induced field (green), and reservoir induced field (cyan), where the length indicates the strength relative to the background field. The dashed black line visualizes the surface boundary.

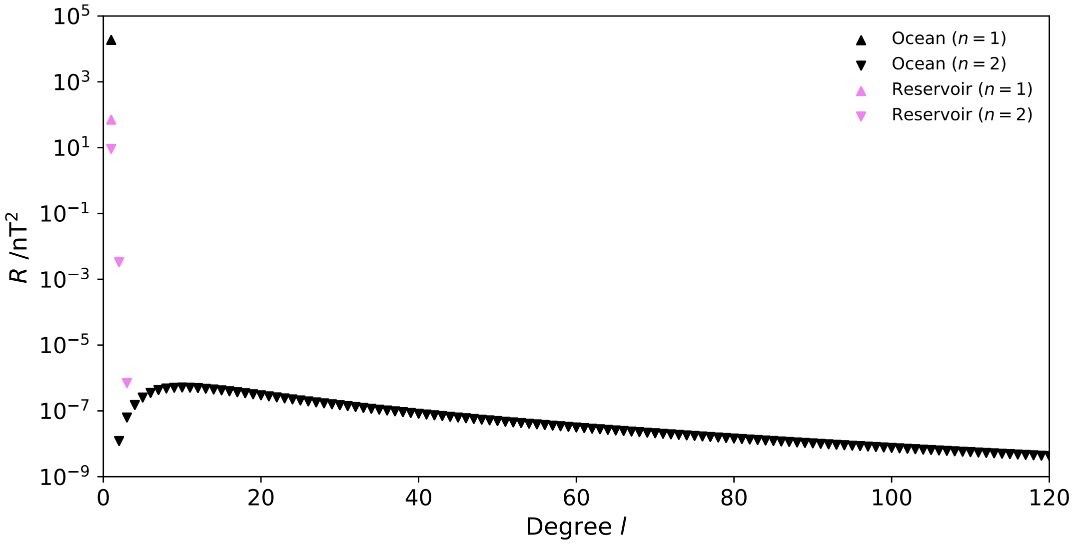

Figure 4.4: Mauersberger-Lowes spectrum for the ocean (black) and reservoir (violet) for multipole degrees up to $l_{\mathrm{max}} = 120$. Upward triangles show the dipoles induced by the Jovian background field. Downward triangles represent the induced fields of second iteration.

and thus induction amplitude, as following from Equation (3.25). However, the reservoir induced field of second iteration $n = 2$ has significant contributions at degrees $l = 1$ and $l = 2$ due to the inhomogeneous nature of the inducing field from the ocean and must be considered to describe the mutual feedback and to meet the prescribed precision of 10^{-2} nT introduced in Section 3.2.3. Thus, the reservoir is strongly coupled to the ocean, whereas the influence from the reservoir on the induction response of the ocean is overall negligible (see small R values for $l > 1$ for the ocean in Figure 4.4). The total induction response of the system can be described as a sum of three induction responses

$$\mathbf{B}_{\mathrm{ind,tot}} = \mathbf{B}_{\mathrm{oc}}^{(1)} + \mathbf{B}_{\mathrm{res}}^{(1)} + \mathbf{B}_{\mathrm{res}}^{(2)}. \tag{4.2}$$

For the geometries considered in this model, the reservoir is coupled to the ocean and reacts considerably to its induced dipole. The coupling of the ocean to the reservoir is negligibly small due to the difference in size.

4.2.3 Detectability at 25 km Altitude

With Europa Clipper, multiple encounters with an altitude of 25 km at closest approach are planned (Campagnola et al., 2019). For that purpose, we investigate the induction strength of a coupled system at 25 km in comparison to a radially symmetric system during a hypothetical flyby above the reservoir. Here, two effects that contribute to magnetic field perturbations in Europa's vicinity, additionally to induction by a subsurface ocean and reservoir, need to be considered, as they can potentially obscure the weak induction signal of a reservoir. The first is plasma interactions in Europa's ionosphere, which are largest when Europa is in the plasma sheet and can generate perturbations on the order of $100 - 200$ nT. Additional perturbations can be present in magnetometer measurements if the spacecraft crosses the Europan Alfvén wings (Schilling et al., 2007, 2008). The second phenomenon is apparently random small-scale fluctuations which occur on short time scales (Blöcker et al., 2016).

To estimate the maximum amplitude that can be distinguished from these fluctuations, we superimpose several artificial amplitudes of reservoir induction signals onto the magnetometer data from the E14 flyby at an altitude of 25 km. We specifically chose this encounter, as the fluctuations were small compared to other flybys. It is also one of the few Galileo orbits that are exempt from large-scale plasma effects. The E14 flyby also does not show any signs of plume activity, which can result in anomalies on the order of 100 nT (Jia et al., 2018; Arnold et al., 2019). Thus, the E14 orbit offers clear identification of induction signals generated within Europa's subsurface. We added artificial dipole signals as generated by a perfectly conducting reservoir with various amplitudes 5, 10, and 20 nT at 25 km to the measurements and found an induction response with a 5 nT amplitude to be distinguishable from most fluctuations within the measurements, which lie at an average of 3 nT (see Figure 4.5). However, individual fluctuations with amplitudes above 5 nT exist in the E14 data and occur on time scales similar to the induction response of a reservoir. Multiple flybys across the same region would be needed to verify such a weak perturbation due to induction from the reservoir, assuming the other small-scale fluctuations are random. An induction signal of 20 nT would be clearly distinguishable from fluctuations, which is also valid for an amplitude of 10 nT. The bottom panel of Figure 4.5 displays a zoom-in of the time interval around the passage of the reservoir. Here, the dipole character of the reservoir's induction response is visible, which is different from the other fluctuations. This might additionally help to separate the apparently random fluctuations from perturbations caused by a reservoir. In future measurements, where indications of an induced signal from a reservoir are present, a number of statistical tests based on the detailed structure of the RMS fluctuations will need to be applied to quantitatively assess such signals.

In Figure 4.6, we present the radial component of the magnetic field B_r that would be measured during a 25 km flyby above a reservoir with a radius of 20 km and a conductivity $\sigma_{\mathrm{res}} = 30\,\mathrm{S/m}$. The radial component B_r is given as the sum of inducing field $B_{\mathrm{J},r}(t)$, given by Equation (4.1), and induced field in ocean and reservoir $B_{\mathrm{ind},r}$, which is given by Equation (4.2). For comparison, we also include the radial component if no reservoir was present and if there was no coupling between ocean and reservoir. We see the induction signal of the reservoir as a small-scale perturbation overlaying the induction signal of the ocean. In this scenario, the coupling effects cause a small enhancement of the reservoir's induction response, resulting in a deviation of approximately 1 nT compared to the induction response of a radially symmetric interior. We calculate the maximum deviation between these two models to obtain information about the potential detectability of local asymmetries within the parameter space discussed in Section 4.1 (Figure 4.7). For large reservoirs, its induction response ranges from $10^{-1} - 10^{-2}$ nT. The induction signature decreases for smaller reservoirs down to orders of 10^{-4} nT. In the low conductivity limit, the induction response at 25 km lies below 10^{-2} nT for all radii. For all reservoir radii and conductivities considered in Figure 4.7, the respective induction responses lie below 5 nT.

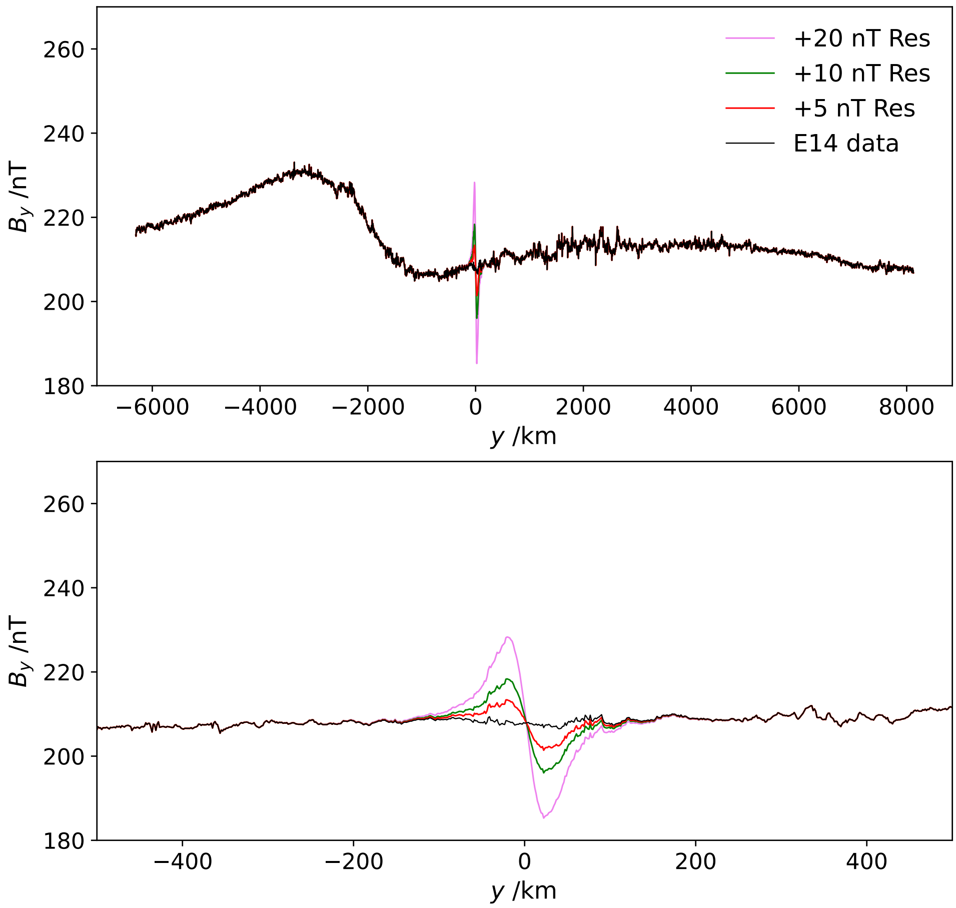

Figure 4.5: Magnetometer measurements of the B_y component during the Galileo E14 flyby (black). Additionally, artificial signals of a perfectly conducting reservoir with 5 nT (red), 10 nT (green), and 20 nT (violet) amplitude at 25 km altitude have been superimposed to the data to test if these signals are distinguishable from the fluctuations. The bottom panel shows a zoom into the 1000 km around C/A to show the reservoir's induction characteristic.

Based on Figure 4.7, at 25 km closest approach, the magnetic field perturbation caused by a local reservoir of liquid water between the ocean and icy surface is too weak to be resolved, as the field strength lies below 5 nT across the entire parameter space considered in this study. Additionally, this induction response will likely not be distinguishable from overlaying plasma effects in the measurements described, for example, in Saur et al. (1998), Schilling et al. (2007, 2008), Blöcker et al. (2016), or Arnold et al. (2020), which are generated by ionospheric interactions with the Jovian magnetosphere and perturb the magnetic field. As the values for all discussed induction responses from the reservoir lie below 5 nT, increasing the limit of detection to account for distinct identification of reservoir signals has no impact on our conclusions.

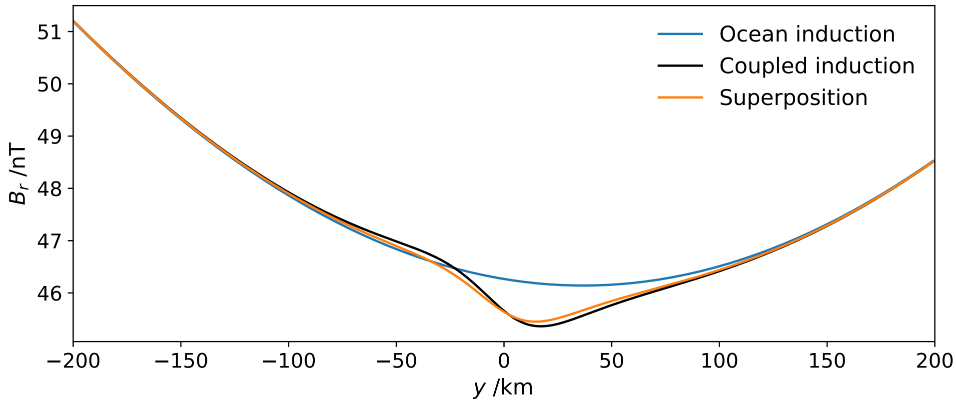

Figure 4.6: Radial component of the sum of inducing and induced magnetic field $B_r = B_{\mathrm{ind},r} + B_{\mathrm{J},r}$, where $B_{\mathrm{ind},r}$ follows Equation (4.2) and $B_{\mathrm{J},r}$ is obtained by considering Equation (4.1) at $\omega t = \pi$, during a hypothetical flyby with 25 km altitude at closest approach with reservoir parameters $\sigma = 30\,\mathrm{S/m}$ and $r_{\mathrm{res}} = 20\,\mathrm{km}$.

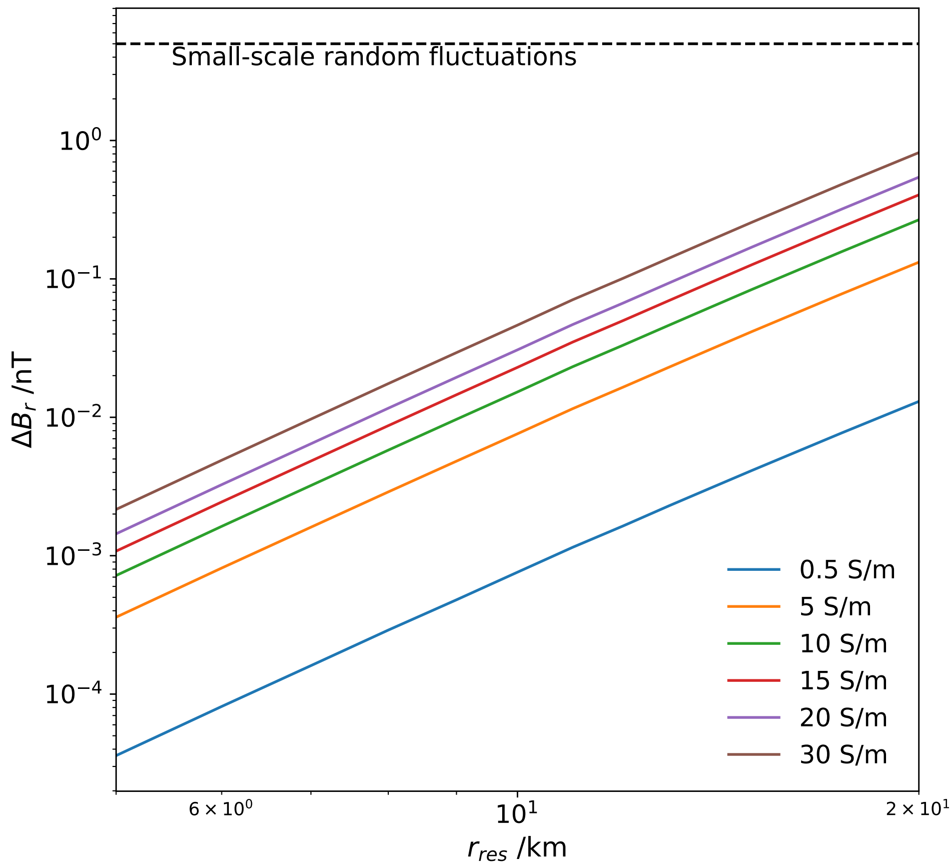

Figure 4.7: Magnetic induction signature caused by reservoir at 25 km altitude as a function of radius for conductivities ranging from 0.5 to 30 S/m. The dashed horizontal line at 5 nT represents the minimum at which reservoirs could be detected with multiple flybys.

4.2.4 Detectability at the Surface

Another potential option for the detection of local asymmetries could be the deployment of stationary magnetometers on Europa's surface, specifically on interesting targets such as chaos regions. This method requires the use of multiple magnetometers to obtain reference values outside the reservoir's reach, e.g., one magnetometer atop the reservoir and a second magnetometer which is positioned at a distance close to the reservoir, where the induction signal of the reservoir is approaching negligible values. For the results presented within this section, the first magnetometer is positioned at $\theta = 90°, \phi = 0°$ in Europa-centered coordinates, directly above the reservoir. The second magnetometer is stationed at $\theta = 90°, \phi = 359°$, which corresponds to a distance of 27.2 km between the two magnetometers. The use of magnetometers allows the recording of time series, which are shown in Figure 4.8. As a comparison, we evaluate the different magnetic fields two magnetometers would measure if only an ocean is present (see Figure 4.9), and find that the deviation is smaller, with a maximum of 1 nT compared to approximately 9 nT if a reservoir with $\sigma_{\mathrm{res}} = 30\,\mathrm{S/m}$ and $r_{\mathrm{res}} = 20\,\mathrm{km}$ is present.

While this difference in measurements of two nearby magnetometers primarily arises due to the rapid decrease of the reservoir's induction response, the spatial variation of the ocean's induction response contributes approximately up to 1 nT to the measured difference. In addition, the plasma effects can be large. We estimate the magnetic field gradient from Europa's plasma interaction based on simulations by Schilling et al. (2008) during the E04 flyby. While simulations made by other authors (see, e.g., Blöcker et al., 2016; Arnold et al., 2020) would allow for such estimates as well, the model conditions assumed in Schilling et al. (2008) resemble our conditions the most due to the similarities between the E04 and E14 flyby, i.e., Galileo performed the flyby near the equatorial plane and Europa was well outside the plasma sheet. Near Europa's equatorial plane, the field varies by approximately 100 nT across one Europan radius, which for this flyby is mostly attributed to the induced field of the subsurface ocean. Thus, the plasma interactions appear to be smaller than induction effects outside the plasma sheet, with a gradient $< 1\,\mathrm{nT/km}$. Inside the plasma sheet, the gradient by plasma interactions is larger, up to approximately $200\,\mathrm{nT}/R_{\mathrm{E}}$.

With the recording of temporal variation at a fixed position, random fluctuations will tend to average out over a long term, e.g., months of observations. To still account for such fluctuations in the measurements, we fit a polynomial of order 4 to 2 hours of E14 data outside the time region of closest approach and find an RMS error of 2.3 nT. However, during times in which Europa is within high density plasma regions, the magnetic field perturbations due to plasma interactions will make any induction signal unresolvable in the measurements. Outside the current sheet, we find that reservoirs with radius below 8 km cannot be detected for all conductivities considered and that reservoirs larger than 8 km require conductivities above $3 - 30\,\mathrm{S/m}$ to lie above the gradient caused by the ocean's induction response (see Figure 4.10). For reservoirs below 12 km, the difference measured by two magnetometers is smaller than the RMS of the fluctuations in the data.

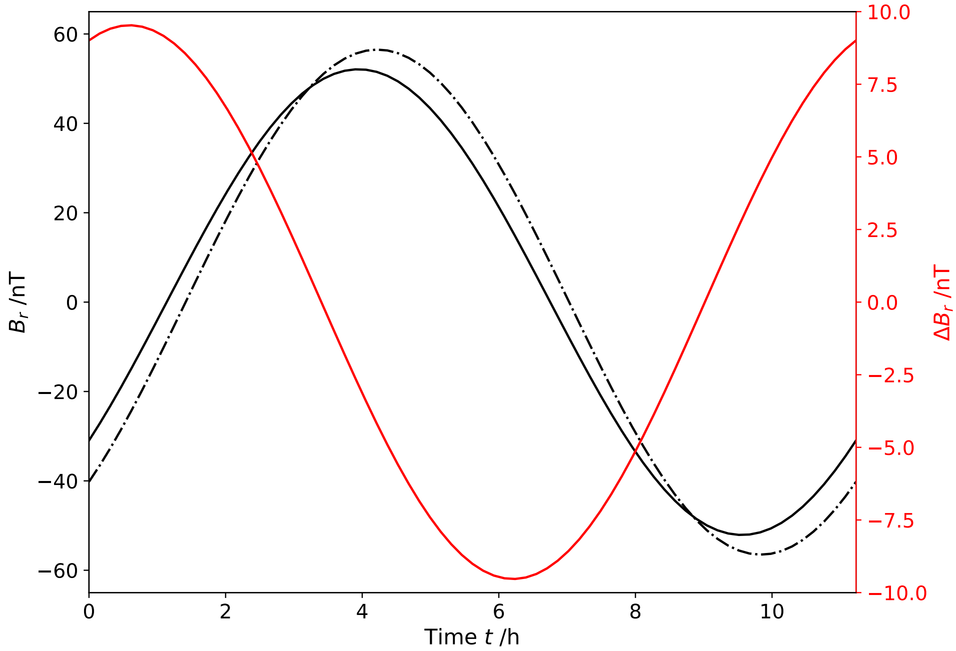

Figure 4.8: Time series of the radial component of the sum of induced and inducing magnetic field (solid, black) on top of a reservoir and 1° in longitude outside a reservoir (dash dotted) for $r_{\mathrm{res}} = 20\,\mathrm{km}$ and $\sigma_{\mathrm{res}} = 30\,\mathrm{S/m}$. The solid red curve and y-axis show the difference between the two calculations.

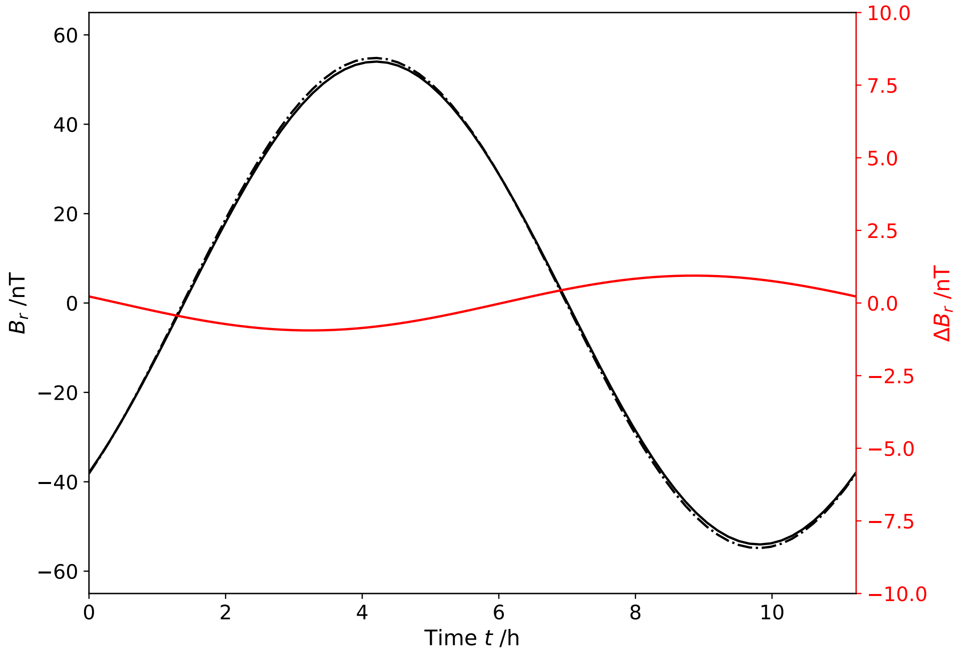

Figure 4.9: Same setup as Figure 4.8, except that in this model only an ocean is present, i.e., there are no local asymmetries.

The three limits for the detectability of a reservoir due to gradients in the induction signal of the ocean, the plasma interaction and small-scale fluctuations discussed in the previous paragraph should be considered upper limits and smaller induction signatures of a reservoir are expected to be detectable. On long time series, periodic contributions can be filtered out and therefore suppressed within a statistically distributed noise, while the gradients due to the plasma interactions and the induced magnetic field from the ocean can be partially accounted for by numerical simulations.

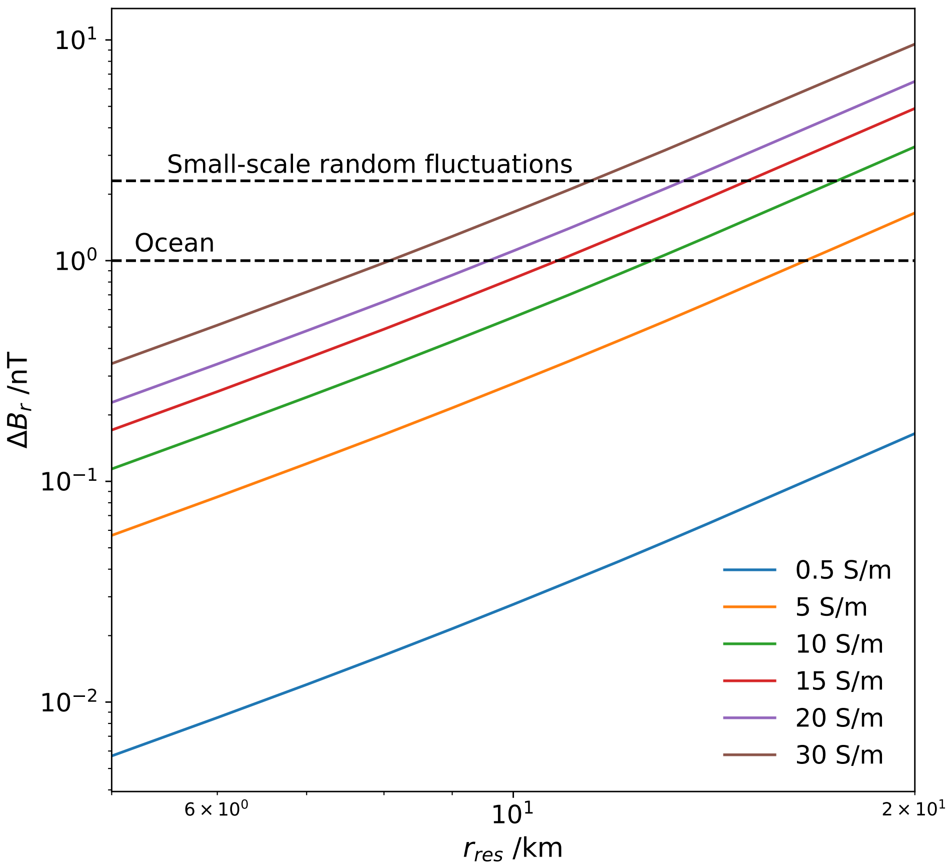

Figure 4.10: Maximum difference caused by the reservoir's induction response between surface measurements taken above a reservoir and 1° in longitude (27.2 km) away from the first magnetometer as a function of reservoir radius for conductivities ranging from 0.5 to 30 S/m. Here, the ocean's induction response has been subtracted from the difference. The dashed horizontal lines mark perturbations caused by the gradient over 27.2 km distance of the ocean's induction response (1 nT) and the RMS at 2.3 nT from random noise in the data, respectively.

4.3 Discussion

We briefly summarize our analytical model and afterward discuss the results presented in Section 4.2, especially with regard to the detectability of reservoirs with future missions.

4.3.1 Analytical Model for Coupled Induction

We constructed an analytical model that accurately describes the electromagnetic coupling and the resulting induced fields between two neighboring spherically symmetric bodies, in this case a global subsurface ocean and a small-scale reservoir within the icy crust. This model is solved numerically using an iterative method to account for the mutual induction between ocean and reservoir. The implementation of coupling effects is crucial for the physical correctness of the calculated fields, and our work provides a new approach to describing these coupled fields. The equations used in this approach assume both conductors to be radially symmetric with a constant conductivity. It is important to consider each multipole moment of the induced field separately as the phase shift is a function of degree l, thus each contribution to the multipole is induced with a varying temporal delay $\phi_l^{\mathrm{ph}}/\omega$. It should be noted that real reservoirs or local conductivity anomalies will not be perfectly spherically symmetric. For complex and arbitrarily shaped conductive structures, no analytical solution of the induction response exists, and the induction response needs to be calculated with full numerical solvers. Such calculations are outside the scope of this work.

4.3.2 Detectability at 25 km Altitude

The detectability of a small-scale reservoir faces multiple challenges. First, the low amplitude of a reservoir due to its small size, as the induction amplitude varies with the square of the radius via Equation (3.25). For a reservoir with radius $r_{\mathrm{res}} = 20\,\mathrm{km}$ and conductivity $\sigma = 30\,\mathrm{S/m}$, its induction amplitude is still just $A_{\mathrm{res}} = 0.15$, while for an ocean such large conductivities would result in a near-perfectly conducting response. If we now assume a perfectly conducting reservoir with $A = 1$ to test its detectability at 25 km, this illustrative scenario highlights the challenge imposed by the coupling processes between ocean and reservoir. Here, the reservoir's dipole response to the Jovian background field gets obscured by the coupled induction response to the ocean's dipole, resulting in a significantly lower induction signature by the reservoir. At 25 km altitude, one would measure a deviation to the symmetric model of approximately 1 nT after coupling processes instead of 8 nT if only the superposition is assumed (superposition refers to considering just the $n = 1$ iteration for both ocean and reservoir). The third issue is the distance to the reservoir, as its induced fields experience a rapid decrease due to its small extension. These fields are dipole dominant and decrease with $(r_{\mathrm{res}}/r)^3$, where $r > 2r_{\mathrm{res}}$ for our cases.

A reservoir might be detectable if its properties lie outside our considered range, i.e., if the reservoir has a higher conductivity or a radius larger than 20 km. A conductivity above the upper limit of 30 S/m could hint at a higher temperature or pressure within the water melt, resulting in an increased conductivity of saline water containing sodium chloride (Guo & Keppler, 2019). Although past studies argued for a magnesium sulfate rich ocean (Kargel et al., 2000; McKinnon & Zolensky, 2003), its conductivities are lower than sodium chloride assuming near-saturation conditions (Hand & Chyba, 2007), and would thus generate weaker magnetic field perturbations. A larger radius will be beneficial for its detectability due to a larger induction amplitude and the slower decrease of the resulting induced field. However, this also implies a deeper ocean, as the icy crust thickness has to be adjusted accordingly. As a deep subsurface ocean lies outside of many of the estimates presented in Section 4.1, we chose not to consider such cases in our study.

4.3.3 Detectability at the Surface

A reservoir can be detected if magnetometers are deployed on Europa's surface, which would be a valuable experiment to include in future missions. For that, one magnetometer would be positioned directly on the region of interest, for example a chaos region. A second magnetometer would be placed right outside the chaos region, where the induction signal of a local water melt below it would approach negligible values. This method allows distinguishing local features from the global depth variabilities of the ocean as considered by Styczinski et al. (2022). While surface measurements also eliminate one of the challenges mentioned in Section 4.3.2 in detecting a reservoir, i.e., the rapid decrease of the induction response with distance, the induction amplitudes remain limited to low values. Thus, in our most conservative case, only reservoirs with a radius larger than $r_{\mathrm{res}} \approx 12\,\mathrm{km}$ and conductivities $\sigma > 7\,\mathrm{S/m}$ are able to generate an induction response where the difference measured by two magnetometers at 27.2 km distance lies above the RMS inferred from the data at times around Galileo's E14 flyby. The recording of temporal variability at a fixed position could, however, allow us to obtain a more profound understanding of the periodicity of the various electromagnetic effects and distinguish them from each other in the time series. With this information, large-scale plasma effects can potentially be subtracted from measurements using numerical models, which would then allow for detection of reservoir signals even in larger-plasma-density regions. Model calculations, where the reservoir placements resemble those of chaos regions on Europa, can be made to compare future measurements with the theoretical results.

4.3.4 Outlook to Future Spacecraft and Lander Missions

Finally, we will discuss our results in the context of the planned Europa Clipper and JUICE spacecraft, as well as highlight the advantages of a surface lander.

Detectability with JUICE

For the JUICE mission, only two flybys at Europa are planned, with altitudes around 400 km (Cappuccio et al., 2022). Assuming a reservoir with a radius of 20 km, its induced field decreases to about 1/8000 of its amplitude at the planned altitude, assuming a simple dipole, equaling to $4 \cdot 10^{-3}\,\mathrm{nT}$ for $\sigma_{\mathrm{res}} = 30\,\mathrm{S/m}$. Thus, JUICE will not be able to detect reservoirs of liquid water with its magnetometer measurements.

Detectability with Europa Clipper

In this work, Europa Clipper has served as a motivation in choosing an altitude of 25 km during a hypothetical flyby, as multiple encounters at that distance are planned. However, assuming a sensitivity limit of 5 nT, the induction signals of a reservoir are too weak to be resolved with magnetometer measurements. If the measurements would have significantly smaller fluctuations than those measured during the E14 flyby, then the sensitivity could be lower than 5 nT as well. This potentially allows the detection of large and highly conductive reservoirs.

Detectability with Landers

We have shown that reservoirs are expected to be detectable at the surface if Europa is outside the plasma sheet, providing additional scientific capabilities to consider for future plans for lander missions, which have been the subject of discussion over the last years (see, e.g., Pappalardo et al., 2013; Blanc et al., 2020; Hand et al., 2022). Additionally, the idea of a magnetometer network across Europa's surface offers an interesting approach to map spatial variabilities, e.g., depth variabilities between the polar and equatorial regions. Such a network of surface magnetometers would be highly valuable to investigate multiple chaos regions suspect to the existence of water pockets and help in the understanding of their formation.

4.3.5 Concluding Remarks

In this work, we investigated the joint induction response of two spherically symmetric, electrically conducting bodies, i.e., an ocean and a reservoir. We provided an analytical model that is solved using a numerical, iterative method and calculated the total induction response of the coupled system across the chosen parameter space for the reservoir's radius and conductivity. These induced magnetic fields have been investigated for their detectability at altitudes equal to the planned JUICE and Europa Clipper spacecraft flybys, where for Europa Clipper the minimum flyby altitude of 25 km has been chosen. With the JUICE spacecraft, reservoirs cannot be detected with magnetometer measurements, whereas Europa Clipper might be able to resolve large and highly conductive reservoirs assuming small random fluctuations at the time of the flybys. Liquid water reservoirs are likely detectable at Europa's surface using a network of magnetometers, offering a valuable outlook to future lander missions. The presented study is therefore a first step toward understanding the induction response and the detectability of local near-surface anomalies within Europa's icy crust by induction sounding.

5

A Quantitative Approach to Constrain Europa's Ocean

In Chapter 3, we have described how the induction method can be used to indirectly probe Europa's interior, specifically its subsurface ocean, as its electromagnetic response to the time-varying component of Jupiter's magnetic field is a function of its depth, thickness, and electrical conductivity. In this chapter, we present a method with which we quantitatively characterize these three properties and their constraints. This is done by performing an inversion of magnetic field measurements recorded with the Galileo spacecraft. Here, we also take into account the model uncertainties introduced by the models for the individual contributions to the magnetic field model, the inducing magnetic field, the Jovian magnetospheric background field, and the magnetic field due to Europa's plasma interaction. These uncertainties are estimated before the inversion is performed. Afterward, we

The study in this chapter is a manuscript that is currently in preparation, with Jason Winkenstern as leading author and Joachim Saur and Sebastian Cervantes as co-authors. The research objective has been developed together with Joachim Saur. The MHD simulations needed to describe the magnetic field due to Europa's plasma interaction were carried out by Sebastian Cervantes.

5.1 Methods

The magnetic field at Europa $\mathbf{B}_{\mathrm{model}}$ can be described as the sum of three contributions

$$\mathbf{B}_{\mathrm{model}} = \mathbf{B}_{\mathrm{bg}} + \mathbf{B}_{\mathrm{ind}} + \mathbf{B}_{\mathrm{plasma}}, \tag{5.1}$$

where $\mathbf{B}_{\mathrm{bg}}$ is the Jovian magnetospheric background field, $\mathbf{B}_{\mathrm{ind}}$ is the induced magnetic field generated within Europa's subsurface ocean, and $\mathbf{B}_{\mathrm{plasma}}$ is the magnetic field due to

Europa's plasma interaction. The modelled magnetic field is compared against observations recorded along the spacecraft's trajectory $\mathbf{B}_{\mathrm{obs}}(\mathbf{r})$. A phenomenological sketch of the problem is shown in Figure 5.1. Subtracting the background and plasma fields from the observed magnetic field, we assume the residual field represents the induced field within the measurements, referred to as the "observed induction response" $\mathbf{B}_{\mathrm{obs,ind}}$ in this study

$$\mathbf{B}_{\mathrm{obs,ind}} = \mathbf{B}_{\mathrm{obs}} - \mathbf{B}_{\mathrm{bg}} - \mathbf{B}_{\mathrm{plasma}}. \tag{5.2}$$

Using the ocean properties as model parameters, we perform an inversion to determine which combinations of (d, h, σ) appropriately reproduce the measurements. Here, we do not only provide a "best-fit", i.e., the ocean properties where $||\mathbf{B}_{\mathrm{model}}(d, h, \sigma) - \mathbf{B}_{\mathrm{obs}}||^2$ is minimum, but also characterize their uncertainties. This is done by performing a chi-squared analysis, in which $||\mathbf{B}_{\mathrm{model}}(d, h, \sigma) - \mathbf{B}_{\mathrm{obs}}||^2$ is weighted against a given uncertainty. Rather than the uncertainty in the spacecraft measurements, it is the assumptions in the model descriptions of the individual contributions that control the overall uncertainty used to calculate chi-squared. A prescribed criterion of $\chi^2 \leq 1$ provides uncertainties on the ocean properties in the form of a range, e.g., $d \in [d_{\mathrm{lower}}, d_{\mathrm{upper}}]$, in which these properties can lie.

In this section, we introduce the models with which we describe the individual contributions to the modelled magnetic field. Due to assumptions made within each model, these descriptions are not an exact representation of the real magnetic field in Europa's environment. We quantify the uncertainties that are introduced as a consequence of our assumptions. Afterward, we present the chi-squared analysis with which these uncertainties are used to characterize both the ocean properties and their uncertainties in a quantitative manner.

5.1.1 Inducing and Induced Magnetic Field Model

The induced field is the direct electromagnetic response to the inducing field. As such, any uncertainty in the model of the inducing field directly propagates into the induced field. Here, we present the inducing field model and quantify its underlying uncertainty. Afterward, we investigate the uncertainty propagation into the induced field.

Inducing Field Model

Considering only the inducing frequency ω corresponding to the synodic rotation period $T = 11.23\,\mathrm{h}$, we assume that the inducing field is confined to the xy-plane and homogeneous in Europa's vicinity. This leads to the following description of the external Gauss coefficients (q, s) of the inducing field

$$\begin{aligned} q(t) &= \Re\left\{q_0 e^{i(\omega t - \phi_0 - \phi_x)}\right\} \\ s(t) &= \Re\left\{s_0 e^{i(\omega t - \phi_0 - \phi_y)}\right\}, \end{aligned} \tag{5.3}$$

with the inducing amplitudes $q_0 = -B_{0,x}$ and $s_0 = -B_{0,y}$, phase of the inducing field $\phi_0 = 200°$ (Schilling et al., 2007), and additional phases of the individual components

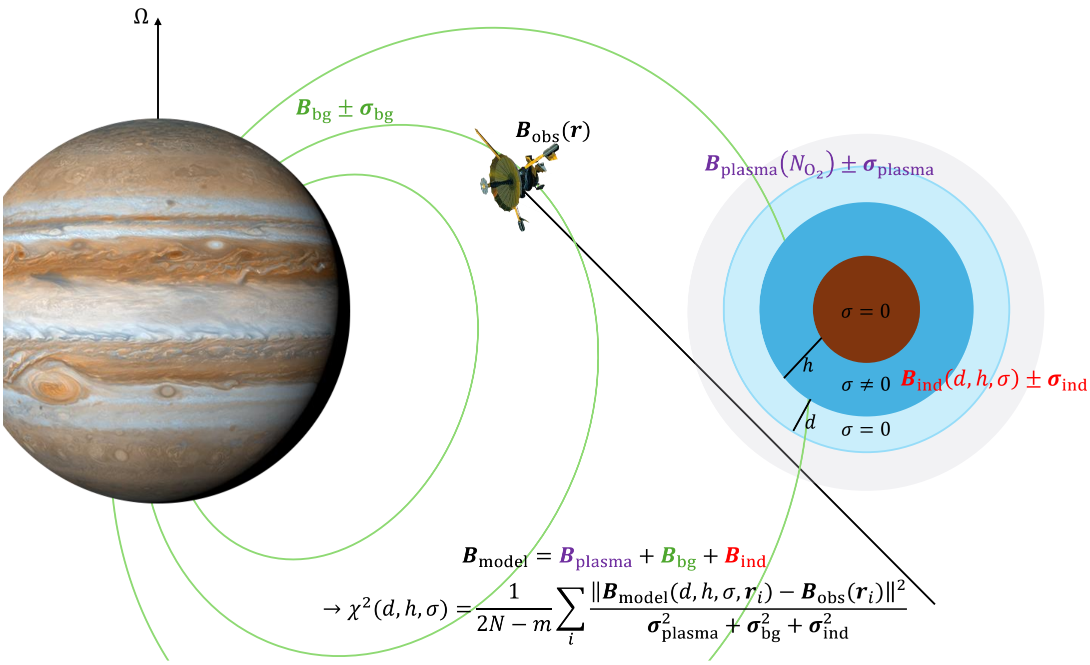

Figure 5.1: Sketch of the problem. The tilt of Jupiter's dipole component with respect to its rotational axis Ω induces a magnetic field within Europa's subsurface ocean (dark blue) $\mathbf{B}_{\mathrm{ind}}(d, h, \sigma)$, which is surrounded by a non-conductive icy crust (bright blue) and underlying mantle material (brown). The induced field is a function of the ocean properties investigated in this work. Besides the induced field, Jupiter's background field $\mathbf{B}_{\mathrm{bg}}$ is additionally perturbed by the plasma interaction between Europa's atmosphere (gray layer) and the Jovian magnetosphere $\mathbf{B}_{\mathrm{plasma}}$, where the strength varies with the O_2 column density N_{O_2}, among other factors. These three contributions build our magnetic field model, as described by Equation (5.1). To quantify the ocean properties, we perform an inversion with the goal to minimize the misfit between the model and measurements made by the Galileo spacecraft along its trajectory $\mathbf{B}_{\mathrm{obs}}(\mathbf{r})$ (black line). Due to assumptions in the model descriptions of background field, inducing field, and plasma interaction, uncertainties are introduced, which are characterized and utilized to derive the ocean properties and their constraints by employing a chi-squared analysis.

Table 5.1: Inducing amplitude at the synodic rotation period. Values between the two references vary as different models for the internal and external contributions to Jupiter's magnetic field have been used.

	Seufert et al. (2011)	Vance et al. (2021)
B_x [nT]	66.3	75.55
B_y [nT]	216.6	209.78

$\phi_x = 90°, \phi_y = 0°$. We employ the EPhiO coordinate system, where z is parallel to Jupiter's rotational axis, y points toward Jupiter, and x completes the right-handed system (pointing approximately in the direction of corotational flow). We note that recent work favors the use of Europa IAU coordinates (e.g., Styczinski et al., 2022; Biersteker et al., 2023), however, with past studies on the Galileo flybys also performed in EPhiO coordinates, we follow that approach.

This study focuses on the measurements recorded during the E14 flyby. As such, we chose values for q_0 and s_0 that best reproduce the values obtained with the magnetospheric model by Khurana (1997) at the System III longitude at which the E14 flyby occurred ($\lambda_{\text{III}} = 184.3°$). From this approach, it follows $q_0 = -37\,\text{nT}$ and $s_0 = -222\,\text{nT}$.

Uncertainty of the Inducing Field

The values for the inducing field amplitudes q_0 and s_0 are estimated using a magnetospheric model which includes both Jupiter's intrinsic field, as well as contributions from magnetospheric currents, rather than exclusively the dipole term of Jupiter's intrinsic field. The strength of the inducing amplitude at a given period can be determined by performing a Fourier analysis of the modelled magnetic field over a long time series (Seufert et al., 2011; Vance et al., 2021). The values for the inducing amplitude at the synodic rotation period are given in Table 5.1. We approximate the uncertainty of the inducing amplitude at the synodic rotation period ($\sigma_{q_0}, \sigma_{s_0}$) as the difference between the values obtained by Seufert et al. (2011) and Vance et al. (2021), which yields $\sigma_{q_0} = 9.3\,\text{nT}$ and $\sigma_{s_0} = 6.3\,\text{nT}$. From that, the uncertainty of the external coefficients can be calculated as

$$\begin{aligned} \sigma_q(t) &= \Re\left\{\sigma_{q_0} e^{i(\omega t - \phi_0 - \phi_x)}\right\} \\ \sigma_s(t) &= \Re\left\{\sigma_{s_0} e^{i(\omega t - \phi_0 - \phi_y)}\right\}. \end{aligned} \tag{5.4}$$

Induced Field Description

The internal Gauss coefficients (g_1^1, h_1^1) of the induced field are related to the external Gauss coefficients via

$$\begin{aligned} g_1^1 &= Qq \\ h_1^1 &= Qs, \end{aligned} \tag{5.5}$$

with the Q-response $Q = Ae^{i\phi^{\text{ph}}}$. For a conductive shell with outer radius r_0 and inner radius r_1, the induction amplitude A and phase shift ϕ^{ph} can be obtained by considering the ratio between the complex coefficients of the induced and inducing field $B_{\mathrm{i},l}$ and $B_{\mathrm{e},l}$ (Zimmer et al., 2000 for degree $l = 1$, Saur et al., 2009 for arbitrary l)

$$\left(\frac{B_\mathrm{i}}{B_\mathrm{e}}\right)_l = -\frac{l}{l+1}\frac{\xi J_{l+3/2}(r_0 k) - J_{-l-3/2}(r_0 k)}{\xi J_{l-1/2}(r_0 k) - J_{-l+1/2}(r_0 k)}, \tag{5.6}$$

with

$$\xi = \frac{r_1 k J_{-l-3/2}(r_1 k)}{(2l+1) J_{l+1/2}(r_1 k) - J_{l-1/2}(r_1 k)}, \tag{5.7}$$

where k is the complex wave number with $k^2 = i\mu_0\omega\sigma$ and $J_\nu(z)$ are the Bessel functions of first kind and order ν with complex argument z. We note that the use of the wave number $k^2 = -i\mu_0\omega\sigma$ in Parkinson (1983) results in the modified Bessel differential equation, for which the solutions are the modified Bessel functions $I_\nu(z)$. Parkinson (1983), however, used the standard Bessel functions, resulting in positive values for the phase shift. From Equation (5.6), the induction amplitude and phase shift can be calculated as $A = \mathrm{abs}(B_\mathrm{i}/B_\mathrm{e})(r_0/r_\mathrm{m})^3$ and $\phi^{\mathrm{ph}} = \arg(B_i/B_e)$, respectively. The induction amplitude ranges from 0 to $l/(l+1)$, or 0 to 1 after multiplying with $(l+1)/l$, which is how the induction amplitude is commonly given in the literature. With our definition of the wave number k, the phase shift is negative, ranging from $-\pi/2$ to 0. For a conductor extending to the surface of the satellite with radius r_m and $\sigma \to \infty$, $A = 1$ and $\phi^{\mathrm{ph}} = 0$.

Assuming that the induced field is transported via the electromagnetic mode, i.e., the conductivity in Europa's icy crust and the surrounding environment is $\sigma = 0$, it can be described by a potential Φ of the form

$$\Phi(r,\theta,\phi) = R_\mathrm{E}\left(\frac{R_\mathrm{E}}{r}\right)^2 \sin\theta\left(g_1^1\cos\phi + h_1^1\sin\phi\right), \tag{5.8}$$

with Europa's mean radius $R_\mathrm{E} = 1561\,\mathrm{km}$ (Nimmo et al., 2007), colatitude θ, and longitude ϕ. The individual components are calculated via $\mathbf{B}_{\mathrm{ind}} = -\nabla\Phi$ and read

$$\begin{aligned}
B_{\mathrm{ind},r}(r,\theta,\phi) &= 2\left(\frac{R_\mathrm{E}}{r}\right)^3 \sin\theta\left(g_1^1\cos\phi + h_1^1\sin\phi\right)\\
B_{\mathrm{ind},\theta}(r,\theta,\phi) &= -\left(\frac{R_\mathrm{E}}{r}\right)^3 \cos\theta\left(g_1^1\cos\phi + h_1^1\sin\phi\right)\\
B_{\mathrm{ind},\phi}(r,\theta,\phi) &= \left(\frac{R_\mathrm{E}}{r}\right)^3 \left(g_1^1\sin\phi - h_1^1\cos\phi\right)
\end{aligned} \tag{5.9}$$

Uncertainty of the induced field

Assuming Gaussian error propagation, the uncertainty of the external Gauss coefficients forward propagates into the internal Gauss coefficients via Equation (3.29) as

$$\begin{aligned}
\sigma_g &= Q\sigma_q\\
\sigma_h &= Q\sigma_s.
\end{aligned} \tag{5.10}$$

Their uncertainty propagates further into the induced magnetic field. The uncertainty for the j-th component of the induced field reads

$$\sigma_{\mathrm{ind},j}(r,\theta,\phi) = \sqrt{\left(\frac{\partial B_{\mathrm{ind},j}(r,\theta,\phi)}{\partial g_1^1}\right)^2 \sigma_g^2 + \left(\frac{\partial B_{\mathrm{ind},j}(r,\theta,\phi)}{\partial h_1^1}\right)^2 \sigma_h^2}. \tag{5.11}$$

For the System III longitude of the E14 flyby, $\lambda_{\mathrm{III}} = 184.3°$, the internal Gauss coefficients g_1^1 and h_1^1 and their associated uncertainties are given in conductivity-thickness space for a depth of 0 km, i.e., an ocean directly at the surface, in Figure 5.2 (c-f). In Figure 5.2 (a) and (b), we also show the induction amplitude A and phase shift ϕ^{ph} to highlight their aforementioned non-uniqueness.

5.1.2 Jovian Magnetospheric Background Field

To compare the modelled induced magnetic field with the data, the Jovian background field must be removed from the measurements. We approximate Jupiter's contribution to the measured magnetic field by fitting a third degree polynomial to the portions of the flyby in which the perturbations due to induction and plasma interaction are smaller than 1.5 nT (Figure 5.3), motivated by the precision of the Europa Clipper magnetometer (Kivelson et al., 2023). While this work does not relate directly to Europa Clipper, this value provides a benchmark. Values larger than 1.5 nT would result in more remnant plasma magnetic fields in the fitting window, thus less representative background fits. A lower value would extend the overall time span of considered measurements, thus decreasing the quality of our fit, as a polynomial fit cannot reproduce the periodicity of the Jovian background field. To assess the length of the intervals used to calculate the background fit, we consider the root-mean-square deviation (RMS) between the data and background fits calculated with varying interval lengths from 15 to 60 minutes (Figure 5.4)

$$RMS_{\mathrm{bg}}(\Delta t) = \sqrt{\frac{1}{3N}\sum_{i=1}^{N}\left(\mathbf{B}_{\mathrm{obs}}(\mathbf{r}_i) - \mathbf{B}_{\mathrm{bg}}(\mathbf{r}_i,\Delta t)\right)^2}, \tag{5.12}$$

where N is the number of measurements, $\mathbf{r}_i$ is the spacecraft position at the i-th measurement, and $\mathbf{B}_{\mathrm{bg}}(\mathbf{r}_i,\Delta t)$ is the background fit calculated with interval length Δt. We do not consider intervals shorter than 15 minutes, as they would produce background fits that are not representative of the variabilities of the Jovian background field on scales of the flyby. In addition, remnant plasma interaction in the fitting window might not be averaged out if the chosen interval length is smaller, as our criterion only limits the strength of the plasma interaction field to less than 1.5 nT, but not strictly zero. This could result in a fit that is not solely controlled by the Jovian background field. This investigation shows that a polyfit with 15-minute window length produces the best-fit background, i.e., the one with minimal RMS. The resulting background fit is shown in Figure 5.5, with $RMS_{\mathrm{bg}} = 0.64$ nT across all three components. The RMS characterizes the uncertainty of the background model, $\sigma_{\mathrm{bg}} = RMS_{\mathrm{bg}}$.

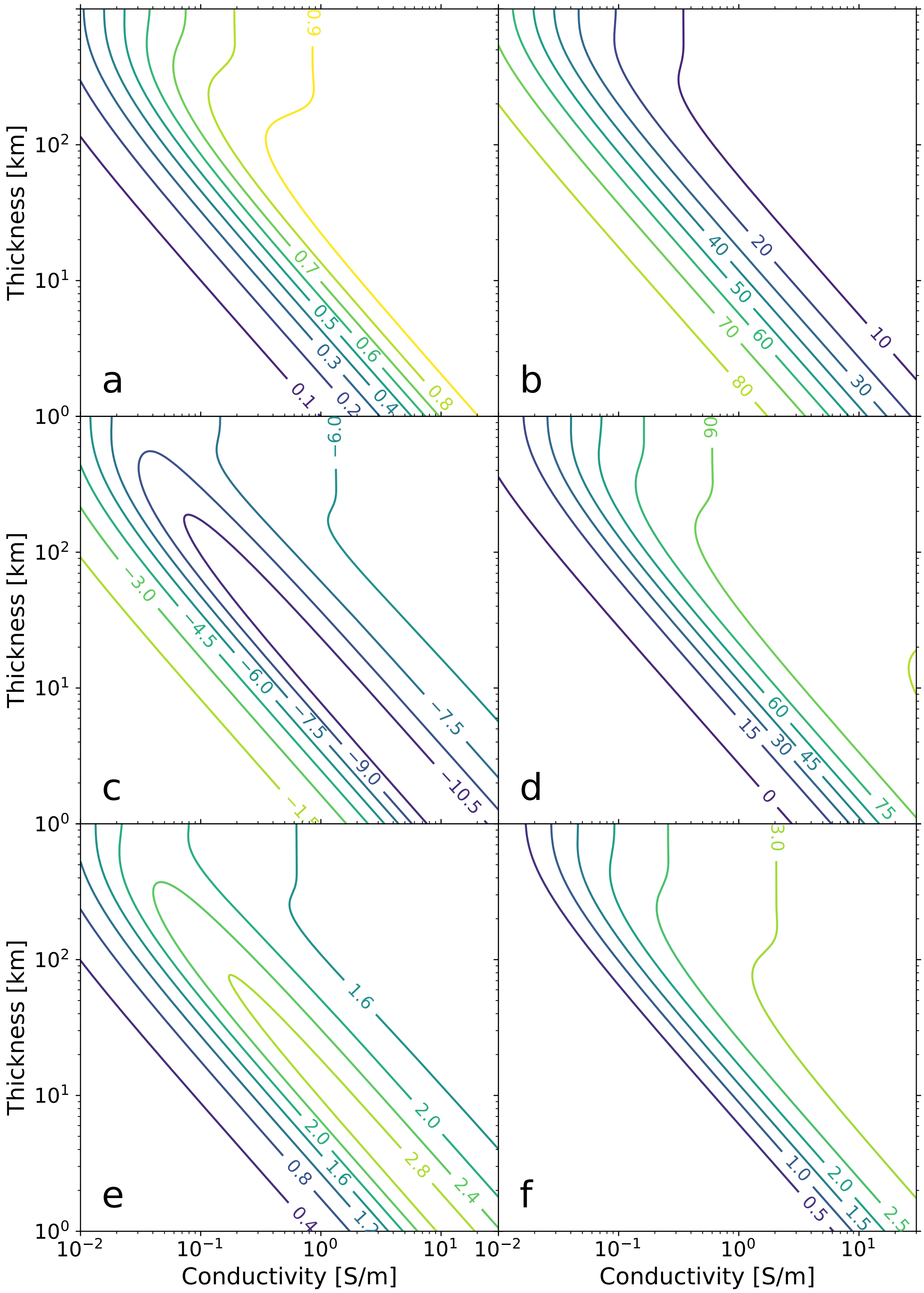

Figure 5.2: In conductivity-thickness space, for an ocean depth $d = 0\,\mathrm{km}$, we show (a) induction amplitude A for degree $l = 1$ and (b) phase shift ϕ^{ph} for $l = 1$, given in degrees. The internal Gauss coefficients (c) g_1^1 and (d) h_1^1, as well as their uncertainties (e) σ_g and (f) σ_h are given in nT. The Gauss coefficients and their uncertainties were calculated for System III longitude $\lambda_{\mathrm{III}} = 184.3°$.

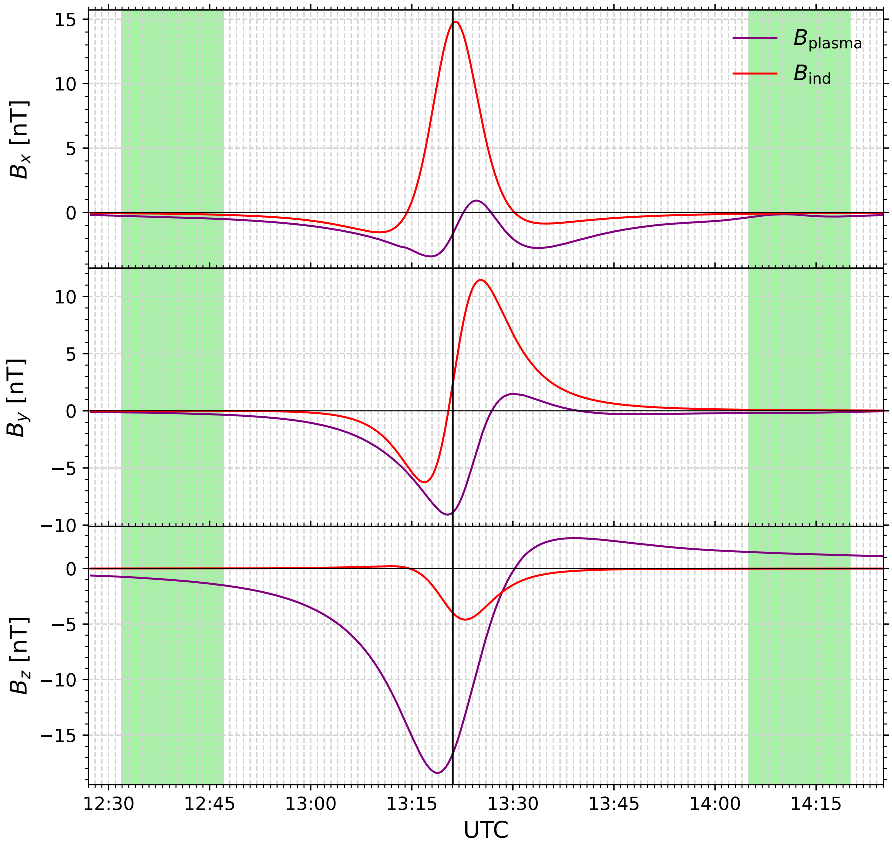

Figure 5.3: Modelled magnetic field due to plasma interaction with Europa's atmosphere (purple) and induction response (red) for the E14 flyby. Moving outward from closest approach (black vertical line), the green intervals begin when the magnetic field signatures are smaller than 1.5 nT and cover a range of 15 minutes.

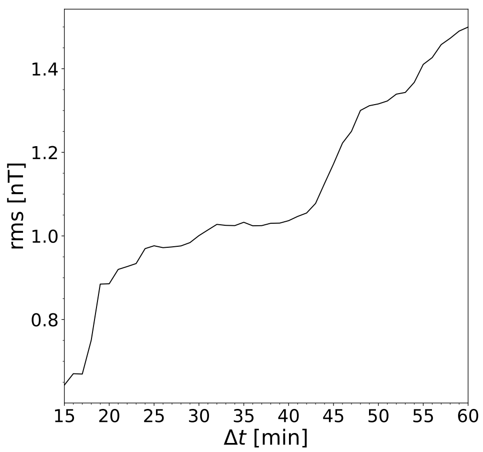

Figure 5.4: Root-mean-square deviation (RMS) of background fits with varying window length Δt for the E14 flyby. The RMS has been calculated across all three components of the magnetic field.

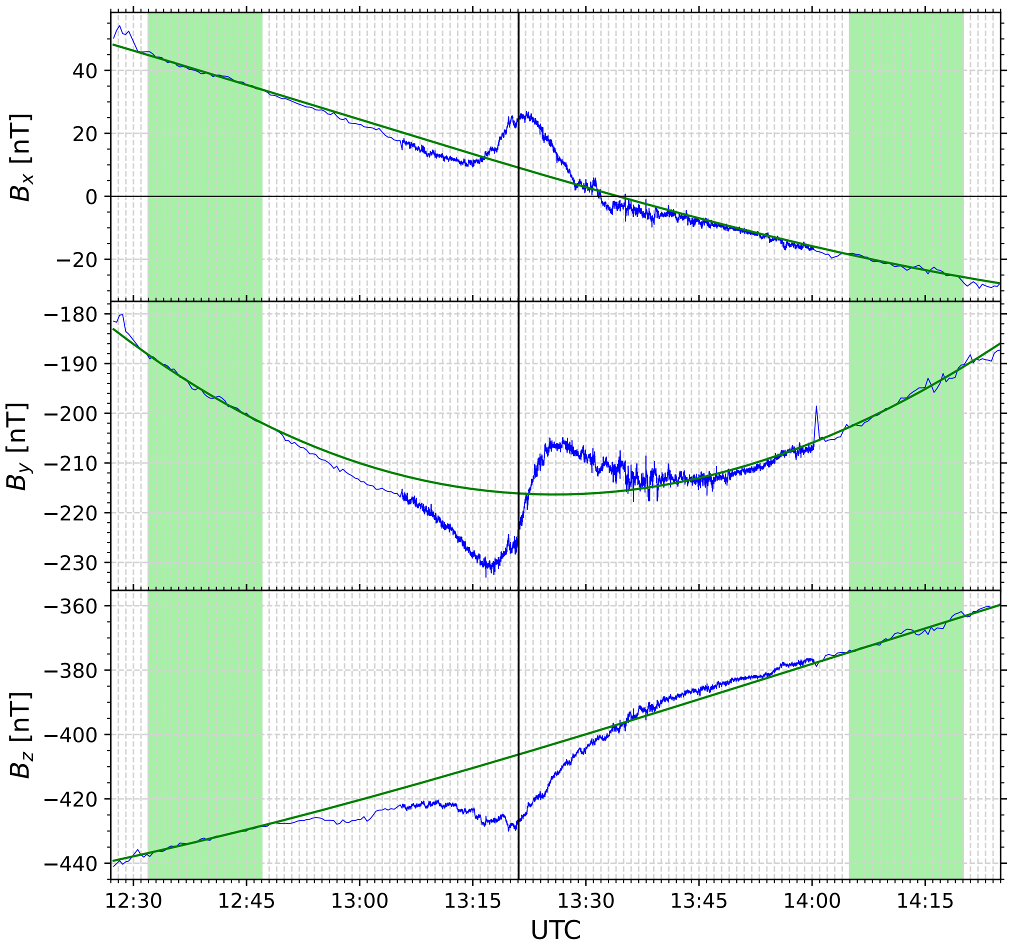

Figure 5.5: Polynomial fit (green) to the components of the measured magnetic field (blue). The light green area indicates the respective 15-minute windows used to calculate the fit.

5.1.3 Plasma Interaction Model

To model the plasma interaction at Europa, we solve the three-dimensional single-fluid magnetohydrodynamic (MHD) equations for the conditions during the E14 flyby using the PLUTO code (Mignone et al., 2007). This code has been used by Duling et al. (2022) to model the plasma interaction of Ganymede.

Model Setup

The MHD equations govern the plasma mass density ρ, plasma bulk velocity $\mathbf{v}$, magnetic field $\mathbf{B}$, and the total energy E_t. For each variable, an evolution equation is stated

$$\begin{aligned}
\frac{\partial \rho}{\partial t} + \nabla \cdot (\rho \mathbf{v}) &= P m_\mathrm{n} - L m_\mathrm{L}, && (5.13)\\
\frac{\partial \rho \mathbf{v}}{\partial t} + \nabla \cdot \left[\rho \mathbf{v}\mathbf{v} - \frac{1}{\mu_0}\mathbf{B}\mathbf{B} + \mathbf{I}\left(p + \frac{1}{2}\frac{B^2}{\mu_0}\right)\right] &= -\left(L m_\mathrm{L} + \nu_\mathrm{n}\rho\right)\mathbf{v}, && (5.14)\\
\frac{\partial \mathbf{B}}{\partial t} - \nabla \times (\mathbf{v} \times \mathbf{B}) &= 0, && (5.15)\\
\frac{\partial E_\mathrm{t}}{\partial t} + \nabla \cdot \left[\left(E_\mathrm{t} + p + \frac{1}{2}\frac{B^2}{\mu_0}\right)\mathbf{v} - \frac{1}{\mu_0}\mathbf{B}\left(\mathbf{v}\cdot\mathbf{B}\right)\right] &= -\frac{1}{2}\left(L m_\mathrm{L} + \nu_\mathrm{n}\rho\right) v^2 \\
&\quad -\frac{3}{2}\left(L m_\mathrm{L} + \nu_\mathrm{n}\rho\right)\frac{p}{\rho} && (5.16)\\
&\quad +\frac{3}{2}\left(P m_\mathrm{n} + \nu_\mathrm{n}\rho\right)\frac{k_\mathrm{B} T_\mathrm{n}}{m_\mathrm{n}}.
\end{aligned}$$

with plasma production and loss rates P and L, respectively, ion-neutral collision frequency ν_n, and thermal pressure p. The initial values of the magnetic field and bulk velocity are $\mathbf{B}_0 = (5, -213, -409)\,\mathrm{nT}$ and $v_0 = 100\,\mathrm{km/s}$ in corotational direction. Our model includes electron impact ionization as the dominant ionization process in Europa's atmosphere (Saur et al., 1998), and we assume an ionization rate of $f_\mathrm{imp} = 10^{-6}\,\mathrm{s}^{-1}$, in the lower limit of the range provided by Smyth and Marconi (2006). This results in a production rate P of

$$P = f_\mathrm{imp} n_\mathrm{n}, \tag{5.17}$$

where n_n is the neutral O_2 number density. Therefore, in the model we take into account the production of singly charged O_2^+ and furthermore assume $m_\mathrm{n} = m_\mathrm{L} = 32\,\mathrm{u}$. We consider a radially symmetric atmosphere and describe its number density profile $n_{O_2}(z)$ as

$$n_{O_2}(z) = n_{0,O_2} e^{-\frac{z}{H}}, \tag{5.18}$$

with surface number density n_{0,O_2}, height z, and scale height H. We consider plasma loss due to dissociative recombination between ions and electrons, where we employ a recombination rate coefficient of

$$\alpha_{\mathrm{rec},O_2^+} = 2 \cdot 10^{-7} \left(\frac{300}{T_\mathrm{e}}\right)^{0.7} \mathrm{cm}^3/\mathrm{s}, \tag{5.19}$$

which has also been used in, e.g., Saur et al. (1998) and Blöcker et al. (2016). For the electron temperature T_e, we use the ionospheric electron temperature of 0.5 eV. Analogous to Duling et al. (2022), we employ the following expression for the loss rate L

$$L = \begin{cases} \alpha\rho\,(\rho - \rho_0)\, m_{\mathrm{L}}^{-2} & \text{for } \rho > \rho_0 \\ 0 & \text{for } \rho < \rho_0 \end{cases}. \tag{5.20}$$

We model collisions between ions and neutrals using the collision frequency

$$\nu_{\mathrm{O_2}} = \sigma_{\mathrm{O_2}} v_0 n_{\mathrm{O_2}}, \tag{5.21}$$

where $\sigma_{\mathrm{O_2}} = 2 \cdot 10^{-15}\,\mathrm{cm}^2$ is the O_2 cross section, similar to Saur et al. (1998). Lastly, the MHD model includes electromagnetic induction in Europa's subsurface ocean through boundary conditions given by Duling et al. (2014). These boundary conditions state that toroidal contributions to the magnetic field need to vanish at the insulating boundary and furthermore state a first order differential equation for the poloidal contributions.

As Figure 5.3 indicates, the perturbations in the B_z-component are dominated by plasma interaction. This is because the inducing field is confined to the xy-plane and the E14 flyby occurred near the equatorial plane. As such, we use the B_z-component to assess which column density, $N_{\mathrm{O_2}} = n_{0,\mathrm{O_2}} H$, best describes the measurements of the E14 flyby. This approach yields an O_2 column density of $N_{\mathrm{O_2}} = 4 \cdot 10^{14}\,\mathrm{cm}^{-2}$.

Uncertainty of the Plasma Interaction

Similar to our approach of using the B_z-component to determine which column density yields the best agreement with the observations, we use it as a proxy to estimate the model uncertainty of the MHD model by calculating the RMS between the "observed plasma perturbation" $\mathbf{B}_{\mathrm{obs,plasma}} = \mathbf{B}_{\mathrm{obs}} - \mathbf{B}_{\mathrm{bg}} - \mathbf{B}_{\mathrm{ind}}$ and the model

$$\sigma^2_{\mathrm{plasma}} = \frac{1}{N} \sum_{i=1}^{N} \left(B_{\mathrm{obs,plasma},z}(\mathbf{r}_i) - B_{\mathrm{plasma},z}(\mathbf{r}_i) \right)^2, \tag{5.22}$$

where N is the number of measurements. We confine the calculation of the MHD model uncertainty to measurements where Galileo was within four Europa radii relative to the satellite's center. In a first order approximation, the uncertainty is assumed to be symmetrical, i.e., it is equal in all three components. Note that this uncertainty measure requires us to specify the ocean properties to subtract the induced field in the B_z-component. As such, the estimate for the plasma uncertainty will change as a function of the ocean model. We first use a reference ocean model with depth $d = 25\,\mathrm{km}$, thickness $h = 100\,\mathrm{km}$, and conductivity $\sigma = 1\,\mathrm{S/m}$ to calculate the induced field, similar to values used in Schilling et al. (2007). After performing the chi-squared analysis, we recalculate the plasma uncertainty, using the induction response of a "best fit" ocean, i.e., where the deviation to the data is minimum (see Section 5.1.4).

5.1.4 Chi-Squared Analysis

After evaluating the uncertainties of our models for the individual contributions to Europa's magnetic field environment in Equations (5.11), (5.12), and (5.22), we perform a chi-squared analysis to find all induction models that appropriately reproduce the observed induction response described by Equation (5.2). We construct a 3D parameter space for the ocean's depth d, thickness h, and conductivity σ. For each combination of (d, h, σ), we calculate the ocean's induction amplitude, phase shift, and the resulting induced magnetic field. We evaluate the corresponding chi-squared value using

$$\begin{aligned}\chi^2(d,h,\sigma) = \frac{1}{2N-m}\sum_{i=1}^{N}\Bigg(&\frac{\left(B_{\text{obs,ind,x}}(\mathbf{r}_i) - B_{\text{ind,x}}(d,h,\sigma,\mathbf{r}_i)\right)^2}{\sigma^2_{\text{bg,x}} + \sigma^2_{\text{plasma}} + \sigma^2_{\text{ind,x}}(\mathbf{r}_i)} \\ &+ \frac{\left(B_{\text{obs,ind,y}}(\mathbf{r}_i) - B_{\text{ind,y}}(d,h,\sigma,\mathbf{r}_i)\right)^2}{\sigma^2_{\text{bg,y}} + \sigma^2_{\text{plasma}} + \sigma^2_{\text{ind,y}}(\mathbf{r}_i)}\Bigg),\end{aligned} \tag{5.23}$$

where N is the number of measurements and $m = 3$ the number of model parameters. We only use the B_x and B_y-components to evaluate χ^2 and we only include measurements where Galileo was within four Europa radii relative to Europa's center, as suggested by Kivelson et al. (2023). Any combination of values for (d, h, σ) that results in $\chi^2 \leq 1$ is labelled a good fit to the data, given the considered uncertainties (Bevington & Robinson, 2003). Assuming Gaussian distributed errors, a $\chi^2 \leq 1$ will mean that our fit, on average, deviates less than one standard deviation from the measurements. The resulting parameter space for (d, h, σ) that fulfills $\chi^2 \leq 1$ gives us constraints on the properties of Europa's subsurface ocean. The combination of (d, h, σ), where χ^2 is minimum yields the best-fit, i.e., the ocean model that yields the best agreement with the observations within our prescribed parameter space.

5.1.5 Parameter Space (d, h, σ)

We calculate χ^2 as a function of the ocean properties (d, h, σ). We do so in a prescribed parameter space, spanning a 3D grid with depth $d \in [1, 150]$ km, thickness $h \in [1, 150]$ km, and electrical conductivity $\sigma \in [0.01, 10]$ S/m. We employ 50 log-spaced grid points along the thickness and conductivity axes and 100 along the depth axis. The parameter space is aimed to explore the range of existing estimates of the total thickness of the H_2O shell (Anderson et al., 1998), as well as the ocean's electrical conductivity (Zimmer et al., 2000; Schilling et al., 2007; Pan et al., 2020, 2021; Vance et al., 2021). Our prescribed depth covers a broad range of estimates (e.g., Turtle and Pierazzo, 2001; Tobie et al., 2003; Wakita et al., 2024). We note that conductivities above 10 S/m are possible if the salt content of Europa's ocean is near the solubility limit (Hand & Chyba, 2007), the required salinity however lies above 100 g/kg.

5.2 Results

In this section, we present the results from our chi-squared analysis. First, we provide a short overview of the E14 flyby, followed by a review of the uncertainty estimates for that flyby. Taking into account these uncertainties, we show the observed induction response and all induced magnetic fields that lie within $\chi \leq 1$. Afterward, we investigate the parameter space of ocean properties (d, h, σ) and derive constraints. We take additional geophysical estimates of the ocean's depth and electrical conductivity into account to further limit our initial solution volume. Finally, we test the robustness of our method by slightly varying the model setup and compare the resulting constraints against the reference model.

5.2.1 The E14 Flyby

During the E14 flyby, Galileo approached Europa upstream, flying near its equatorial plane with a closest approach (C/A) altitude of 1684.1 km (Figure 5.6). Europa was situated above the plasma sheet during the encounter, with a magnetic latitude of $\Psi_{\mathrm{m}} = 9.1°$ (Kurth et al., 2001). To assess the flyby for the purposes of our quantitative analysis, we fit the induction response of a perfectly conducting ocean with $A = 1$ and $\phi^{\mathrm{ph}} = 0$ to the measurements (Figure 5.7). The B_x-component is well reproduced by only taking the ocean's induced field into account. While we expect the plasma interaction to contribute noticeably to the B_y-component, the conditions of the E14 flyby are ideal for our quantitative study, despite its large altitude. Thus, in the following, we will focus solely on the E14 flyby.

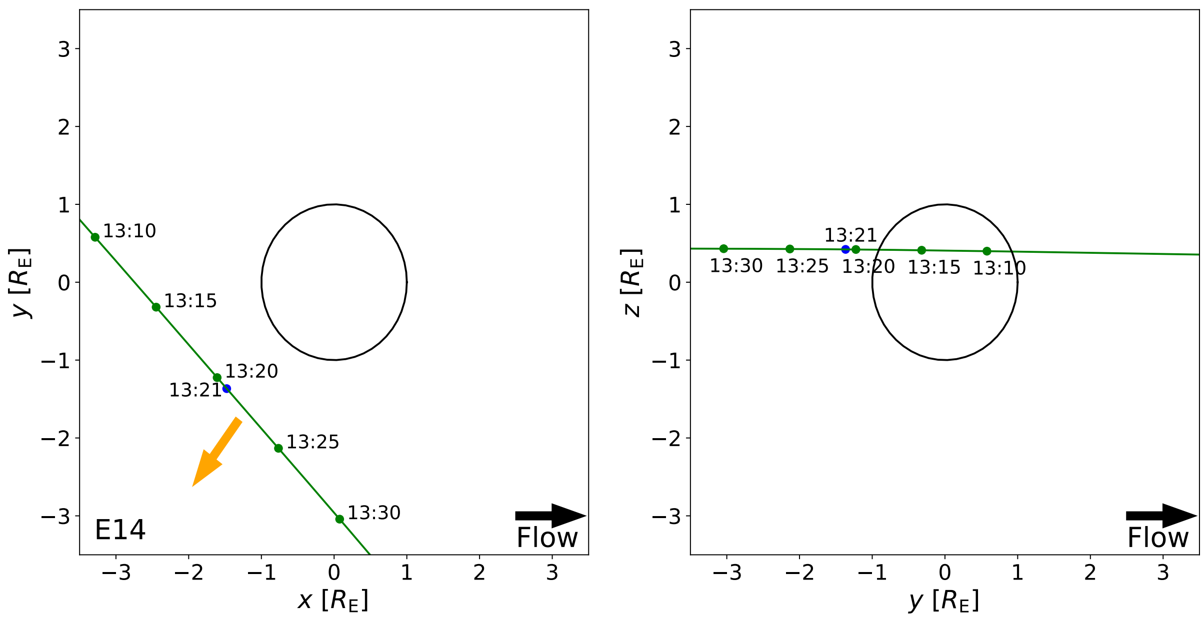

Figure 5.6: Trajectory of the Galileo spacecraft during the E14 encounter in the xy (left) and yz-plane (right), respectively. The blue dot marks the time and location of closest approach. The yellow arrow points toward the sun.

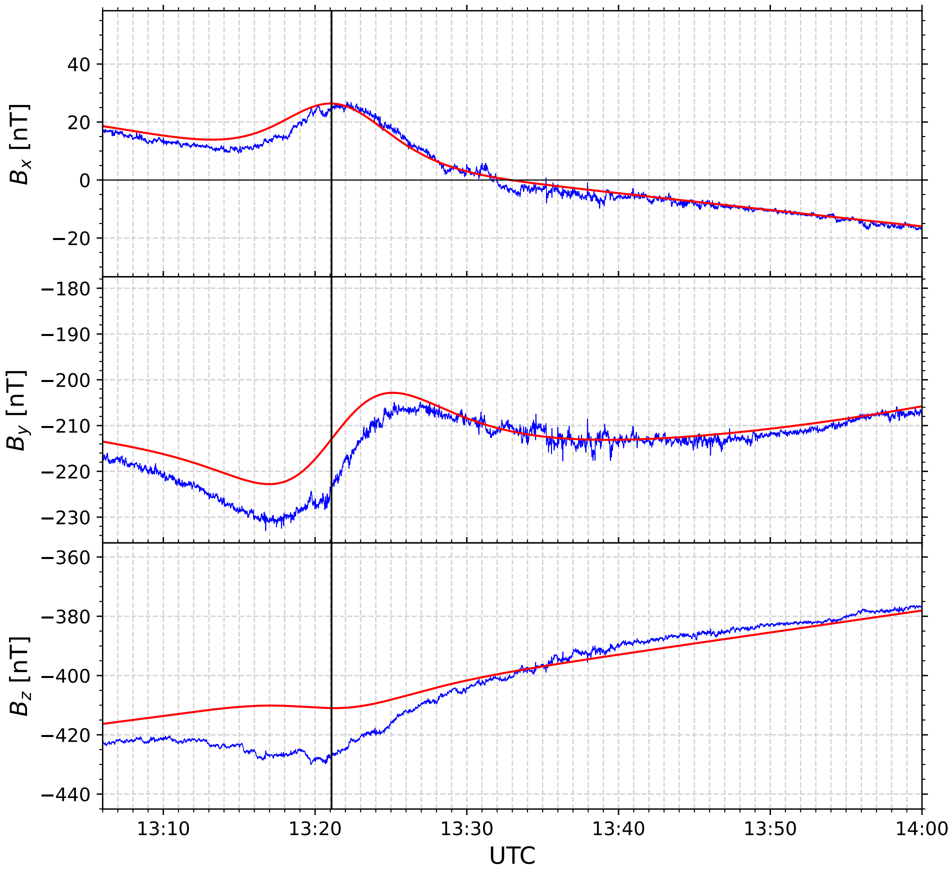

Figure 5.7: Magnetic field measurements of the E14 flyby (blue) and the induction response of a perfectly conducting ocean with $A = 1$ and $\phi^{\mathrm{ph}} = 0$ (red). The vertical black line marks the closest approach.

The same assessment has been done for the flybys E04, E12, E19, and E26. The measurements are presented in Appendix E. For the cases of the E12 and E26 flybys, the induction response is obscured by strong plasma magnetic fields of up to 100 nT, hampering the possibility to quantitatively constrain Europa's subsurface ocean, as our model would be primarily controlled by Europa's plasma interaction, rather than its ocean characteristics. During the E19 flyby, the magnetometer stopped recording shortly after closest approach. This complicates the fitting of the Jovian background field and thus the overall inversion process. The E04 flyby was a wake crossing and had plasma magnetic fields on a similar strength to the induced field. Of the five flybys discussed, the E04 was deemed the second most suitable for the exploration of Europa's ocean. However, we refrain from performing a joint inversion of the E04 and E14 flybys due to stronger high-frequency fluctuations in the E04 measurements. As these are not accounted for in our model, the goodness of our fits would degrade as a result. A joint inversion would be of interest if multiple flybys with conditions similar to the E14 flyby existed, i.e., a low C/A altitude (< 1800 km), large distance to the plasma sheet, magnetic field perturbations dominated by the induced field, and small high-frequency fluctuations throughout the measurements.

5.2.2 Uncertainty Estimates

In Section 5.1, we have stated the equations used to estimate the uncertainties introduced within our individual model descriptions for the induced magnetic field, Jupiter's background field, and the plasma interaction at Europa (see Equations (5.11), (5.12), and (5.22), respectively). We present the values for all three uncertainties in Figure 5.8, as well as the resulting total uncertainty $\sqrt{\sigma_{\mathrm{bg}}^2 + \sigma_{\mathrm{plasma}}^2 + \sigma_{\mathrm{ind}}^2(\mathbf{r}_i)}$. As we only use the B_x and B_y-components to perform our analysis, we only show the uncertainties for these two components. The plasma uncertainty is the dominating contribution to the overall uncertainty, with $\sigma_{\mathrm{plasma}} = 1.72\,\mathrm{nT}$. Furthermore, the plasma uncertainty is the same in both components, as we assume that the uncertainty in the B_z-component translates to B_x and B_y. The uncertainty of the background field is calculated for each component individually and is constant across the entire flyby, with $\sigma_{\mathrm{bg}} = (0.56, 0.59)\,\mathrm{nT}$. While the plasma and background fields uncertainties are calculated once and are assumed to be a constant value throughout the flyby, the uncertainty of the induced field is calculated along the spacecraft's trajectory and is thus approximately zero for most measurements due to the distance term in the induced dipole. Having obtained our uncertainty estimates, we can now perform the chi-squared analysis to derive the ocean properties and their constraints.

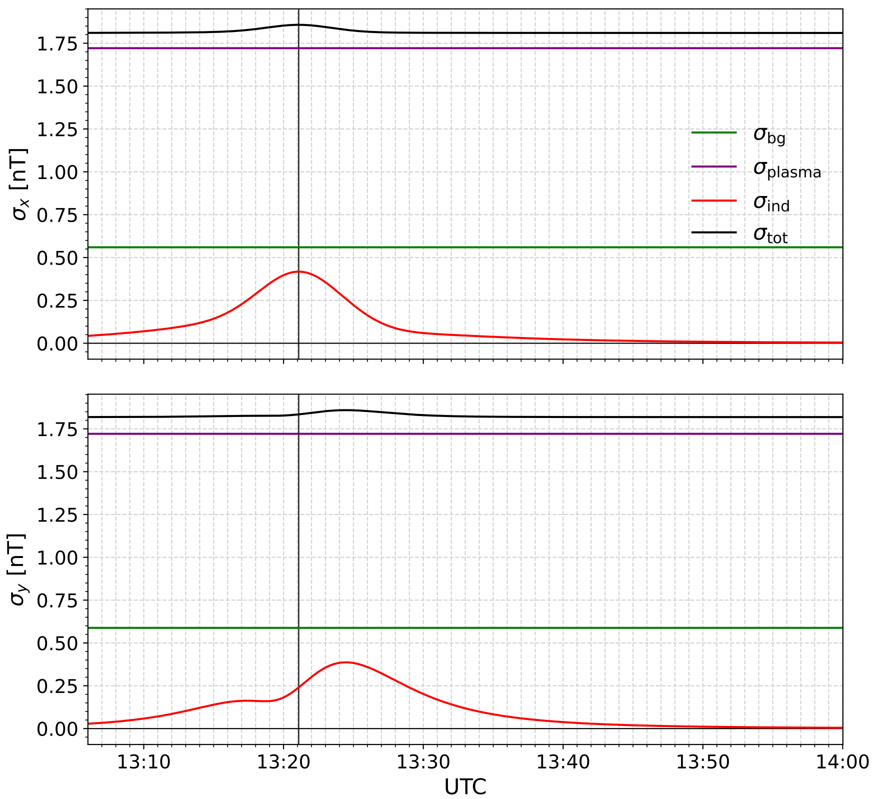

Figure 5.8: Uncertainty estimates during the E14 flyby for the induced field (red, Equation (5.11)), the Jovian background field (green, Equation (5.12)), and the plasma magnetic field (purple, Equation (5.22)). The black line is the total uncertainty of the system, used in the denominator of Equation (5.23).

5.2.3 Chi-Squared Analysis

Figure 5.9 shows the "observed induction response" $\mathbf{B}_{\text{obs,ind}}$ as calculated with Equation (5.2). In addition, all induction models that lie within $\chi < 1$ are presented. We are able to reproduce the trend of the observed induction response in the B_x and B_y-components, although underestimating the amplitude of the perturbation in the B_x-component around closest approach. The best fit to the measurements is a highly conductive, shallow ocean ($d = 1\,\text{km}$, $h = 7\,\text{km}$, $\sigma = 10\,\text{S/m}$), indicated as a red solid line in Figure 5.9. This work, however, does not only provide the best fit for (d, h, σ), but also the possible range for these values derived from the chi-squared analysis. The $\chi \leq 1$ criterion provides a direct method to obtain upper and lower limits for (d, h, σ), above or below which χ^2 would be greater than one, and thus not an appropriate fit. The limits are derived by considering the $\chi = 1$ isocontour.

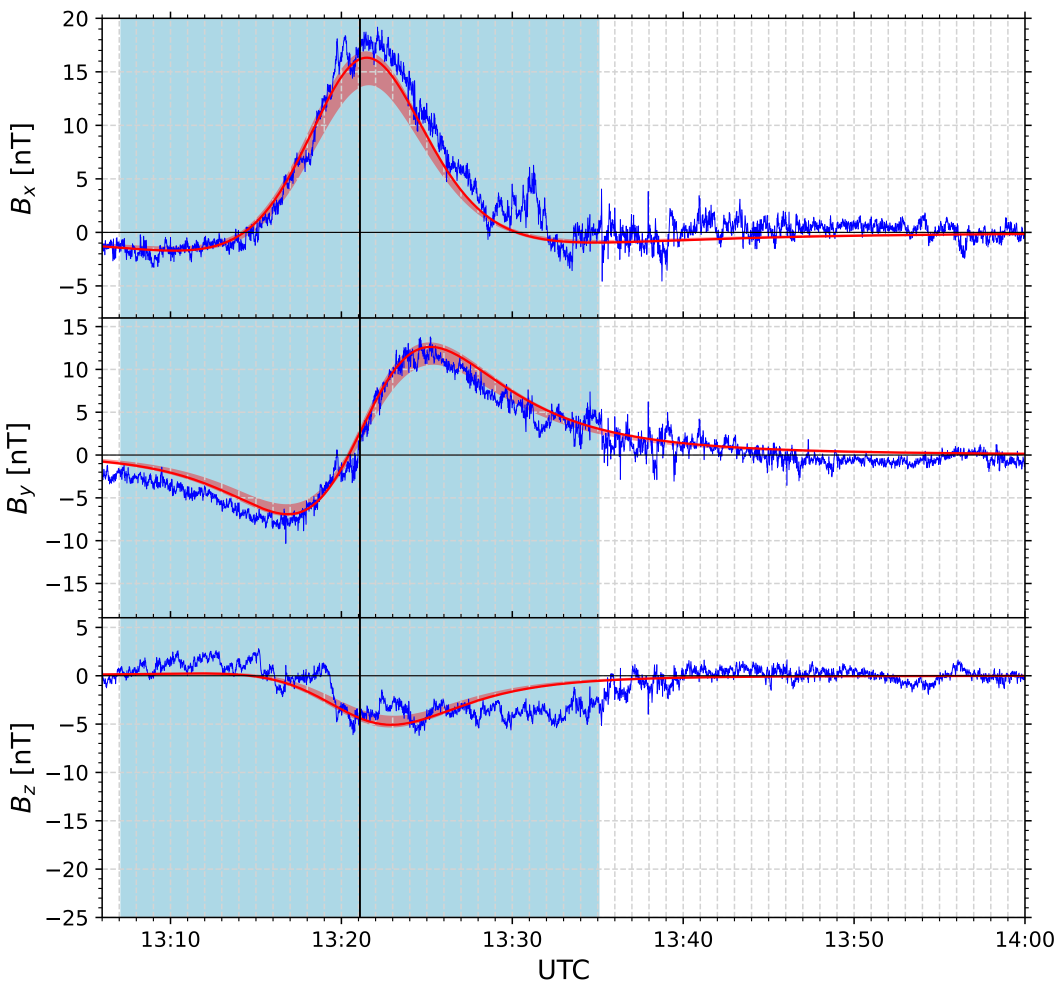

Figure 5.9: Observed induction response $\mathbf{B}_{\text{obs,ind}}$ (blue) for the E14 flyby. The light red band shows all induction models with a $\chi \leq 1$. The red solid line is our best fit with $\chi^2 \approx 0.6$ at $d = 1\,\text{km}$, $h = 7\,\text{km}$, and $\sigma = 10\,\text{S/m}$. The interval of the trajectory where Galileo was within 4 Europa radii relative to Europa's center is highlighted in light blue.

In Figure 5.10, we show the χ-isocontours in conductivity-thickness space for three given depths. The solution for depth $d = 1\,\mathrm{km}$ yields lower constraints on the subsurface ocean's conductivity of $\sigma > 0.3\,\mathrm{S/m}$ and a thickness of $h > 3\,\mathrm{km}$. Within the prescribed parameter space, we are unable to resolve an upper limit on both the conductivity and thickness of Europa's ocean. The existence of an ocean directly at the surface is unlikely. Thus, we investigate the conductivity-thickness space at 20 km depth. This corresponds to the minimum depth suggested by Wakita et al. (2024). As the induction amplitude decreases with increasing depth, the space of possible values for (h, σ) below the $\chi = 1$ isocontour decreases, with a minimum conductivity around $0.45\,\mathrm{S/m}$. The minimum thickness at 20 km depth changed slightly, with $h > 3.5\,\mathrm{km}$. The lowest depth that still lies within $\chi \leq 1$ is approximately 90 km. However, the required conductivity at that depth lies above $8\,\mathrm{S/m}$. This conductivity would require a highly saline ocean above 100 g/kg, considering temperatures around 273 K (Pan et al., 2020, 2021; Vance et al., 2021).

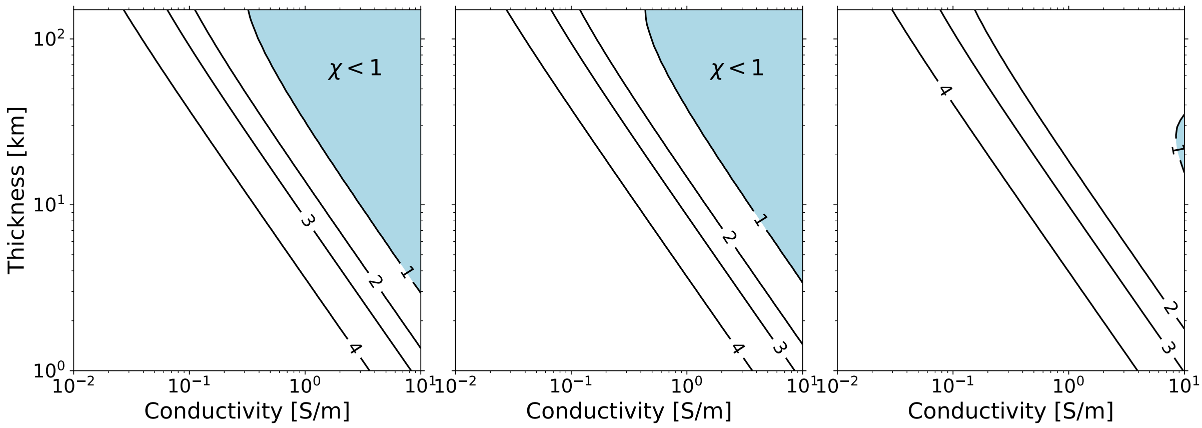

Figure 5.10: χ-isocontours in conductivity-thickness space for (left) $d = 1\,\mathrm{km}$, (middle) $d = 20\,\mathrm{km}$, and (right) $d = 90\,\mathrm{km}$. The blue shaded region marks the $\chi < 1$ solution space.

5.2.4 Robustness of Our Method

The constraints derived in this work are a result of the assumptions in our individual models for the inducing field, the background field, and the magnetic field due to Europa's plasma interaction, as well as the values for the input parameters, e.g., the degree of the background fit and the O_2 column density. In three additional runs, we introduce slight changes to our model parameters to assess the robustness of our derived constraints, only varying one parameter at a time. These model changes do not vary the respective magnetic field contributions significantly and, should this approach be robust, should also result in similar limits on the ocean properties compared to the reference model. The variations to our model that we consider are

i. a background fit of degree $n = 2$,

ii. a background fit with interval length $\Delta t = 20\,\mathrm{min}$,

iii. and an asymmetric O_2 atmosphere that includes both upstream-downstream asymmetry and a day-night asymmetry.

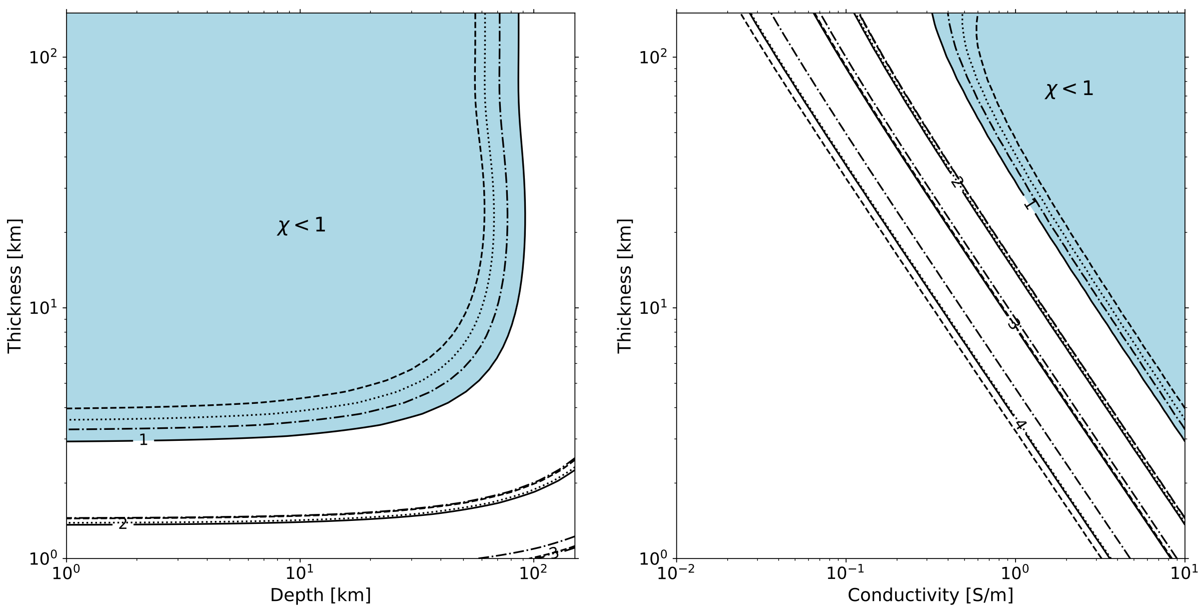

Figure 5.11: χ-isocontours of the reference model presented in Section 5.2.3 (solid), a model with degree $n = 2$ background fit (dash dotted), a model with interval length $\Delta t = 20\,\text{min}$ background fit (dashed), and a model with asymmetric O_2 atmosphere (dotted). The left figure presents the isocontours in depth-thickness space, highlighting variations in the derived depth constraints. The right figure shows the isocontours in conductivity-thickness space to highlight the robustness of our derived conductivity constraints.

In each case, we estimate the resulting uncertainties and calculate χ^2 across the prescribed parameter space. The resulting χ-isocontours for all four runs are shown in Figure 5.11 in depth-thickness and conductivity-thickness space, respectively. The constraints derived from the $\chi = 1$ isocontour are listed in Table 5.2. It should be noted that the listed constraints do not take into account additional limitations on the ocean's depth. In the following subsections, we will compare the resulting background and plasma interaction fields and provide possible explanations for the observed robustness.

Table 5.2: Limits on Europa's subsurface ocean properties derived under varying model assumptions

	d [km]	h [km]	σ [S/m]
Reference model	90	3.0	0.32
$n = 2$ fit	77	3.3	0.40
$\Delta t = 20\,\text{min}$ fit	61	4.0	0.59
Asymmetric atmosphere	85	3.3	0.38

Robustness Against Background Field Variations

Figure 5.12 shows the three background fits used in this study compared to the measured data. The deviation between the 15-minute background fit and 20-minute fit appears the most noticeable since particularly in the B_x-component the 20-minute fit is around 1 nT smaller than our reference fit around closest approach. This in turn will result in an "observed induction response" that is approximately 1 nT larger than in the reference case. As a consequence, the required induction amplitude (and phase) to stay within $\chi < 1$ increases (decreases), resulting in more restrictive constraints on the ocean properties. In contrast, the background fit with degree $n = 3$ is shown to be fairly robust against changes in the degree of the polynomial fit compared to $n = 2$, as all three components follow either fairly linear or parabolic trends within the considered frame of measurements. This notion holds specifically for the considered interval length of $\Delta t = 15$ min, and might not be applicable at longer timeframes, where the polynomials no longer fit to the periodicity of Jupiter's background field. We thus motivate a short interval length for the optimal background fit.

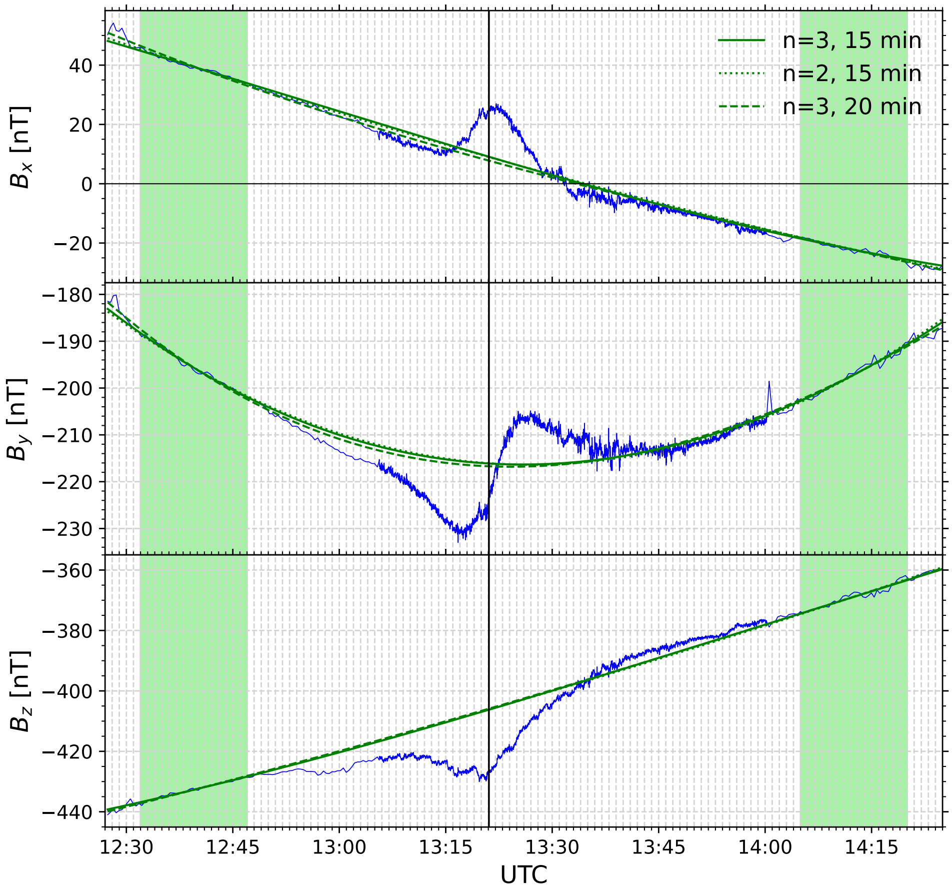

Figure 5.12: Magnetic field measurements (blue) and background fits calculated with (solid green) degree $n = 3$ and window length $\Delta t = 15$ min, (dashed green) $n = 3$ and $\Delta t = 20$ min, and (dotted green) $n = 2$ and $\Delta t = 15$ min. The light green area indicates the respective 15-minute intervals.

Robustness Against Variations in the Atmospheric Model

While a radially symmetric atmosphere was used to obtain the results in Section 5.2.3, simulations by Plainaki et al. (2013) on the generation of Europa's exosphere show a spatial variability due to the time-varying orientations of solar illumination and the incident plasma direction. Additional variabilities between the trailing and leading hemispheres of Europa have been observed (Hansen et al., 2005). In this section, we employ an atmosphere model that includes both an upstream-downstream and day-night asymmetry to test how a varying atmosphere model influences the derived limits of Europa's ocean properties. For that, the surface density is described with a longitudinal variability following

$$n_{\mathrm{O}_2}(\phi) = \begin{cases} n_{0,\mathrm{O}_2}(1 + k\sin\phi)(1 + k'\cos(\phi - \phi_{\mathrm{sp}})) & \text{if } \frac{\pi}{2} < \phi < \frac{3\pi}{2} \wedge |\phi - \phi_{\mathrm{sp}}| < \frac{\pi}{2} \\ n_{0,\mathrm{O}_2}(1 + k\sin\phi) & \text{if } \frac{\pi}{2} < \phi < \frac{3\pi}{2} \wedge |\phi - \phi_{\mathrm{sp}}| > \frac{\pi}{2} \\ n_{0,\mathrm{O}_2}(1 + k'\cos(\phi - \phi_{\mathrm{sp}})) & \text{if } -\frac{\pi}{2} < \phi < \frac{\pi}{2} \wedge |\phi - \phi_{\mathrm{sp}}| < \frac{\pi}{2} \\ n_{0,\mathrm{O}_2} & \text{else,} \end{cases} \tag{5.24}$$

with n_{0,O_2} resulting in a column density of $N_{\mathrm{O}_2} = 10^{14}\,\mathrm{cm}^{-2}$ and ϕ_{sp} being the longitude of the subsolar point. Here, we use $k = 1$ and $k' = 1$ to reproduce the perturbations in the B_z-component from the symmetric model, which results in a maximum column density of $4 \cdot 10^{14}\,\mathrm{cm}^{-2}$, assuming the subsolar point aligns with the trailing hemisphere apex. As the B_z-component does not vary much between both model runs, the uncertainty σ_{plasma} of our MHD model changes by only 7%, with $\sigma_{\mathrm{plasma}} = 1.71\,\mathrm{nT}$ in the reference model and $\sigma_{\mathrm{plasma}} = 1.60\,\mathrm{nT}$ for the asymmetric atmosphere model, using our best fit ocean to calculate σ_{plasma}. Since the uncertainty is slightly smaller in the asymmetric description of Europa's atmosphere, we would expect tighter constraints on the ocean properties, assuming the B_x and B_y-components are unchanged. If the plasma interaction fields from the asymmetric case would be in better agreement with the observations in the B_x and B_y-component, the misfit between $\mathbf{B}_{\mathrm{model}}$ and $\mathbf{B}_{\mathrm{obs}}$ would decrease, thus increasing the combination of ocean properties that fulfill $\chi^2 \leq 1$. From the slightly tighter constraints on the ocean properties in the asymmetric case compared to the reference model, we conclude that this not the case.

The changes in the magnetic field of plasma perturbations, which were introduced by consideration of an asymmetric atmosphere, yield minor changes in our derived constraints for the ocean properties, indicating that our method is robust with changes to our atmospheric model. We emphasize that these findings are specific to the atmosphere model considered in this study, and furthermore a result of the chosen strength of the asymmetry, with $k = 1$ and $k' = 1$. Consideration of other longitudinal variabilities or a stronger/weaker asymmetry will have an effect on the robustness. Thus, our results cannot be extrapolated to such cases.

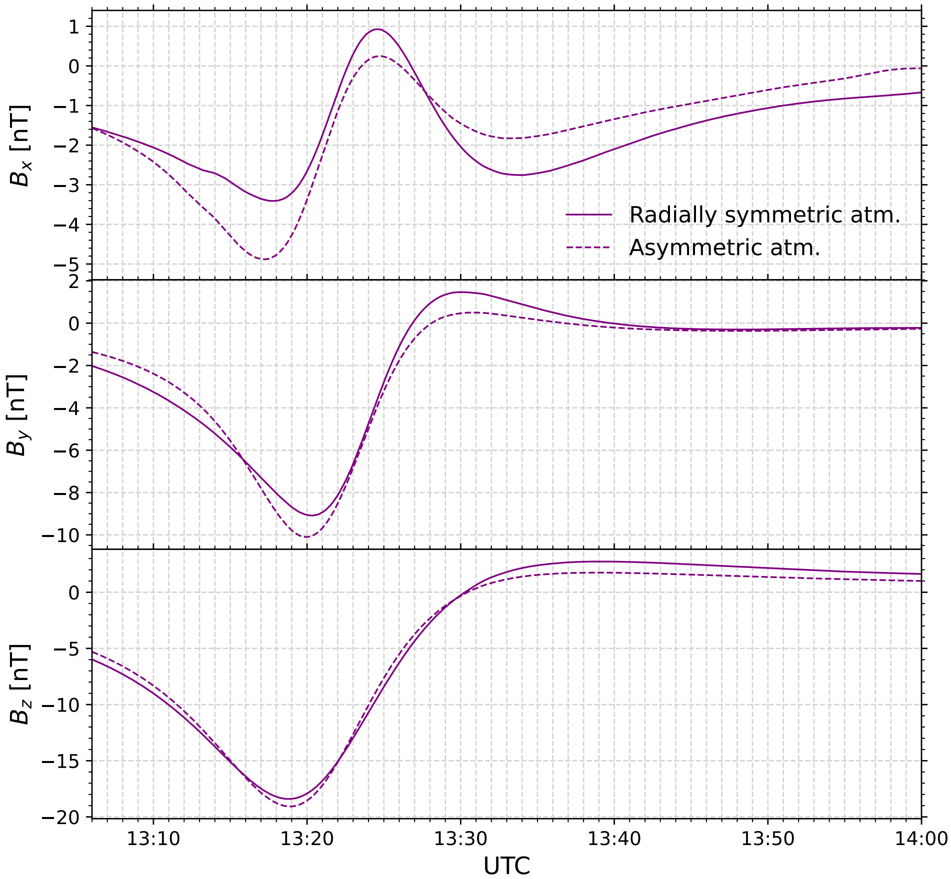

Figure 5.13: Plasma perturbed magnetic field resulting from (solid) a symmetric atmosphere with column density $N_{O_2} = 4{\cdot}10^{14}\,\mathrm{cm}^{-2}$ and (dashed) an asymmetric atmosphere with upstream-downstream and day-night asymmetries, following Equation (5.24).

5.3 Discussion

Here, we summarize the estimated uncertainties and discuss the quantitative constraints on Europa's interior derived with the chi-squared analysis of the E14 flyby. We also present the application of this approach to Galileo's E04 flyby and compare the results against the E14 flyby.

5.3.1 Uncertainty Estimates

In this work, we estimated the uncertainties that are introduced by our models for the inducing field at Europa, the Jovian magnetospheric background field, and the magnetic field due to plasma interaction in Europa's vicinity. These uncertainties are specific to the conditions of a given flyby. The uncertainty of the inducing field, and thus of the induced field, varies with System III longitude, as described by Equation (5.4). We characterized the uncertainty of the inducing field amplitudes $(\sigma_{q0}, \sigma_{s0})$ as the difference of the inducing amplitude of the synodic rotation period obtained from two various models. This approach provides only a rough approximation. Additional uncertainties of the phase of the dipole component of Jupiter's intrinsic field, ϕ_0, were not taken into account.

The uncertainties of the background field and the plasma magnetic field are characterized by the RMS, following Equations (5.12) and (5.22). As such, an increased misfit between our model and the observations will naturally increase these two uncertainties as well. Such increased misfits can occur during flybys where small-scale fluctuations are larger than, for example, during the E14 flyby, as they are not included in our model description of Europa's magnetic field environment (see Section 5.3.3).

We estimate the uncertainty of the plasma model using the B_z-component and assume that this uncertainty translates into the B_x and B_y-components. While this is only an assumption, it provides a first order estimate of the uncertainty introduced by our MHD model and highlights the necessity to consider such uncertainties when analyzing existing and future spacecraft data.

It should be noted that this work does not cover all uncertainties and is confined to single-frequency magnetic sounding. While the consideration of additional frequencies, e.g., higher order synodics and Europa's orbital period, can provide useful additional insights (Biersteker et al., 2023), we consider these outside the scope of this work.

5.3.2 Application to the E14 Flyby

Here, we discuss the results obtained in Section 5.2.3. We first review the constraints on Europa's interior derived from the chi-squared analysis and follow with an evaluation of their robustness against changes to the model setup.

Interior Constraints

The primary motivation of this work is to characterize and constrain the depth, thickness, and electrical conductivity of Europa's subsurface ocean. As most existing constraints originating from electromagnetic induction have been derived qualitatively from visual comparison, this study emphasizes the development of a method using a quantitative measure, in the form of a chi-squared analysis, where the squared deviation between the modelled induction response $\mathbf{B}_{\text{ind}}$ and the observed induction $\mathbf{B}_{\text{obs,ind}}$, described by Equation (5.2), is weighed against the sum of our model uncertainties described by Equations (5.11), (5.12), and (5.22). Due to its ideal conditions for magnetic sounding, i.e., a strong inducing field and quiet plasma environment, we applied this method to the E14 flyby. Here we found a minimum conductivity of approximately 0.45 S/m, assuming the icy crust is at least 20 km thick (Wakita et al., 2024). This value is slightly lower than the constraint obtained by Schilling et al. (2007), who estimated the minimum conductivity to be 0.5 S/m. Zimmer et al. (2000) suggested a minimum conductivity of 0.06 S/m. Compared to the value derived in this study, $\sigma \geq 0.45$ S/m, our method provides a tighter constraint on the conductivity. It is worth noting that the cited constraints were not derived quantitatively, but only qualitatively on the basis of visually comparing various ocean models to the measurements.

While our inversion motivated an ocean that lies at a shallow depth, with $d = 1\,\mathrm{km}$ for the best fit, such small values conflict with geological estimates from tidal heating and crater simulations, where larger icy crust thicknesses in the range of 20-35 km are suggested. Assuming a conductivity of $10\,\mathrm{S/m}$, we derived a depth constraint on Europa's ocean, according to which it lies at most 90 km below the icy surface. This value lies outside the uncertainties on the icy crust thickness derived by Petricca et al. (2023), who suggested a thickness of at most 35 km. In their work, induction amplitudes of $A = 0.97 \pm 0.02$ and $A = 0.92 \pm 0.02$ were considered. The uncertainty of the induction amplitude is taken from Schilling et al. (2004), who, however, did not perform a systematic analysis of their model uncertainties. The cited value thus likely underestimates the range of possible values for the induction amplitude. As a comparison, our lowest value for the induction amplitude is $A = 0.81$. This comparison highlights the varying constraints that can be derived under consideration of different uncertainties and, more importantly, emphasizes the necessity of a systematic error analysis.

Robustness of Our Method

To study the robustness of our method, we considered slight changes in our setup for the background fit, as well as an asymmetric atmosphere in our plasma interaction model. The background field has been modelled by fitting a polynomial to the measurements outside the region, where perturbations caused by the induced field and plasma interaction with Europa's atmosphere are non-negligible. While this method was also used in, e.g., Zimmer et al. (2000) and Schilling et al. (2004), its degree, interval length, and excluded window were not specified. In this work, we found that these specifications have a noticeable impact on our fits to the data and thus on the derived constraints on Europa's interior. Our method appeared least robust against changes to the interval length of the background fit, as here, the resulting background field changed the most. The background fit is involved in multiple instances of our method, i.e., its uncertainty σ_{bg}, the uncertainty of the plasma interaction σ_{plasma}, and the observed induction response. Thus, variations to the background field noticeably influence the derived constraints. Particularly the last point is not exclusive to our work, but pertains to the principle of magnetic sounding in general, and emphasizes the importance of the fit of Jupiter's background field. In this work, we proposed a background fit of 15 minute interval length and degree $n = 3$ to be the optimal fit. This assessment was done on the basis of calculating the RMS within the fitting window. We note, however, that the minimum lies at the lower limit of the considered interval lengths. Thus, a polyfit of 14 minute interval length could have a smaller RMS, and be deemed a better background fit on the basis of RMS alone. While we motivate a fitting window of at least 15 minutes to average out remnant plasma interaction fields and not 'overfit' the data, more work is required to find the 'best' background fit, as well as a criterion to assess the goodness of the fit.

The derived constraints experienced a small change when we used an asymmetric atmosphere instead of a radially symmetric atmosphere. While we interpret this result as a robustness of the ocean properties to variations in our asymmetric model, we prescribed a specific strength of the asymmetry. We cannot extrapolate this conclusion to changes in the overall setup of our MHD model, as we kept additional parameters affecting the plasma interaction (e.g., ionization frequency f_{imp}) unchanged. Therefore, additional tests would be required to study the robustness of the retrieved ocean properties to changes in the various input parameters of the MHD model. In general, the results of any inversion will be specific to the plasma interaction model used in the description of Europa's magnetic field environment.

5.3.3 Application to the E04 Flyby

While this work focussed primarily on the magnetic field measurements of the E14 flyby, we also applied our chi-squared analysis to the E04 flyby at Europa. This flyby occurred at a C/A altitude of 696 km while Europa was outside the Jovian plasma sheet. A noticeable difference to the E14 flyby is that the E04 was a downstream flyby, crossing Europa's wake. Figure 5.14 compares the plasma magnetic field and the induced magnetic field, similar to Figure 5.3 for the E14 flyby. While the induced field is the primary source of magnetic field perturbation in the B_x and B_y-components, plasma magnetic fields are larger for the conditions of the E04 flyby compared to those of the E14 flyby. Here, a column density of $N_{\mathrm{O}_2} = 10^{14}\,\mathrm{cm}^{-2}$ was used to model the plasma interaction. Expectedly, the induced field is stronger compared to the E14 flyby, due to the lower altitude. Using Equation (5.22), we derive a plasma uncertainty of $\sigma_{\mathrm{plasma}} \approx 7.4\,\mathrm{nT}$, approximately five times higher than our estimate for the E14 flyby. To fit the background field, we used a polynomial fit of degree $n = 3$ and window length $\Delta t = 27\,\mathrm{min}$. This deviates from the 15 minutes used in the E14 flyby, as for the E04, the RMS was minimum at 27 minutes. The resulting background fit is shown in Figure 5.15.

Figure 5.16 shows the observed induction response obtained for the E04 flyby. Comparing the observed induction to that of the E14 flyby (Figure 5.9), larger residuals in the B_z component become apparent. These indicate that the plasma interaction model used here is less representative of the 'real' environment than compared to the E14 flyby. In addition, small-scale fluctuations are stronger throughout the encounter compared to those of the E14 flyby. These, seemingly random, high frequency perturbations can be seen throughout the measurements and are possibly a result of kinetic effects (see Blöcker et al., 2016). Another noteworthy feature is the continuous offset in the B_x component while approaching Europa, in the order of 10-20 nT. These strong deviations from our model result in an RMS of approximately 11 nT for our best fit model obtained in the analysis of the E04 flyby. This value is ten times larger than that of the E14 flyby, 1.14 nT. Figure 5.17 shows the residuals $\Delta\mathbf{B} = \mathbf{B}_{\mathrm{obs,ind}} - \mathbf{B}_{\mathrm{ind}}$ in all three components for the E04 and E14 flybys. If our model were to perfectly describe the measurements, the residuals would be zero. Non-zero residuals are visible in both flybys across all components, although for the E04 flyby they are on the order of 10 nT. In comparison, the residuals for the E14 flyby consistently lie below 10 nT throughout the flyby. This direct comparison emphasizes that the observations during the E04 flyby have stronger contributions from effects that are not considered in our model for Europa's magnetic field environment. It is for that reason that a joint inversion was not performed in this work. A smaller pool

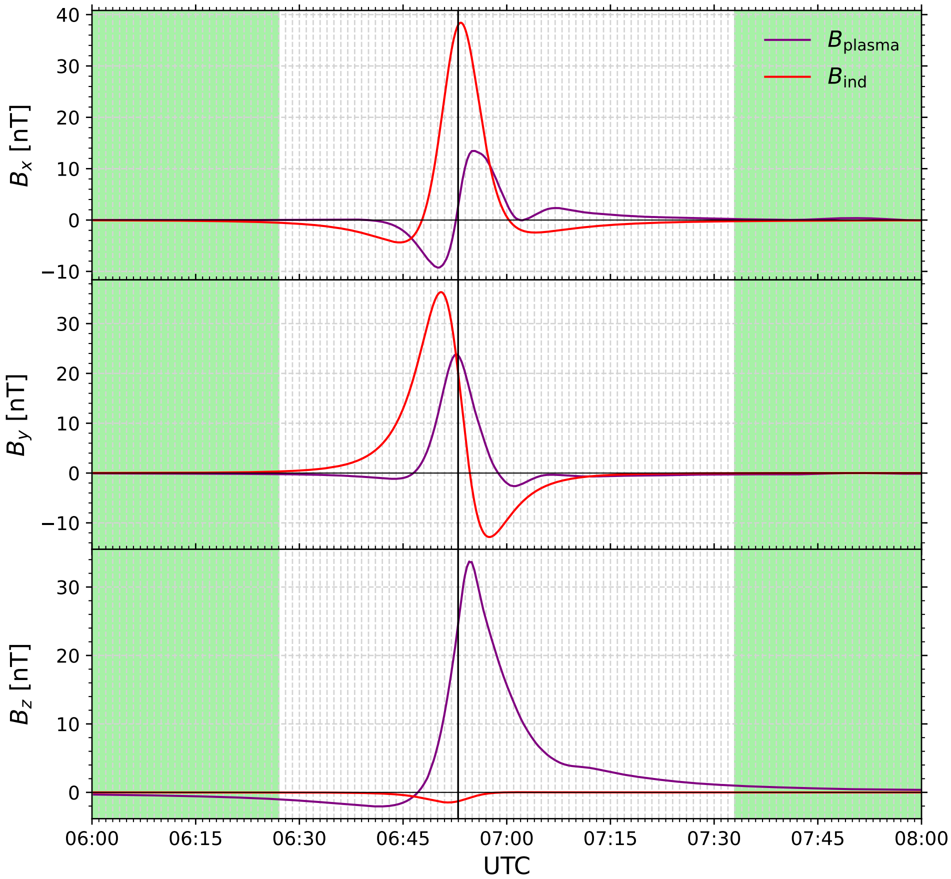

Figure 5.14: Modelled magnetic field due to plasma interaction with Europa's atmosphere (purple) and induction response (red) for the E04 flyby. Moving outward from closest approach (black vertical line), the green regions begin when the magnetic field signatures are smaller than 1.5 nT and cover a range of 27 minutes, respectively.

of measurements that is described well by our model allows for better retrieval of ocean properties than a larger sample size, where our model partially fails to account for the measured magnetic field, resulting in larger residuals.

Our chi-squared analysis for the E04 flyby results in $\chi^2 > 1$ across the entire parameter space, with a minimum of approximately 1.6. Two possible explanations for this result are (i) underestimating our uncertainties and (ii) our description of the Europa's magnetic field environment does not fully capture the measured magnetic field. Particularly, the latter reason plays a role during the E04 flyby, as shown in Figure 5.17. Residuals oscillating around zero indicate that our model describes the general structure of the observations well, with the exception of the small-scale fluctuations, as is the case for the E14 flyby. However, in the E04 flyby, these fluctuations are not only stronger, but there are also noticeable offsets from the zero line on the order of 10 nT, indicating that larger structures of the observations are mismodelled. This could result from an incomplete plasma interaction model. Thus, the E04 flyby is an ideal example to emphasize the need for accurate modelling of the plasma perturbed magnetic fields around Europa to gain quantitative insights about Europa's interior from magnetometer measurements. For that reason, the Europa Clipper spacecraft is equipped with the PIMS (Plasma Instrument for Magnetic Sounding) instrument, monitoring the plasma environment to correct the magnetometer measurements for plasma perturbed fields (Westlake et al., 2023). These corrections should allow for better removal of plasma magnetic fields from observations, which in turn will improve retrieval of ocean properties, but also increase the number of measurements that can be used in the inversion. The multitude of flybys performed by the Europa Clipper spacecraft will generate an unprecedented amount of measurements and fill gaps in System III longitudinal coverage as well, providing a great opportunity to apply this method in a joint inversion of multiple flybys.

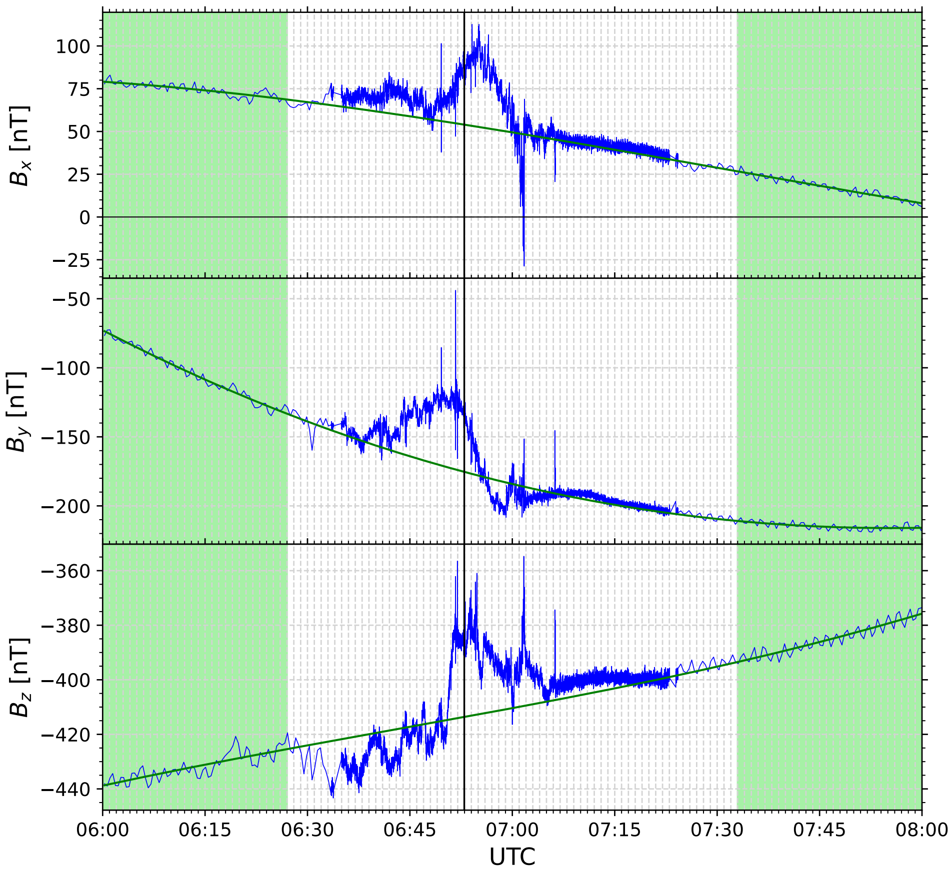

Figure 5.15: Polynomial fit (green) to the components of the measured magnetic field (blue). The light green area indicates the respective 27-minute windows used to calculate the fit.

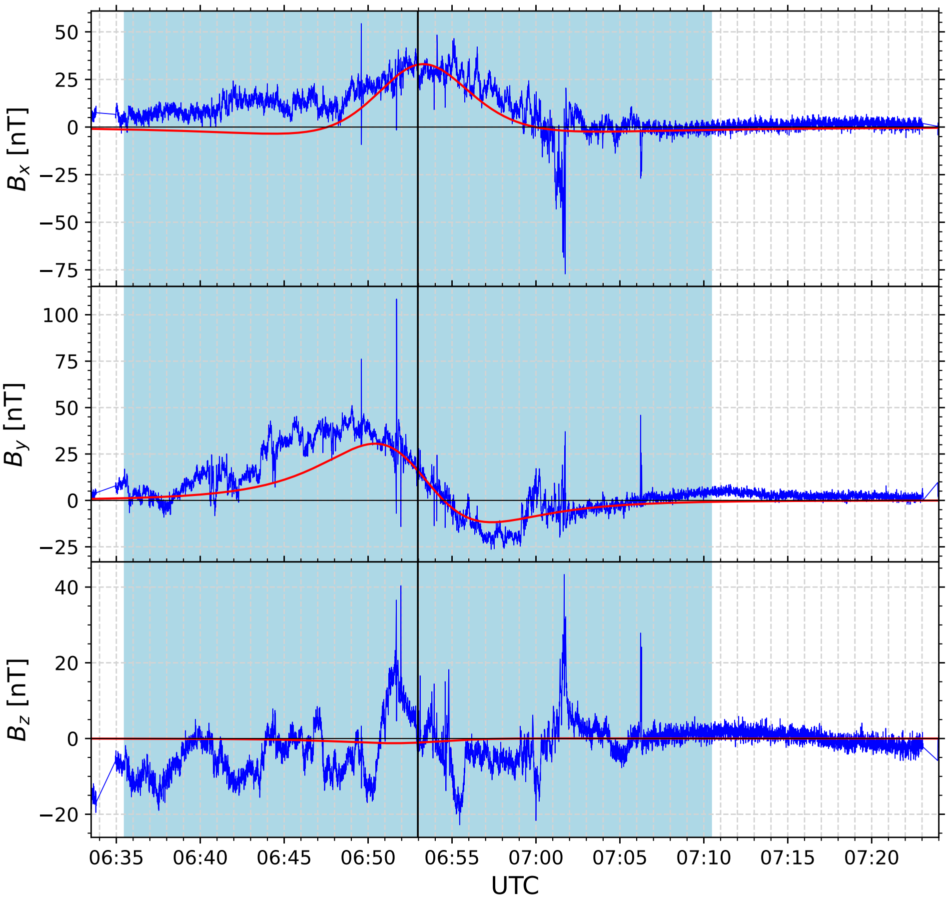

Figure 5.16: Observed induction response $\mathbf{B}_{\mathrm{obs,ind}}$ (blue) for the E04 flyby. The red solid line shows the best fit induced magnetic field obtained from our analysis of the E14 flyby. The blue region highlights the portion of the trajectory where Galileo was within 4 Europa radii relative to the moon's center.

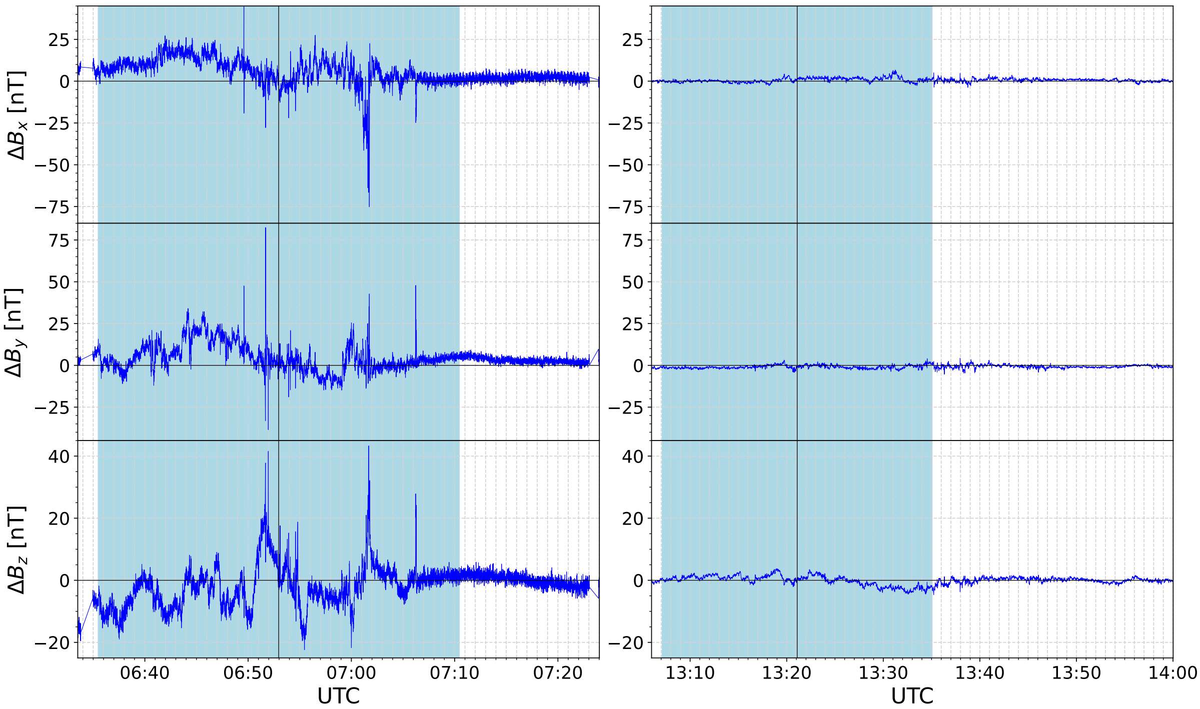

Figure 5.17: Residuals $\Delta \mathbf{B} = \mathbf{B}_{\text{obs,ind}} - \mathbf{B}_{\text{ind}}$ for (left) the E04 flyby and (right) the E14 flyby.

5.4 Conclusion

In this study, we developed a method to quantitatively derive the depth, thickness, and electrical conductivity of Europa's subsurface ocean, as well as constraints on these properties. For that, we performed an inversion where we compared the modelled magnetic field against the observations of the Galileo spacecraft. The magnetic field model in this work is described as the sum of the Jovian background field, the induced magnetic field generated within Europa's subsurface ocean, and the plasma magnetic field, as described by Equation (5.1). Each contribution to the magnetic field was modelled individually and has an uncertainty associated with it, for which we introduced estimates. These estimates were used in a chi-squared analysis to derive the ocean properties, which were used as model parameters in the analysis. Any combination of depth, thickness, and conductivity that resulted in a magnetic field model with $\chi > 1$ was classified as an inappropriate fit to the observations and thus considered outside the regime of possible values for the ocean properties. This way, the $\chi = 1$ isocontour provided constraints on the range of (d, h, σ). The combination of (d, h, σ) where chi-squared is at minimum yields the best fit to the measurements.

We showcased the method using the magnetic field measurements of Galileo's E14 flyby, as the plasma environment was 'quiet' during the encounter and the inducing field was near its maximum, resulting in a strong electromagnetic response. While the observations of four other flybys, E04, E12, E19, and E26, were also discussed as potential candidates for the inversion, we ultimately decided against further consideration of those measurements for varying reasons, as stated in Section 5.2.1.

After performing the chi-squared analysis, we found that the measurements are best reproduced by a subsurface ocean that is preferably shallow and highly conductive. The best fit lies at $d = 1\,\mathrm{km}$, $h = 7\,\mathrm{km}$, and $\sigma = 10\,\mathrm{S/m}$. We took additional estimates of the ocean's depth into account to further constrain the electrical conductivity and thickness. For that, we considered a minimum depth of 20 km (Wakita et al., 2024). Under consideration of the additional depth constraint, we derived a minimum conductivity of 0.45 S/m. An upper limit on the conductivity could not be resolved, as the induction amplitude saturates. For the thickness, no upper constraint was found within our prescribed parameter space, considering thicknesses up to 150 km. However, our analysis yielded a minimum thickness of 3.5 km.

The Jovian background field is commonly approximated by a polynomial fit to the measurements of the specific flyby considered. The degree of the fit, as well as the interval length and its start and end, however, are ambiguous and usually not well documented in the previous literature. In this work, we have shown the effect that varying background fits have on the derived ocean properties, emphasizing the need for adequate documentation of background fitting in future work to ensure reproducibility. Additionally, we suggest the consistent use of one background model across various studies once the observations of both the JUICE and Europa Clipper spacecrafts become available, as this would greatly increase the comparability of the obtained results. While we motivated a background fit with interval length of 15 minutes and degree $n = 3$, we could not with full certainty claim that this is the "best fit". It is worth noting that, measured by the RMS, the optimal interval length varies between flybys, i.e., the RMS is minimal at 27 minutes for the E04 flyby. This further motivates that the RMS might not be the ideal criterion to assess the 'best' background fit, and to instead decide on one specific window length for all flybys.

We also compared the constraints resulting from two different descriptions for Europa's atmosphere, showing minor changes in both the magnetic field due to the plasma interaction, and in the constraints of the ocean properties. While the conditions of the E14 resulted in comparably small plasma magnetic field contributions in the B_x and B_y-components, this does not hold for any arbitrary flyby, as shown in our application to the E04 flyby. The framework we present in this study provides a useful method to analyze existing and future spacecraft data, such as will be recorded with ESA's JUICE spacecraft and NASA's Europa Clipper, and quantify uncertainties introduced by our models for the individual contributions to Europa's magnetic field environment.

6

Conclusion

In this work, we first considered the induction response that would be generated by small pockets of water melt entrapped in Europa's icy crust. Such liquid water reservoirs could exist during the formation of chaos regions. As their exact formation mechanism, however, is unclear, the potential identification of reservoir induction signals in magnetic field measurements could improve our understanding of Europa's interior and the processes that generate surface chaos. The inclusion of a local water reservoir in the model of Europa's interior enables electromagnetic coupling between the global subsurface ocean and the reservoir, as the induced fields also act as inducing fields. To solve this induction coupling, we developed an analytical, iterative approach. With that, the coupled induced fields of both ocean and reservoir can be calculated to a prescribed maximum degree $l_{\max}$ and iteration step $n_{\max}$. We found that the reservoir has a negligible inducing effect on the global ocean. The ocean's induction response to the reservoir was thus excluded from further calculations in this work. On the contrary, the ocean's dipole induced by the time-varying component of Jupiter's magnetic field induces a magnetic field within the reservoir. This contribution is non-negligible and, since the ocean's induction response cannot be assumed to be homogeneous around the reservoir, consists of higher degrees as well. We found that, for our prescribed parameter space of reservoirs with radii up to 25 km and conductivities up to 30 S/m, degrees up to $l = 3$ must be considered in the multipole description to describe the total induction response of the system with a precision of 10^{-2} nT.

We applied this method to a hypothetical 25 km flyby directly above a reservoir and calculated its induction response. Here, we found values for the reservoir induction response below 1 nT across the entire parameter space. Due to additional small-scale fluctuations in the measured magnetic field, such small induction signatures are likely not detectable, as they would be indistinguishable from these fluctuations. Employing a lander and measuring the magnetic field directly at the surface would negate the rapid fall-off of the reservoir's induction response. In this scenario, reservoirs would likely be detectable, even at smaller radii of $r_{\mathrm{res}} = 8\,\mathrm{km}$, assuming a conductivity of $\sigma_{\mathrm{res}} = 30\,\mathrm{S/m}$. For a single stationary magnetometer, the problem is underdetermined. Therefore, two magnetometers on the surface with sufficient distance from each other are necessary to disentangle the induction responses from the ocean and the reservoir.

In the second part of this thesis, we performed an inversion of magnetic field measurements recorded with the Galileo spacecraft, with the goal to explore Europa's subsurface ocean and describe its properties, i.e., its depth, thickness, and electrical conductivity. For that, we first introduced our models for Jupiter's magnetospheric field, the induced field, and the magnetic field due to Europa's plasma interaction. We performed a systematic error analysis, estimating the model uncertainties that are introduced by our individual model descriptions. Through the model uncertainty, we could derive constraints on the ocean properties by employing a chi-squared analysis. As any combination of ocean properties resulting in a $\chi > 1$ is classified as an inappropriate fit to the measurements, the $\chi = 1$ isocontour provides the upper and lower limits on depth, thickness, and electrical conductivity.

In our inversion, we considered only the observations of Galileo's E14 flyby and found that the observations were best explained by a subsurface ocean that is preferably shallow and highly conductive, with a best fit of $d = 1\,\mathrm{km}$, $h = 7\,\mathrm{km}$, and $\sigma = 10\,\mathrm{S/m}$. As such shallow depths are in conflict with other geological estimates, i.e., from tidal heating and crater simulations, we took additional estimates of the ocean's depth into account to further constrain the electrical conductivity and thickness.

The interior of the icy satellite Europa remains an active research question, more than 25 years after the discovery of its subsurface ocean. This year, on October 14th, the Europa Clipper spacecraft successfully launched, embarking on its journey to the Jovian system, where it will enter Jupiter orbit in 2030. During its mission, the spacecraft will perform 49 flybys at Europa, collecting an unprecedented amount of data. Besides the sheer volume of data, Europa Clipper will be closer to the icy satellite than any other spacecraft before, performing multiple flybys in the range of 25 to 100 km altitude. These low altitude encounters enable the exploration of new science objectives. The work carried out in this thesis provides an approach to characterize the coupled induction response between a global ocean and local water reservoir, and estimates the possibility to detect such melt pockets, especially with the Europa Clipper spacecraft but also future lander missions. We furthermore provide a quantitative framework to describe Europa's subsurface ocean and constrain its properties. This method should prove useful in the analysis of future spacecraft data, especially as we provide a systematic error analysis of the model uncertainties in the magnetic field model.

Bibliography

Abramowitz, M., & Stegun, I. A. (1972). *Handbook of mathematical functions with formulas, graphs, and mathematical tables* (10th ed., Vol. 55). US Government printing office.

Addison, P., Haynes, C. M., Stahl, A. M., Liuzzo, L., & Simon, S. (2024). Magnetic signatures of the interaction between Europa and Jupiter's magnetosphere during the Juno flyby. *Geophysical Research Letters*, *51*(2), e2023GL106810.

Allegrini, F., Saur, J., Szalay, J. R., Ebert, R. W., Kurth, W. S., Cervantes, S., Smith, H. T., Bagenal, F., Bolton, S. J., Clark, G., et al. (2024). Electron beams at Europa. *Geophysical research letters*, *51*(13), e2024GL108422.

Anderson, J. D., Schubert, G., Jacobson, R. A., Lau, E. L., Moore, W. B., & Sjogren, W. L. (1998). Europa's differentiated internal structure: Inferences from four Galileo encounters. *Science*, *281*(5385), 2019–2022.

Arnold, H., Liuzzo, L., & Simon, S. (2019). Magnetic signatures of a plume at Europa during the Galileo E26 flyby. *Geophysical Research Letters*, *46*(3), 1149–1157.

Arnold, H., Liuzzo, L., & Simon, S. (2020). Plasma interaction signatures of plumes at Europa. *Journal of Geophysical Research: Space Physics*, *125*(1), e2019JA027346.

Arridge, C. S., & Eggington, J. W. B. (2021). Electromagnetic induction in the icy satellites of Uranus. *Icarus*, *367*, 114562.

Bagenal, F. (1994). Empirical model of the Io plasma torus: Voyager measurements. *Journal of Geophysical Research: Space Physics*, *99*(A6), 11043–11062.

Bagenal, F., & Dols, V. (2020). The space environment of Io and Europa. *Journal of Geophysical Research: Space Physics*, *125*(5), e2019JA027485.

Bevington, P. R., & Robinson, D. K. (2003). *Data reduction and error analysis for the physical sciences*. McGraw-Hill, New York.

Biersteker, J. B., Weiss, B. P., Cochrane, C. J., Harris, C. D. K., Jia, X., Khurana, K. K., Liu, J., Murphy, N., & Raymond, C. A. (2023). Revealing the interior structure of icy moons with a Bayesian approach to magnetic induction measurements. *The Planetary Science Journal*, *4*(4), 62.

Blanc, M., Prieto-Ballesteros, O., André, N., Gómez-Elvira, J., Jones, G., Sterken, V., Desprats, W., Gurvits, L. I., Khurana, K. K., Balmino, G., et al. (2020). Joint Europa Mission (JEM): a multi-scale study of Europa to characterize its habitability and search for extant life. *Planetary and space science*, *193*, 104960.

Blöcker, A., Saur, J., & Roth, L. (2016). Europa's plasma interaction with an inhomogeneous atmosphere: Development of Alfvén winglets within the Alfvén wings. *Journal of Geophysical Research: Space Physics*, *121*(10), 9794–9828.

Bolton, S. J., Bagenal, F., Blanc, M., Cassidy, T., Chané, E., Jackman, C., Jia, X., Kotova, A., Krupp, N., Milillo, A., et al. (2015). Jupiter's magnetosphere: Plasma sources and transport. *Space Science Reviews*, *192*, 209–236.

Brown, M. E., & Hand, K. P. (2013). Salts and radiation products on the surface of Europa. *The Astronomical Journal*, *145*(4), 110.

Campagnola, S., Buffington, B. B., Lam, T., Petropoulos, A. E., & Pellegrini, E. (2019). Tour design techniques for the Europa Clipper mission. *Journal of Guidance, Control, and Dynamics*, *42*(12), 2615–2626.

Cappuccio, P., Di Benedetto, M., Durante, D., & Iess, L. (2022). Callisto and Europa gravity measurements from JUICE 3GM experiment simulation. *The Planetary Science Journal*, *3*(8), 199.

Carlson, R. W., Johnson, R. E., & Anderson, M. S. (1999). Sulfuric acid on Europa and the radiolytic sulfur cycle. *Science*, *286*(5437), 97–99.

Castillo-Rogez, J. C., Daswani, M. M., Glein, C. R., Vance, S. D., & Cochrane, C. J. (2022). Contribution of non-water ices to salinity and electrical conductivity in Ocean Worlds. *Geophysical Research Letters*, *49*(16), e2021GL097256.

Catling, D. C. (2013). *Astrobiology: a very short introduction* (Vol. 370). Oxford University Press, USA.

Cervantes, S., & Saur, J. (2022). Constraining Europa's subsolar atmosphere with a joint analysis of HST spectral images and Galileo magnetic field data. *Journal of Geophysical Research: Space Physics*, *127*(9), e2022JA030472.

Collins, G. C., Patterson, G. W., Detelich, C. E., Prockter, L. M., Kattenhorn, S. A., Cooper, C. M., Rhoden, A. R., Cutler, B. B., Oldrid, S. R., Perkins, R. P., et al. (2022). Episodic Plate Tectonics on Europa: Evidence for Widespread Patches of Mobile-Lid Behavior in the Antijovian Hemisphere. *Journal of Geophysical Research: Planets*, *127*(11), e2022JE007492.

Connerney, J. E. P., Timmins, S., Oliversen, R. J., Espley, J. R., Joergensen, J. L., Kotsiaros, S., Joergensen, P. S., Merayo, J. M. G., Herceg, M., Bloxham, J., et al. (2022). A new model of Jupiter's magnetic field at the completion of Juno's prime mission. *Journal of Geophysical Research: Planets*, *127*(2), e2021JE007055.

Dalton, J. B., Prieto-Ballesteros, O., Kargel, J. S., Jamieson, C. S., Jolivet, J., & Quinn, R. (2005). Spectral comparison of heavily hydrated salts with disrupted terrains on Europa. *Icarus*, *177*(2), 472–490.

Duling, S., Saur, J., Clark, G., Allegrini, F., Greathouse, T., Gladstone, R., Kurth, W. S., Connerney, J. E. P., Bagenal, F., & Sulaiman, A. H. (2022). Ganymede MHD model: Magnetospheric context for Juno's PJ34 flyby. *Geophysical Research Letters*, *49*(24), e2022GL101688.

Duling, S., Saur, J., & Wicht, J. (2014). Consistent boundary conditions at nonconducting surfaces of planetary bodies: Applications in a new Ganymede MHD model. *Journal of Geophysical Research: Space Physics*, *119*(6), 4412–4440.

Greeley, R., Figueredo, P. H., Williams, D. A., Chuang, F. C., Klemaszewski, J. E., Kadel, S. D., Prockter, L. M., Pappalardo, R. T., Head III, J. W., Collins, G. C., et al. (2000). Geologic mapping of Europa. *Journal of Geophysical Research: Planets*, *105*(E9), 22559–22578.

Greeley, R., Sullivan, R., Klemaszewski, J., Homan, K., Head III, J. W., Pappalardo, R. T., Veverka, J., Clark, B. E., Johnson, T. V., Klaasen, K. P., et al. (1998). Europa: initial Galileo geological observations. *Icarus*, *135*(1), 4–24.

Greenberg, R., Hoppa, G. V., Tufts, B. R., Geissler, P., Riley, J., & Kadel, S. (1999). Chaos on Europa. *Icarus*, *141*(2), 263–286.

Guo, H., & Keppler, H. (2019). Electrical conductivity of NaCl-bearing aqueous fluids to 900 C and 5 GPa. *Journal of Geophysical Research: Solid Earth*, *124*(2), 1397–1411.

Hall, D. T., Strobel, D. F., Feldman, P. D., McGrath, M. A., & Weaver, H. A. (1995). Detection of an oxygen atmosphere on Jupiter's moon Europa. *Nature*, *373*(6516), 677–679.

Hand, K. P., & Chyba, C. F. (2007). Empirical constraints on the salinity of the europan ocean and implications for a thin ice shell. *Icarus*, *189*(2), 424–438.

Hand, K. P., Phillips, C. B., Murray, A., Garvin, J. B., Maize, E. H., Gibbs, R. G., Reeves, G., San Martin, A. M., Tan-Wang, G. H., Krajewski, J., et al. (2022). Science goals and mission architecture of the Europa lander mission concept. *The Planetary Science Journal*, *3*(1), 22.

Hansen, C. J., Esposito, L., Stewart, A. I. F., Colwell, J., Hendrix, A., Pryor, W., Shemansky, D., & West, R. (2006). Enceladus' water vapor plume. *Science*, *311*(5766), 1422–1425.

Hansen, C. J., Shemansky, D. E., & Hendrix, A. (2005). Cassini UVIS observations of Europa's oxygen atmosphere and torus. *Icarus*, *176*(2), 305–315.

Huybrighs, H. L. F., Roussos, E., Blöcker, A., Krupp, N., Futaana, Y., Barabash, S., Hadid, L. Z., Holmberg, M. K. G., Lomax, O., & Witasse, O. (2020). An active plume eruption on Europa during Galileo flyby E26 as indicated by energetic proton depletions. *Geophysical Research Letters*, *47*(10), e2020GL087806.

Jia, X., Kivelson, M. G., Khurana, K. K., & Kurth, W. S. (2018). Evidence of a plume on Europa from Galileo magnetic and plasma wave signatures. *Nature Astronomy*, *2*(6), 459–464.

Jia, X., Kivelson, M. G., & Paranicas, C. (2021). Comment on "An Active Plume Eruption on Europa During Galileo Flyby E26 as Indicated by Energetic Proton Depletions" by Huybrighs et al. *Geophysical Research Letters*, *48*(6), e2020GL091550.

Kargel, J. S., Kaye, J. Z., Head III, J. W., Marion, G. M., Sassen, R., Crowley, J. K., Ballesteros, O. P., Grant, S. A., & Hogenboom, D. L. (2000). Europa's crust and ocean: Origin, composition, and the prospects for life. *Icarus*, *148*(1), 226–265.

Khurana, K. K. (1997). Euler potential models of Jupiter's magnetospheric field. *Journal of Geophysical Research: Space Physics*, *102*(A6), 11295–11306.

Khurana, K. K., Kivelson, M. G., Stevenson, D. J., Schubert, G., Russell, C. T., Walker, R. J., & Polanskey, C. (1998). Induced magnetic fields as evidence for subsurface oceans in Europa and Callisto. *Nature*, *395*(6704), 777–780.

Khurana, K. K., Kivelson, M. G., Russell, C. T., Walker, R. J., & Southwood, D. J. (1997). Absence of an internal magnetic field at Callisto. *Nature*, *387*(6630), 262–264.

Kivelson, M. G., Khurana, K. K., Joy, S., Russell, C. T., Southwood, D. J., Walker, R. J., & Polanskey, C. (1997). Europa's magnetic signature: Report from Galileo's pass on 19 December 1996. *Science*, *276*(5316), 1239–1241.

Kivelson, M. G., Khurana, K. K., Russell, C. T., Volwerk, M., Walker, R. J., & Zimmer, C. (2000). Galileo magnetometer measurements: A stronger case for a subsurface ocean at Europa. *Science*, *289*(5483), 1340–1343.

Kivelson, M. G., Khurana, K. K., Russell, C. T., Walker, R. J., Joy, S. P., & Mafi, J. N. (2024a). NASA Planetary Data System. https://doi.org/10.17189/nyak-9259

Kivelson, M. G., Khurana, K. K., Russell, C. T., Walker, R. J., Joy, S. P., & Mafi, J. N. (2024b). NASA Planetary Data System. https://doi.org/10.17189/fq45-wv97

Kivelson, M. G., Khurana, K. K., Russell, C. T., Walker, R. J., Warnecke, J., Coroniti, F. V., Polanskey, C., Southwood, D. J., & Schubert, G. (1996a). Discovery of Ganymede's magnetic field by the Galileo spacecraft. *Nature*, *384*(6609), 537–541.

Kivelson, M. G., Khurana, K. K., Stevenson, D. J., Bennett, L., Joy, S., Russell, C. T., Walker, R. J., Zimmer, C., & Polanskey, C. (1999). Europa and Callisto: Induced or intrinsic fields in a periodically varying plasma environment. *Journal of Geophysical Research: Space Physics*, *104*(A3), 4609–4625.

Kivelson, M. G., Khurana, K. K., Walker, R. J., Russell, C. T., Linker, J. A., Southwood, D. J., & Polanskey, C. (1996b). A magnetic signature at Io: Initial report from the Galileo magnetometer. *Science*, *273*(5273), 337–340.

Kivelson, M. G., Jia, X., Lee, K. A., Raymond, C. A., Khurana, K. K., Perley, M. O., Biersteker, J. B., Blacksberg, J., Caron, R., Cochrane, C. J., et al. (2023). The Europa clipper magnetometer. *Space Science Reviews*, *219*(6), 48.

Kurth, W. S., Gurnett, D. A., Persoon, A. M., Roux, A., Bolton, S. J., & Alexander, C. J. (2001). The plasma wave environment of Europa. *Planetary and Space Science*, *49*(3-4), 345–363.

Langel, R. A., & Estes, R. H. (1982). A geomagnetic field spectrum. *Geophysical Research Letters*, *9*(4), 250–253.

Lee, S., Pappalardo, R. T., & Makris, N. C. (2005). Mechanics of tidally driven fractures in Europa's ice shell. *Icarus*, *177*(2), 367–379.

Leonard, E. J., Pappalardo, R. T., & Yin, A. (2018). Analysis of very-high-resolution Galileo images and implications for resurfacing mechanisms on Europa. *Icarus*, *312*, 100–120.

Leonard, E. J., Patthoff, D. A., & Senske, D. A. (2024). *Global geologic map of Europa* (tech. rep.). US Geological Survey.

Lesage, E., Massol, H., & Schmidt, F. (2020). Cryomagma ascent on Europa. *Icarus*, *335*, 113369.

Ligier, N., Poulet, F., Carter, J., Brunetto, R., & Gourgeot, F. (2016). VLT/SINFONI observations of Europa: New insights into the surface composition. *The Astronomical Journal*, *151*(6), 163.

McCleskey, R. B., Nordstrom, D. K., & Ryan, J. N. (2012). Comparison of electrical conductivity calculation methods for natural waters. *Limnology and Oceanography: Methods*, *10*(11), 952–967.

McCord, T. B., Hansen, G. B., Fanale, F. P., Carlson, R. W., Matson, D. L., Johnson, T. V., Smythe, W. D., Crowley, J. K., Martin, P. D., Ocampo, A., et al. (1998). Salts on Europa's surface detected by Galileo's near infrared mapping spectrometer. *Science*, *280*(5367), 1242–1245.

McKinnon, W. B., & Zolensky, M. E. (2003). Sulfate content of Europa's ocean and shell: Evolutionary considerations and some geological and astrobiological implications. *Astrobiology*, *3*(4), 879–897.

Mignone, A., Bodo, G., Massaglia, S., Matsakos, T., Tesileanu, O., Zanni, C., & Ferrari, A. (2007). PLUTO: a numerical code for computational astrophysics. *The Astrophysical Journal Supplement Series*, *170*(1), 228.

Neubauer, F. M. (1998). The sub-Alfvénic interaction of the Galilean satellites with the Jovian magnetosphere. *Journal of Geophysical Research: Planets*, *103*(E9), 19843–19866.

Nimmo, F., Thomas, P. C., Pappalardo, R. T., & Moore, W. B. (2007). The global shape of Europa: Constraints on lateral shell thickness variations. *Icarus*, *191*(1), 183–192.

Pan, Y., Yong, W., & Secco, R. A. (2020). Electrical conductivity of aqueous magnesium sulfate at high pressure and low temperature with application to Ganymede's subsurface ocean. *Geophysical Research Letters*, *47*(21), e2020GL090192.

Pan, Y., Yong, W., & Secco, R. A. (2021). Electrical conductivity of aqueous NaCl at high pressure and low temperature: Application to deep subsurface oceans of icy moons. *Geophysical Research Letters*, *48*(17), e2021GL094020.

Pappalardo, R. T., Buratti, B. J., Korth, H., Senske, D. A., Blaney, D. L., Blankenship, D. D., Burch, J. L., Christensen, P. R., Kempf, S., Kivelson, M. G., et al. (2024). Science Overview of the Europa Clipper Mission. *Space Science Reviews*, *220*(4), 1–58.

Pappalardo, R. T., Vance, S. D., Bagenal, F., Bills, B. G., Blaney, D. L., Blankenship, D. D., Brinckerhoff, W. B., Connerney, J. E. P., Hand, K. P., Hoehler, T. M., et al. (2013). Science potential from a Europa lander. *Astrobiology*, *13*(8), 740–773.

Parkinson, W. D. (1983). Introduction to geomagnetism.

Petricca, F., Genova, A., Castillo-Rogez, J. C., Styczinski, M. J., Cochrane, C. J., & Vance, S. D. (2023). Characterization of icy moon hydrospheres through joint inversion of gravity and magnetic field measurements. *Geophysical Research Letters*, *50*(17), e2023GL104016.

Plainaki, C., Milillo, A., Mura, A., Saur, J., Orsini, S., & Massetti, S. (2013). Exospheric O2 densities at Europa during different orbital phases. *Planetary and Space Science*, *88*, 42–52.

Poston, M. J., Carlson, R. W., & Hand, K. P. (2017). Spectral behavior of irradiated sodium chloride crystals under Europa-like conditions. *Journal of Geophysical Research: Planets*, *122*(12), 2644–2654.

Prockter, L. M., Pappalardo, & T, R. (2000). Folds on Europa: Implications for crustal cycling and accommodation of extension. *Science*, *289*(5481), 941–943.

Roth, L. (2021). A stable H2O atmosphere on Europa's trailing hemisphere from HST images. *Geophysical Research Letters*, *48*(20), e2021GL094289.

Roth, L., Saur, J., Retherford, K. D., Strobel, D. F., Feldman, P. D., McGrath, M. A., & Nimmo, F. (2014). Transient water vapor at Europa's south pole. *science*, *343*(6167), 171–174.

Saur, J., Neubauer, F. M., Connerney, J. E. P., Zarka, P., & Kivelson, M. G. (2004). Plasma interaction of Io with its plasma torus. *Jupiter: The planet, satellites and magnetosphere*, *1*, 537–560.

Saur, J., Neubauer, F. M., & Glassmeier, K.-H. (2009). Induced magnetic fields in solar system bodies. In *Planetary magnetism* (pp. 391–421). Springer.

Saur, J., Strobel, D. F., & Neubauer, F. M. (1998). Interaction of the Jovian magnetosphere with Europa: Constraints on the neutral atmosphere. *Journal of Geophysical Research: Planets*, *103*(E9), 19947–19962.

Schenk, P. M. (2002). Thickness constraints on the icy shells of the Galilean satellites from a comparison of crater shapes. *Nature*, *417*(6887), 419–421.

Schilling, N., Khurana, K. K., & Kivelson, M. G. (2004). Limits on an intrinsic dipole moment in Europa. *Journal of Geophysical Research: Planets*, *109*(E5).

Schilling, N., Neubauer, F. M., & Saur, J. (2007). Time-varying interaction of Europa with the jovian magnetosphere: Constraints on the conductivity of Europa's subsurface ocean. *Icarus*, *192*(1), 41–55.

Schilling, N., Neubauer, F. M., & Saur, J. (2008). Influence of the internally induced magnetic field on the plasma interaction of Europa. *Journal of Geophysical Research: Space Physics*, *113*(A3).

Schmidt, B. E., Blankenship, D. D., Patterson, G. W., & Schenk, P. M. (2011). Active formation of 'chaos terrain' over shallow subsurface water on Europa. *Nature*, *479*(7374), 502–505.

Seufert, M., Saur, J., & Neubauer, F. M. (2011). Multi-frequency electromagnetic sounding of the Galilean moons. *Icarus*, *214*(2), 477–494.

Silber, E. A., & Johnson, B. C. (2017). Impact crater morphology and the structure of Europa's ice shell. *Journal of Geophysical Research: Planets*, *122*(12), 2685–2701.

Smith, B. A., Soderblom, L. A., Beebe, R., Boyce, J., Briggs, G., Carr, M., Collins, S. A., Cook, A. F., Danielson, G. E., Davies, M. E., et al. (1979). The Galilean satellites and Jupiter: Voyager 2 imaging science results. *Science*, *206*(4421), 927–950.

Smyth, W. H., & Marconi, M. L. (2006). Europa's atmosphere, gas tori, and magnetospheric implications. *Icarus*, *181*(2), 510–526.

Sparks, W. B., Hand, K. P., McGrath, M. A., Bergeron, E., Cracraft, M., & Deustua, S. E. (2016). Probing for evidence of plumes on Europa with HST/STIS. *The Astrophysical Journal*, *829*(2), 121.

Sparks, W. B., Schmidt, B. E., McGrath, M. A., Hand, K. P., Spencer, J. R., Cracraft, M., & Deustua, S. E. (2017). Active cryovolcanism on Europa? *The Astrophysical Journal Letters*, *839*(2), L18.

Styczinski, M. J., Vance, S. D., Harnett, E. M., & Cochrane, C. J. (2022). A perturbation method for evaluating the magnetic field induced from an arbitrary, asymmetric ocean world analytically. *Icarus*, *376*, 114840.

Tobie, G., Choblet, G., & Sotin, C. (2003). Tidally heated convection: Constraints on Europa's ice shell thickness. *Journal of Geophysical Research: Planets*, *108*(E11).

Trumbo, S. K., Becker, T. M., Brown, M. E., Denman, W. T. P., Molyneux, P., Hendrix, A., Retherford, K. D., Roth, L., & Alday, J. (2022). A new UV spectral feature on Europa: Confirmation of NaCl in leading-hemisphere chaos terrain. *The Planetary Science Journal*, *3*(2), 27.

Trumbo, S. K., & Brown, M. E. (2023). The distribution of CO2 on Europa indicates an internal source of carbon. *Science*, *381*(6664), 1308–1311.

Trumbo, S. K., Brown, M. E., & Hand, K. P. (2019). Sodium chloride on the surface of Europa. *Science advances*, *5*(6), eaaw7123.

Turtle, E. P., & Pierazzo, E. (2001). Thickness of a Europan ice shell from impact crater simulations. *Science*, *294*(5545), 1326–1328.

Vance, S. D., Styczinski, M. J., Bills, B. G., Cochrane, C. J., Soderlund, K. M., Gómez-Pérez, N., & Paty, C. (2021). Magnetic induction responses of Jupiter's ocean moons including effects from adiabatic convection. *Journal of Geophysical Research: Planets*, *126*(2), e2020JE006418.

Villanueva, G. L., Hammel, H. B., Milam, S. N., Faggi, S., Kofman, V., Roth, L., Hand, K. P., Paganini, L., Stansberry, J., Spencer, J., et al. (2023). Endogenous CO2 ice mixture on the surface of Europa and no detection of plume activity. *Science*, *381*(6664), 1305–1308.

Wakita, S., Johnson, B. C., Silber, E. A., & Singer, K. N. (2024). Multiring basin formation constrains Europa's ice shell thickness. *Science Advances*, *10*(12), eadj8455.

Walker, M. E., & Rhoden, A. R. (2022). Tidal heating at Europa using the multifrequency analysis of tidal heating toolkit. *The Planetary Science Journal*, *3*(7), 149.

Westlake, J. H., McNutt Jr, R. L., Grey, M., Coren, D., Rymer, A. M., Cochrane, C. J., Luspay-Kuti, A., Hohlfeld, E., Seese, N., Crew, A., et al. (2023). The Plasma Instrument for Magnetic Sounding (PIMS) on the Europa Clipper Mission. *Space Science Reviews*, *219*(8), 62.

Winch, D. E., Ivers, D. J., Turner, J. P. R., & Stening, R. J. (2005). Geomagnetism and Schmidt quasi-normalization. *Geophysical Journal International*, *160*(2), 487–504.

Winkenstern, J., & Saur, J. (2023). Detectability of local water reservoirs in Europa's surface layer under consideration of coupled induction. *Journal of Geophysical Research: Planets*, *128*(10), e2023JE007992.

Winkenstern, J. (2023). *Mutual Induction Coupling (in the Case of Europa's Global Subsurface Ocean and a Local Reservoir of Liquid Water)* (Version 2.0). Zenodo [Software]. https://doi.org/10.5281/zenodo.11242047

Zimmer, C., Khurana, K. K., & Kivelson, M. G. (2000). Subsurface oceans on Europa and Callisto: Constraints from Galileo magnetometer observations. *Icarus*, *147*(2), 329–347.

Appendix

A Laplace Equation

In a medium with no electrical conductivity, the magnetic field can be described by a gradient potential Φ with $\mathbf{B} = -\nabla\Phi$. As there are no magnetic monopoles, $\nabla \cdot \mathbf{B} = 0$, the magnetic field potential Φ fulfills the Laplace equation

$$\nabla \cdot (\nabla\Phi) = \triangle\Phi = 0, \tag{A.1}$$

for which the solution will be derived in this appendix. In spherical coordinates, (r, θ, ϕ), the Laplace equation reads

$$\frac{1}{r^2}\partial_r\left(r^2\partial_r\Phi\right) + \frac{1}{r^2\sin\theta}\partial_\theta\left(\sin\theta\partial_\theta\Phi\right) + \frac{1}{r^2\sin^2\theta}\partial_\phi^2\Phi = 0. \tag{A.2}$$

We rewrite the potential using a product ansatz, $\Phi(r, \theta, \phi) = R(r)Y(\theta, \phi)$, which separates radial and angular variabilities. These variables are separated in Equation (A.2) to obtain the following expression after dividing by RY/r^2

$$\frac{1}{R}\frac{\mathrm{d}}{\mathrm{d}r}\left(r^2\frac{\mathrm{d}}{\mathrm{d}r}R\right) = -\left(\frac{1}{Y\sin\theta}\partial_\theta(\sin\theta\partial_\theta Y) + \frac{1}{Y\sin^2\theta}\partial_\phi^2 Y\right). \tag{A.3}$$

The LHS is solely a function of r, while the RHS is a function of (θ, ϕ). As the equation must hold for any combination of (r, θ, ϕ), both sides must equal the same constant, i.e., for the LHS we get

$$\frac{1}{R}\frac{\mathrm{d}}{\mathrm{d}r}\left(r^2\frac{\mathrm{d}}{\mathrm{d}r}R\right) = l(l+1). \tag{A.4}$$

This equation is solved for $R(r) = Ar^l + B^{-l-1}$, where A and B are constants.

The RHS of Equation (A.3) reads

$$\frac{1}{Y\sin\theta}\left(\partial_\theta(\sin\theta\partial_\theta Y) + \frac{1}{\sin\theta}\partial_\phi^2 Y\right) = -l(l+1). \tag{A.5}$$

Using the product ansatz $Y(\theta,\phi)=\Theta(\theta)\varphi(\phi)$ and multiplying with $\sin^2\theta$ yields

$$\frac{\sin\theta}{\Theta}\frac{\mathrm{d}}{\mathrm{d}\theta}\left(\sin\theta\frac{\mathrm{d}\Theta}{\mathrm{d}\theta}\right)+\sin^2\theta l(l+1)=-\frac{1}{\varphi}\frac{\mathrm{d}^2\varphi}{\mathrm{d}\phi^2}. \tag{A.6}$$

Again, both sides depend on separate variables and thus must be equal to a constant, which is here set to m^2. For φ follows

$$\frac{\mathrm{d}^2\varphi}{\mathrm{d}\phi^2}=-m^2\varphi, \tag{A.7}$$

which is solved for $\varphi(\phi)=Ce^{im\phi}$, with constant C.

Multiplying Equation (A.6) with $\Theta/\sin^2\theta$ yields the associated Legendre differential equation

$$\frac{\mathrm{d}^2\Theta}{\mathrm{d}\theta^2}+\frac{\cos\theta}{\sin\theta}\frac{\mathrm{d}\Theta}{\mathrm{d}\theta}+\left(l(l+1)-\frac{m^2}{\sin^2\theta}\right)\Theta=0, \tag{A.8}$$

which is solved for the associated Legendre polynomials

$$P_l^m(\cos\theta)=N_l^m\sin^m\theta\frac{\mathrm{d}^m}{\mathrm{d}\left(\cos\theta\right)^m}P_l(\cos\theta), \tag{A.9}$$

where P_l are the Legendre polynomials and N_l^m is a normalization constant. In geomagnetism, the associated Legendre polynomials are commonly Schmidt quasi-normalized (Winch et al., 2005), i.e., the normalization constant is set to

$$N_l^m=\sqrt{(2-\delta_0^m)\frac{(l-m)!}{(l+m)!}}. \tag{A.10}$$

Finally, the general solution to the Laplace equation can be written as

$$\Phi(r,\theta,\phi)=\sum_{l=0}^{\infty}\sum_{m=-l}^{l}\left(A_lr^l+B_lr^{-l-1}\right)Y_l^m(\theta,\phi), \tag{A.11}$$

with spherical harmonics $Y_l^m(\theta,\phi)=P_l^m(\cos\theta)e^{im\phi}$ of degree l and order m. In the context of magnetic fields, the sum over the degree starts at $l=1$, as there are no magnetic monopoles. Furthermore, the sum over m is usually written from 0 to l, especially in the context of using real Gauss coefficients (q_l^m,s_l^m) and (g_l^m,h_l^m).

B Helmholtz Equation

Inside a conductive layer, $\nabla\times\mathbf{B}\neq 0$, the potential description for the magnetic field does not hold anymore. Here, the induction equation must be solved

$$\triangle\mathbf{B}=\sigma\mu_0\partial_t\mathbf{B}, \tag{B.12}$$

which, in frequency space with $\mathbf{B}(\mathbf{r},t)=\mathbf{B}(\mathbf{r})e^{-i\omega t}$, can be rewritten as

$$\triangle\mathbf{B}=-k^2\mathbf{B}. \tag{B.13}$$

This is the Helmholtz equation with complex wave number $k^2 = i\omega\sigma\mu_0$. Before the Helmholtz equation is solved, the description of the magnetic field is considered first. Since $\nabla\cdot\mathbf{B}=0$ holds, the magnetic field can be fully described by a vector potential $\mathbf{A}$ with $\mathbf{B}=\nabla\times\mathbf{A}$. This vector field can be split into contributions perpendicular and parallel to $\mathbf{r}$, so that

$$\mathbf{A}=T\mathbf{r}+\nabla\times(P\mathbf{r}), \tag{B.14}$$

where T and P are the toroidal and poloidal potentials, respectively. For the magnetic field follows

$$\mathbf{B}=\nabla\times\mathbf{A}=\nabla\times(T\mathbf{r})+\nabla\times[\nabla\times(P\mathbf{r})]. \tag{B.15}$$

Since the curl of a vector is perpendicular to that vector, and $\mathbf{r}=r\hat{e}_r$, that means that the toroidal part of the magnetic field has no radial component. Specifically, toroidal contributions to the magnetic field cannot be observed outside the conductor, i.e., they would not be measured by a spacecraft flying by a planetary body. As such, we will only consider the poloidal parts, which can be described by (Parkinson, 1983)

$$P=\sum_{l=1}^{\infty}\sum_{m=0}^{l}C_l F_l(r)Y_l^m(\theta,\phi). \tag{B.16}$$

In the following, we will consider only a single degree l and order m. After applying the curl twice, the magnetic field $\mathbf{B}=\nabla\times[\nabla\times(P\mathbf{r})]$ reads

$$\begin{aligned}
B_r &= -\frac{1}{r\sin\theta}\left(\partial_\theta(\sin\theta\partial_\theta P))+\frac{1}{\sin\theta}\partial_\phi^2 P\right)\\
B_\theta &= \frac{1}{r}\partial_r(\partial_\theta(Pr))\\
B_\phi &= \frac{1}{r\sin\theta}\partial_r(\partial_\phi(Pr))
\end{aligned} \tag{B.17}$$

The B_r component is recognized as the RHS of Equation (A.3) after multiplying with P/r, and can thus be rewritten as $B_r = P/rl(l+1)$. Plugging Equation (B.16) into our description for the magnetic field yields

$$\begin{aligned}
B_r(r,\theta,\phi) &= \frac{C}{r}F(r)l(l+1)Y_l^m(\theta,\phi)\\
B_\theta(r,\theta,\phi) &= \frac{C}{r}\frac{\mathrm{d}}{\mathrm{d}r}(rF(r))\partial_\theta Y_l^m(\theta,\phi)\\
B_\phi(r,\theta,\phi) &= \frac{C}{r\sin\theta}\frac{\mathrm{d}}{\mathrm{d}r}(rF(r))\partial_\phi Y_l^m(\theta,\phi).
\end{aligned} \tag{B.18}$$

As we are only solving for a scalar function $F(r)$, it is sufficient to solve the Helmholtz equation for one component, e.g., the B_r component

$$(\triangle\mathbf{B})_r=\triangle B_r-\frac{2B_r}{r^2}-\frac{2}{r^2\sin\theta}\partial_\theta(\sin\theta B_\theta)-\frac{2}{r^2\sin\theta}\partial_\phi B_\phi=-k^2B_r \tag{B.19}$$

We first consider the term including the B_θ-component, which can be written as

$$-\frac{2}{r^2\sin\theta}\partial_\theta\left(\sin\theta\partial_\theta\left(\frac{C}{r}\frac{\mathrm{d}}{\mathrm{d}r}(rF)Y_l^m\right)\right) = \frac{2}{r^3}l(l+1)C\frac{\mathrm{d}}{\mathrm{d}r}(rF)Y_l^m + \frac{2}{r^3\sin^2\theta}\frac{\mathrm{d}}{\mathrm{d}r}(rF)\partial_\phi^2 Y_l^m. \tag{B.20}$$

The second term can be rewritten as B_ϕ, so that

$$\frac{2C}{r^3}l(l+1)FY_l^m + \frac{2C}{r^2}\frac{\mathrm{d}F}{\mathrm{d}r}l(l+1)Y_l^m + \frac{2}{r^2\sin\theta}\partial_\phi B_\phi = \frac{2B_r}{r^2} + \frac{2C}{r^2}\frac{\mathrm{d}F}{\mathrm{d}r}l(l+1)Y_l^m + \frac{2}{r^2\sin\theta}\partial_\phi B_\phi. \tag{B.21}$$

It becomes clear that the first and last term cancel with two terms in Equation (B.19). We write $\triangle B_r$ as

$$\frac{1}{r^2}\partial_r(r^2\partial_r B_r)+\frac{1}{r^2\sin\theta}\partial_\theta(\sin\theta\partial_\theta B_r)+\frac{1}{r^2\sin\theta^2}\partial_\phi^2 B_r = \frac{1}{r^2}\partial_r(r^2\partial_r B_r)-\frac{l(l+1)}{r^2}B_r, \tag{B.22}$$

reducing Equation (B.19) to

$$\frac{C}{r}\frac{\mathrm{d}^2F}{\mathrm{d}r^2}l(l+1)Y_l^m - \frac{C}{r^2}Fl^2(l+1)^2Y_l^m + \frac{2C}{r^2}\frac{\mathrm{d}F}{\mathrm{d}r}l(l+1)Y_l^m = -\frac{k^2C}{r}Fl(l+1)Y_l^m. \tag{B.23}$$

Multiplication with r and rewriting yields the spherical Bessel differential equation

$$\frac{\mathrm{d}^2F}{\mathrm{d}r^2} + \frac{2}{r}\frac{\mathrm{d}F}{\mathrm{d}r} + \left(k^2 - \frac{l(l+1)}{r^2}\right)F = 0, \tag{B.24}$$

which is solved for the spherical Bessel functions $j_l(rk)$ and $j_{-l}(rk)$.

C Solving Boundary Conditions

This appendix provides the necessary steps to solve the system of equations obtained from the boundary conditions introduced in Section 3.1.4. The resulting equation system depends on the shape of the conducting body. In this work, a homogeneous sphere and a spherical shell surrounded by two insulating regions (three-layer model) were used. Thus, the boundary equations are solved specifically for these cases.

C.1 Homogeneous Sphere

In the case of a homogeneous sphere, our domain is divided into two subdomains, (I) the surrounding insulator with $\sigma = 0$ and (II) the conducting sphere with $\sigma = \text{const}$. Inside the conducting region, Equation (3.15) is used to describe the magnetic field components, where D must be zero, or else the solution diverges for $r \to 0$. Equation (3.17) results from the required continuity of the normal and tangential component of the magnetic field at the boundary, from which follows for a sphere with radius a and wave number k

$$\begin{aligned} -(lB_\mathrm{e} - (l+1)B_\mathrm{i}) &= \frac{C}{a} l(l+1) j_l(ak) \\ -(B_\mathrm{e} + B_\mathrm{i}) &= \frac{C}{a} F_+(a), \end{aligned} \tag{C.25}$$

where we define a help function $F_+(a)$ as

$$F_+(a) = \frac{\mathrm{d}}{\mathrm{d}r}(r j_l(rk))\Big|_{r=a}. \tag{C.26}$$

From the first equation an expression for C in terms of B_i and B_e can be obtained

$$C = -\frac{r_\mathrm{res}(lB_\mathrm{e} - (l+1)B_\mathrm{i})}{l(l+1)j_l(ak)}, \tag{C.27}$$

which can then be used in the second equation

$$-(B_\mathrm{e} + B_\mathrm{i}) = -\frac{lB_\mathrm{e} - (l+1)B_\mathrm{i}}{l(l+1)j_l(ak)} F_+(a). \tag{C.28}$$

The complex magnetic field coefficients are split up to each side of the equation as

$$B_\mathrm{i}\left(1 + \frac{1}{l j_l(ak)} F_+(a)\right) = -B_\mathrm{e}\left(1 - \frac{1}{(l+1) j_l(ak)} F_+(a)\right), \tag{C.29}$$

from which a preliminary expression for their ratio is obtained

$$\begin{aligned} \frac{B_\mathrm{i}}{B_\mathrm{e}} &= -\frac{1 - \frac{1}{(l+1)j_l(ak)} F_+(a)}{1 + \frac{1}{l j_l(ak)} F_+(a)} \\ &= -\frac{\frac{1}{(l+1)j_l(ak)}\left((l+1)j_l(ak) - F_+(a)\right)}{\frac{1}{l j_l(ak)}\left(l j_l(ak) + F_+(a)\right)} \\ &= -\frac{l}{l+1}\frac{(l+1)j_l(ak) - F_+(a)}{l j_l(ak) + F_+(a)}. \end{aligned} \tag{C.30}$$

In the next step, $F_+(a) = \frac{\mathrm{d}}{\mathrm{d}r}(r j_l(rk))\Big|_{r=a}$ must be calculated, with

$$j_l(rk) = \sqrt{\frac{\pi}{2rk}} J_{l+1/2}(rk). \tag{C.31}$$

Note that the factor $\sqrt{\pi/2}$ will be omitted throughout this appendix, as it cancels out at the end of our derivation. To solve the differential, we apply the product and chain rules

$$\frac{\mathrm{d}}{\mathrm{d}r}(r j_l(rk)) = \frac{\mathrm{d}}{\mathrm{d}r}\left(\sqrt{\frac{r}{k}} J_{l+1/2}(rk)\right) = \frac{\mathrm{d}}{\mathrm{d}r}\left(\sqrt{\frac{r}{k}}\right) + \sqrt{\frac{r}{k}}\frac{\mathrm{d}}{\mathrm{d}rk} J_{l+1/2}(rk)\frac{\mathrm{d}}{\mathrm{d}r}(rk). \tag{C.32}$$

For the differential of the Bessel function, the following identity is used (Parkinson, 1983)

$$\frac{\mathrm{d}}{\mathrm{d}z} J_l(z) = J_{l-1}(z) - \frac{l}{z} J_l(z), \tag{C.33}$$

with which Equation (C.32) can be rewritten as

$$\begin{aligned} \frac{\mathrm{d}}{\mathrm{d}r}(r j_l(rk)) &= \frac{1}{2}\sqrt{\frac{1}{rk}} J_{l+1/2}(rk) + \sqrt{rk}\left(J_{l-1/2}(rk) - \frac{l+1/2}{rk} J_{l+1/2}(rk)\right) \\ &= \sqrt{rk} J_{l-1/2}(rk) - l\sqrt{\frac{1}{rk}} J_{l+1/2}(rk). \end{aligned} \tag{C.34}$$

Plugging Equation (C.34) with $r = a$ into Equation (C.30) yields

$$\begin{aligned} \frac{B_\mathrm{i}}{B_\mathrm{e}} &= -\frac{l}{l+1} \frac{(l+1)\sqrt{\frac{1}{ak}} J_{l+1/2}(ak) - \sqrt{ak} J_{l-1/2}(ak) + l\sqrt{\frac{1}{ak}} J_{l+1/2}(ak)}{l\sqrt{\frac{1}{ak}} J_{l+1/2}(ak) + \sqrt{ak} J_{l-1/2}(ak) - l\sqrt{\frac{1}{ak}} J_{l+1/2}(ak)} \\ &= -\frac{l}{l+1} \frac{\sqrt{ak}\left(\frac{2l+1}{ak} J_{l+1/2}(ak) - J_{l-1/2}(ak)\right)}{\sqrt{ak} J_{l-1/2}(ak)}. \end{aligned} \tag{C.35}$$

Using the recursive identity of the Bessel functions (Parkinson, 1983)

$$J_{l+1}(z) = \frac{2l}{z} J_l(z) - J_{l-1}(z), \tag{C.36}$$

we obtain the ratio between the induced and inducing field coefficients as given in Equation (3.19)

$$\frac{B_\mathrm{i}}{B_\mathrm{e}} = -\frac{l}{l+1} \frac{J_{l+3/2}(ak)}{J_{l-1/2}(ak)}. \tag{C.37}$$

C.2 Three-Layer Model

The three-layer model is constructed by (I) an insulating surrounding region, (II) a conductive layer, and (III) an insulating inner region. Here, we have two boundaries at the inner radius of the conductive layer r_1 and the outer radius r_0, respectively, resulting in a system of four equations

$$\begin{aligned} -lB_\mathrm{e}^{(\mathrm{III})} &= \frac{l(l+1)}{r_1}\left(C j_l(r_1 k) + D j_{-l}(r_1 k)\right) \\ -B_\mathrm{e}^{(\mathrm{III})} &= \frac{1}{r_1}\left(C F_+(r_1) + D F_-(r_1)\right) \\ -(lB_\mathrm{e}^{(\mathrm{I})} - (l+1)B_\mathrm{i}^{(\mathrm{I})}) &= \frac{l(l+1)}{r_0}\left(C j_l(r_0 k) + D j_{-l}(r_0 k)\right) \\ -(B_\mathrm{e}^{(\mathrm{I})} + B_\mathrm{i}^{(\mathrm{I})}) &= \frac{1}{r_0}\left(C F_+(r_0) + D F_-(r_0)\right), \end{aligned} \tag{C.38}$$

where $F_-(a)$ is defined analogously to $F_+(a)$ as

$$F_-(a) = \frac{\mathrm{d}}{\mathrm{d}r}\left(r j_{-l}(rk)\right)\Big|_{r=a}. \tag{C.39}$$

In subdomain (III), $B_{\mathrm{i}}^{(\mathrm{III})}$ must be zero, as else the magnetic field approaches infinity for $r \to 0$. Unlike in the case of the homogeneous sphere, D is now non-zero due to the inner boundary. The RHS of the first equations can be set equal to obtain a relationship between C and D, independent of $B_{\mathrm{e}}^{(\mathrm{III})}$

$$(l+1)(Cj_l r_1 k + Dj_{-l}(r_1 k)) = (CF_+(r_1) + DF_-(r_1)), \tag{C.40}$$

which can be rewritten as

$$D\left((l+1)j_{-l}(r_1 k) - F_-(r_1)\right) = C\left(F_+(r_1) - (l+1)j_l(r_1 k)\right), \tag{C.41}$$

from which an expression for D can be obtained

$$D = \frac{F_+(r_1) - (l+1)j_l(r_1 k)}{(l+1)j_{-l}(r_1 k) - F_-(r_1)} C \tag{C.42}$$

The differential of $rj_l(rk)$ has been calculated in the previous derivation. The expression cannot be used analogously for j_{-l}, instead follows

$$\begin{aligned} \frac{\mathrm{d}}{\mathrm{d}r}(rj_{-l}(rk)) &= \frac{1}{2}\sqrt{\frac{1}{rk}} J_{-l-1/2}(rk) + \sqrt{rk}\left(J_{-l-3/2}(rk) - \frac{-l-1/2}{rk} J_{-l-1/2}(rk)\right) \\ &= (l+1)\sqrt{\frac{1}{rk}} J_{-l-1/2}(rk) + \sqrt{rk} J_{-l-3/2}(rk), \end{aligned} \tag{C.43}$$

where we used Equation (C.33) for the derivative of the Bessel function. From that follows for D

$$\begin{aligned} D &= \frac{\sqrt{r_1 k} J_{-l-1/2}(r_1 k) - l\sqrt{\frac{1}{r_1 k}} J_{l+1/2} - (l+1)\sqrt{\frac{1}{r_1 k}} J_{l+1/2}(r_1 k)}{(l+1)\sqrt{\frac{1}{r_1 k}} J_{-l-1/2}(r_1 k) - (l+1)\sqrt{\frac{1}{r_1 k}} J_{-l-1/2}(r_1 k) - \sqrt{r_1 k} J_{-l-3/2}(r_1 k)} C \\ &= \frac{(2l+1)J_{l+1/2}(r_1 k) - r_1 k J_{l-1/2}(r_1 k)}{r_1 k J_{-l-3/2}(r_1 k)} C. \end{aligned} \tag{C.44}$$

To improve readability throughout the rest of the derivation, we set

$$\xi = \frac{(2l+1)J_{l+1/2}(r_1 k) - r_1 k J_{l-1/2}(r_1 k)}{r_1 k J_{-l-3/2}(r_1 k)}, \tag{C.45}$$

with which follows $D = \xi C$. We use the derived expression for D in the third equation of our system (Equation (C.38)), where the superscript (I) is omitted for B_{e} and B_{i} as $B_{\mathrm{e}}^{(\mathrm{III})}$ does not occur anymore

$$-(lB_{\mathrm{e}} - (l+1)B_{\mathrm{i}}) = \frac{l(l+1)}{r_0} C(j_l(r_0 k) + \xi j_{-l}(r_0 k)). \tag{C.46}$$

As before, we derive an expression for C as

$$C = -\frac{r_0}{l(l+1)} \frac{lB_{\mathrm{e}} - (l+1)B_{\mathrm{i}}}{j_l(r_0 k) + \xi j_{-l}(r_0 k)}, \tag{C.47}$$

which is used in the fourth equation, writing

$$B_\mathrm{e}+B_\mathrm{i}=\frac{1}{l(l+1)}\frac{lB_\mathrm{e}-(l+1)B_\mathrm{i}}{j_l(r_0k)+\xi j_{-l}(r_0k)}\left(F_+(r_0)+\xi F_-(r_0)\right). \tag{C.48}$$

Separating the coefficients B_e and B_i yields

$$\begin{aligned} B_\mathrm{i}&\left(1+\frac{1}{l}\frac{F_+(r_0)+\xi F_-(r_0)}{j_l(r_0k)+\xi j_{-l}(r_0k)}\right)\\ &=-B_\mathrm{e}\left(1-\frac{1}{l+1}\frac{F_+(r_0)+\xi F_-(r_0)}{j_l(r_0k)+\xi j_{-l}(r_0k)}\right), \end{aligned} \tag{C.49}$$

from which the ratio follows as

$$\begin{aligned} \frac{B_\mathrm{i}}{B_\mathrm{e}}&=-\frac{1-\frac{1}{l+1}\frac{F_+(r_0)+\xi F_-(r_0)}{j_l(r_0k)+\xi j_{-l}(r_0k)}}{1+\frac{1}{l}\frac{F_+(r_0)+\xi F_-(r_0)}{j_l(r_0k)+\xi j_{-l}(r_0k)}}\\ &=\frac{\frac{1}{l+1}\frac{1}{j_l(r_0k)+\xi j_{-l}(r_0k)}\left((l+1)(j_l(r_0k)+\xi j_{-l}(r_0k))-F_+(r_0)-\xi F_-(r_0)\right)}{\frac{1}{l}\frac{1}{j_l(r_0k)+\xi j_{-l}(r_0k)}\left(l(j_l(r_0k)+\xi j_{-l}(r_0k))+F_+(r_0)+\xi F_-(r_0)\right)}\\ &=-\frac{l}{l+1}\frac{(l+1)(j_l(r_0k)+\xi j_{-l}(r_0k))-F_+(r_0)-\xi F_-(r_0)}{l(j_l(r_0k)+\xi j_{-l}(r_0k))+F_+(r_0)+\xi F_-(r_0)}. \end{aligned} \tag{C.50}$$

Calculating the differentials, the numerator reads

$$\begin{aligned} &\xi(l+1)\sqrt{\frac{1}{r_0k}}J_{-l-1/2}(r_0)+(l+1)\sqrt{\frac{1}{r_0k}}J_{l+1/2}(r_0k)-\sqrt{r_0k}J_{l-1/2}(r_0k)\\ &+l\sqrt{\frac{1}{r_0k}}J_{l+1/2}(r_0k)-\xi\sqrt{r_0k}J_{-l-3/2}(r_0k)-\xi(l+1)\sqrt{\frac{1}{r_0k}}J_{-l-1/2}(r_0)\\ &=(2l+1)\sqrt{\frac{1}{r_0k}}J_{l+1/2}(r_0k)-\sqrt{r_0k}J_{l-1/2}(r_0k)-\xi\sqrt{r_0k}J_{-l-3/2}(r_0k)\\ &=\sqrt{r_0k}\left(\frac{2l+1}{r_0k}J_{l+1/2}(r_0k)-J_{l-1/2}(r_0k)-\xi J_{-l-3/2}(r_0k)\right)\\ &=\sqrt{r_0k}\left(J_{l+3/2}(r_0k)-\xi J_{-l-3/2}(r_0k)\right), \end{aligned} \tag{C.51}$$

where we used the recursive formula for the Bessel functions. For the denominator, we get

$$\begin{aligned} &l\xi\sqrt{\frac{1}{r_0k}}J_{-l-1/2}(r_0k)+l\sqrt{\frac{1}{r_0k}}J_{l+1/2}(r_0k)+\sqrt{r_0k}J_{l-1/2}(r_0k)\\ &-l\sqrt{\frac{1}{r_0k}}J_{l+1/2}(r_0k)+\xi\sqrt{r_0k}J_{-l-3/2}(r_0k)+\xi(l+1)\sqrt{\frac{1}{r_0k}}J_{-l-1/2}(r_0k)\\ &=\sqrt{r_0k}\left[\xi\left(\frac{2l+1}{r_0k}J_{-l-1/2}(r_0k)+J_{-l-3/2}(r_0k)\right)+J_{l-1/2}(r_0k)\right]\\ &=\sqrt{r_0k}\left(J_{l-1/2}(r_0k)-\xi J_{-l+1/2}(r_0k)\right). \end{aligned} \tag{C.52}$$

Here, special attention must be paid to the application of the recursive formula, as it is applied with an opposite sign, but as the degree $-l-1/2$ is negative, the term $-(-2l-1) = 2l+1$ remains positive. Plugging the results from Equations (C.51) and (C.52) into Equation (C.50) gives our final expression for the ratio

$$\frac{B_\mathrm{i}}{B_\mathrm{e}} = -\frac{l}{l+1}\frac{J_{l+3/2}(r_0k) - \xi J_{-l-3/2}(r_0k)}{J_{l-1/2}(r_0k) - \xi J_{-l+1/2}(r_0k)}, \tag{C.53}$$

from which we obtain Equation (3.21) by rewriting $\xi \to 1/\xi$, as it is used in literature (see, e.g., Zimmer et al., 2000; Saur et al., 2009)

$$\frac{B_\mathrm{i}}{B_\mathrm{e}} = -\frac{l}{l+1}\frac{\xi J_{l+3/2}(r_0k) - J_{-l-3/2}(r_0k)}{\xi J_{l-1/2}(r_0k) - J_{-l+1/2}(r_0k)}, \tag{C.54}$$

with ξ now defined as

$$\xi = \frac{r_1 k J_{-l-3/2}(r_1k)}{(2l+1)J_{l+1/2}(r_1k) - r_1 k J_{l-1/2}(r_1k)}. \tag{C.55}$$

D Coordinate Transformation

As mentioned in Section 3.2, two coordinate systems must be employed to solve the coupling feedback between two conducting bodies to ensure spherical symmetry within each system. This appendix covers the coordinate transformation that is performed between the two systems shown in Figure D.1, and has also been published as the appendix to Winkenstern and Saur (2023).

We assume two spherical coordinate systems, (r, θ, ϕ) to describe the ocean's induced fields, and (r', θ', ϕ') for the reservoir's induction response, respectively. We introduce the transformation vector $\mathbf{r}_\mathrm{c} = (r_{\mathrm{c},x}, r_{\mathrm{c},y}, r_{\mathrm{c},z})$, which spans from Europa's center to that of the reservoir. As we align our reservoir with the x-axis in this study, $\mathbf{r}_\mathrm{c} = (r_\mathrm{c}, 0, 0)$. In Europa-centered Cartesian coordinates, we describe the surface of the reservoir with radius r_res as

$$\begin{aligned} x &= r_\mathrm{c} + r_\mathrm{res}\sin\theta\cos\phi \\ y &= r_\mathrm{res}\sin\theta\sin\phi \\ z &= r_\mathrm{res}\cos\theta, \end{aligned} \tag{D.56}$$

and, respectively, describe the ocean's surface with outer radius r_0 in reservoir-centered Cartesian coordinates as

$$\begin{aligned} x' &= -r_\mathrm{c} + r_0\sin\theta'\cos\phi' \\ y' &= r_0\sin\theta'\sin\phi' \\ z' &= r_0\cos\theta'. \end{aligned} \tag{D.57}$$

Afterward, we transform from Cartesian into spherical coordinates via

$$\begin{aligned} r &= \sqrt{x^2+y^2+z^2} \\ \theta &= \operatorname{atan2}(\sqrt{x^2+y^2}, z) \\ \phi &= \operatorname{atan2}(y, x), \end{aligned} \tag{D.58}$$

and calculate the ocean's induction response across the reservoir's surface using the potential description (Equation (3.31)). This induction response, however, is given in Europa-centered coordinates. For correct application, the radial component in reservoir-centered coordinates $B_{r'}$ is required, thus transforming the induced field as follows

$$\begin{aligned} B_{x'} &= B_r \sin\theta\cos\phi + B_\theta\cos\theta\cos\phi - B_\phi\sin\phi \\ B_{y'} &= B_r \sin\theta\sin\phi + B_\theta\cos\theta\sin\phi + B_\phi\cos\phi \\ B_{z'} &= B_r\cos\theta - B_\theta\sin\theta. \end{aligned} \tag{D.59}$$

Finally, we calculate the radial component via

$$B_{r'} = B_{x'}\sin\theta'\cos\phi' + B_{y'}\sin\theta'\sin\phi' + B_{z'}\cos\theta', \tag{D.60}$$

which is used in Equation (3.33) to calculate the external Gauss coefficients of the inducing field (q_l^m, s_l^m). Equation (D.60) can be derived analogously for the radial component of the reservoir's induction response across the ocean's surface.

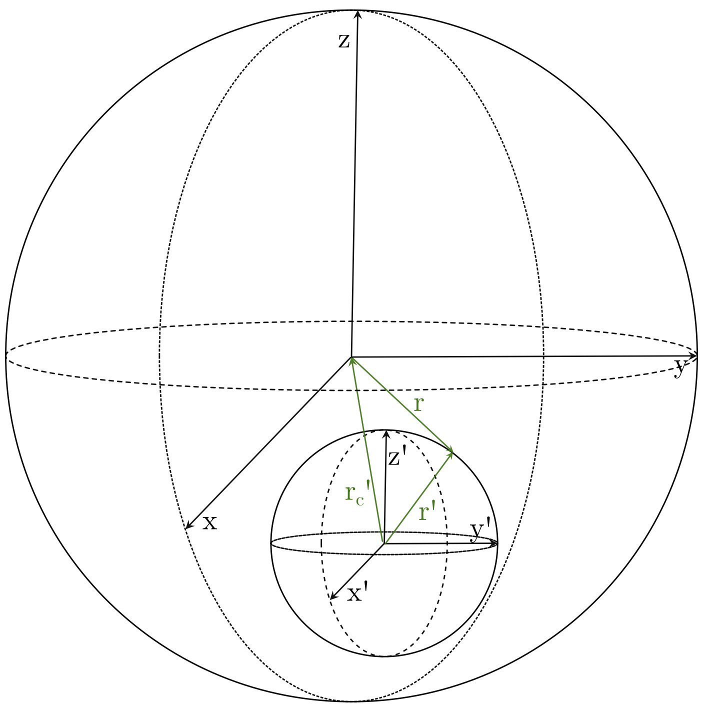

Figure D.1: Sketch of the two coordinate systems with origin in Europa's center (x, y, z) and with origin in the reservoir (x', y', z'), respectively. The scale and position of the reservoir are chosen arbitrarily. The green vectors visualize the transformation between the two systems.

E Flyby Discussion

The second part of the thesis pertains to the inversion of magnetometer (MAG) measurements recorded with the Galileo spacecraft, with the goal to characterize the properties of Europa's subsurface ocean. As such, we first ensure that the selected flybys are appropriate for a quantitative study of Europa's subsurface ocean. For that, flybys with an altitude larger than 1800 km at closest approach are filtered out (Schilling et al., 2004). At that altitude, Europa's induction response will decrease to less than 10% of its initial amplitude. This leaves the flybys E04, E12, E14, E19, and E26 (see Table E.1). The trajectories during these five encounters are given in Figure E.2.

Table E.1: Summary of Galileo flybys with existing MAG data. Altitude is given for closest approach with $R_{\mathrm{E}} = 1561$ km. Values for the magnetic latitude are from Schilling et al. (2004).

Flyby	Altitude [km]	Sys3 Long. [°]	Europa Lat. [°]	Mag. Lat. [°]
E04	696.1	156.8	-1.2	6.5
E11	2047.3	222.7	25.5	8.7
E12	205.0	117.7	-9.1	0.9
E14	1648.1	184.3	11.8	9.2
E15	2518.5	292.9	14.9	-0.5
E17	3586.4	139.9	-42.4	3.8
E19	1443.4	260.7	30.6	4.8
E26	347.4	2.3	-47.0	-9.5

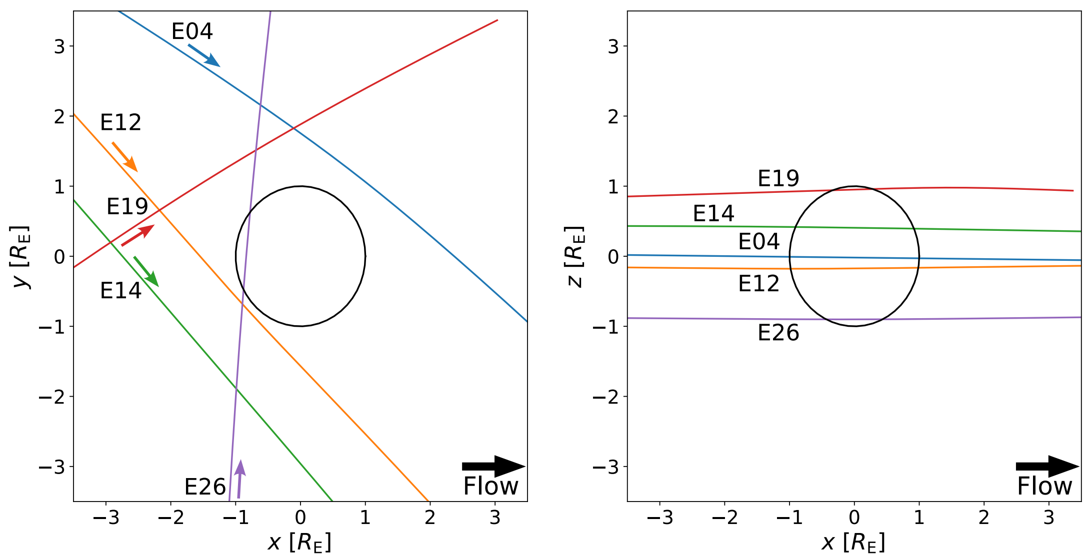

Figure E.2: Trajectories of the Galileo spacecraft in the xy-plane (left) and xz-plane (right) during its five closest encounters at Europa, namely E04 (blue), E12 (orange), E14 (green), E19 (red), and E26 (purple). Colored arrows indicate the direction of the spacecraft during the respective encounters.

E.1 The E12 Flyby

The E12 flyby occurred when Europa was situated close to the plasma sheet, resulting in strong plasma perturbations which obscure the ocean's induction response. In addition, this flyby has been identified as a putative plume crossing (Jia et al., 2018), further enhancing non-inductive magnetic field signatures. Figure E.3 shows the magnetic field measurements and the induction response of a perfectly conducting ocean with amplitude $A = 1$ and phase $\phi^{\mathrm{ph}} = 0$. Attributing any remaining perturbations to plasma interaction, we can see that these significantly outweigh the electromagnetic response of the ocean, with perturbations above 100 nT in all three components. While a domination of plasma interaction fields is expected in the B_z-component, given our inducing field is confined to the xy-plane and the flyby occurred near Europa's equatorial plane, the perturbations in the B_x and B_y-components overshadow the ocean's induction response and render this flyby unsuitable for our quantitative study of Europa's interior.

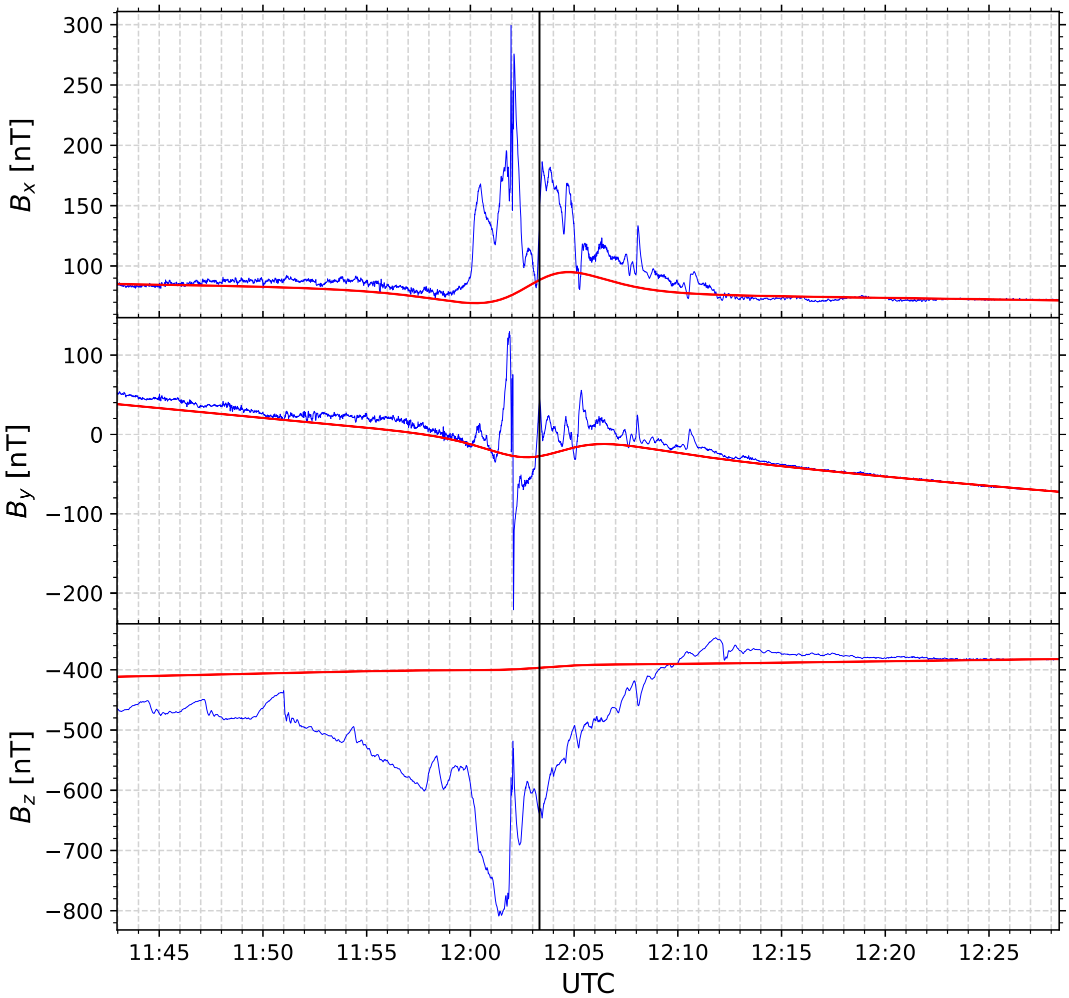

Figure E.3: Magnetic field measurements of the E12 flyby (blue) and the induction response of a perfectly conducting ocean with $A = 1$ and $\phi^{\mathrm{ph}} = 0$ (red). The vertical black line marks the closest approach.

E.2 The E26 Flyby

While Europa was well below the plasma sheet during the E26 flyby, it is also discussed to be a plume crossing (Arnold et al., 2019; Huybrighs et al., 2020; Jia et al., 2021), giving rise to large perturbations in all three components (Figure E.4), of which some appear on very local scales. Although the Galileo spacecraft made its closest encounters during the E12 and E26 flybys, the strength of the plasma magnetic field would result in a scenario, where the goodness of our fit to the observations is primarily controlled by our model for Europa's plasma interaction, rather than by the induced magnetic field and thus the properties of the ocean. It is for that reason that we do not consider an inversion of the measurements of these two flybys.

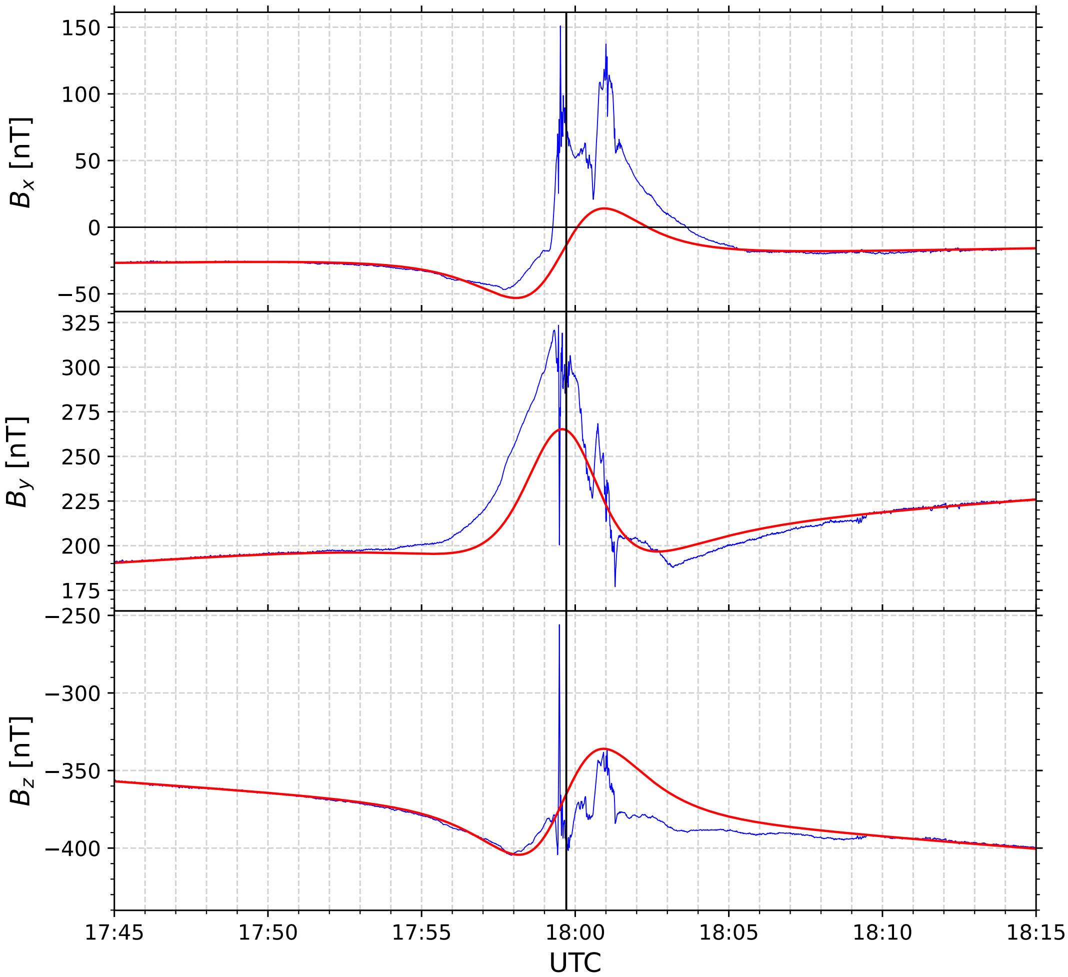

Figure E.4: Magnetic field measurements of the E26 flyby (blue) and the induction response of a perfectly conducting ocean with $A = 1$ and $\phi^{\mathrm{ph}} = 0$ (red). The vertical black line marks the closest approach.

E.3 The E04 Flyby

Of the five flybys discussed in this section, the E04 flyby was the only one where Galileo flew downstream of Europa, crossing its wake. In this region, plasma perturbations are particularly irregular compared to the upstream hemisphere (Figure E.5). While the ocean's induced magnetic field contributes significantly to the measured perturbation in the B_x and B_y-components, small-scale fluctuations appear to be particularly strong during the E04 flyby, compared to measurements during other flybys. While we do not present the E04 flyby in our primary results, we do apply our method to these measurements in Section 5.3.3 to assess how such fluctuations not accounted for in our model description affect our analysis.

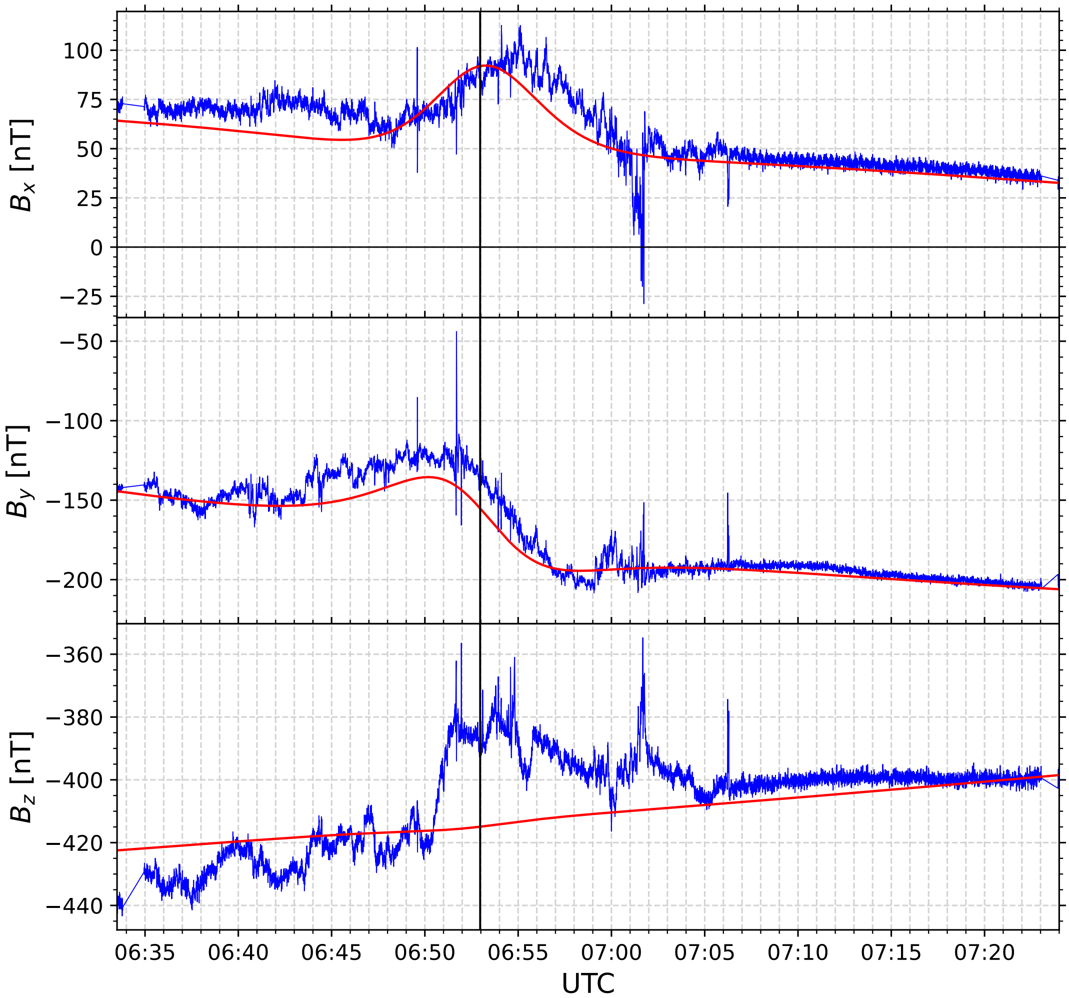

Figure E.5: Magnetic field measurements of the E04 flyby (blue) and the induction response of a perfectly conducting ocean with $A = 1$ and $\phi^{\mathrm{ph}} = 0$ (red). The vertical black line marks the closest approach.

E.4 The E19 Flyby

The E19 flyby occurred at a System III longitude of $\lambda_{\mathrm{III}} = 260.7°$. Here, the inducing field is comparably weaker than during, e.g., the E04 or E14 flyby. Furthermore, the E19 flyby has the second largest C/A altitude with 1443.4 km. This results in a faint induction response with an amplitude of approximately 10 at the spacecraft's position (Figure E.6). Furthermore, the magnetometer stopped recording around 20 minutes after closest approach. The lack of measurements well after C/A could complicate the fitting of the Jovian background field. Thus, we decide to exclude the E19 flyby from our analysis.

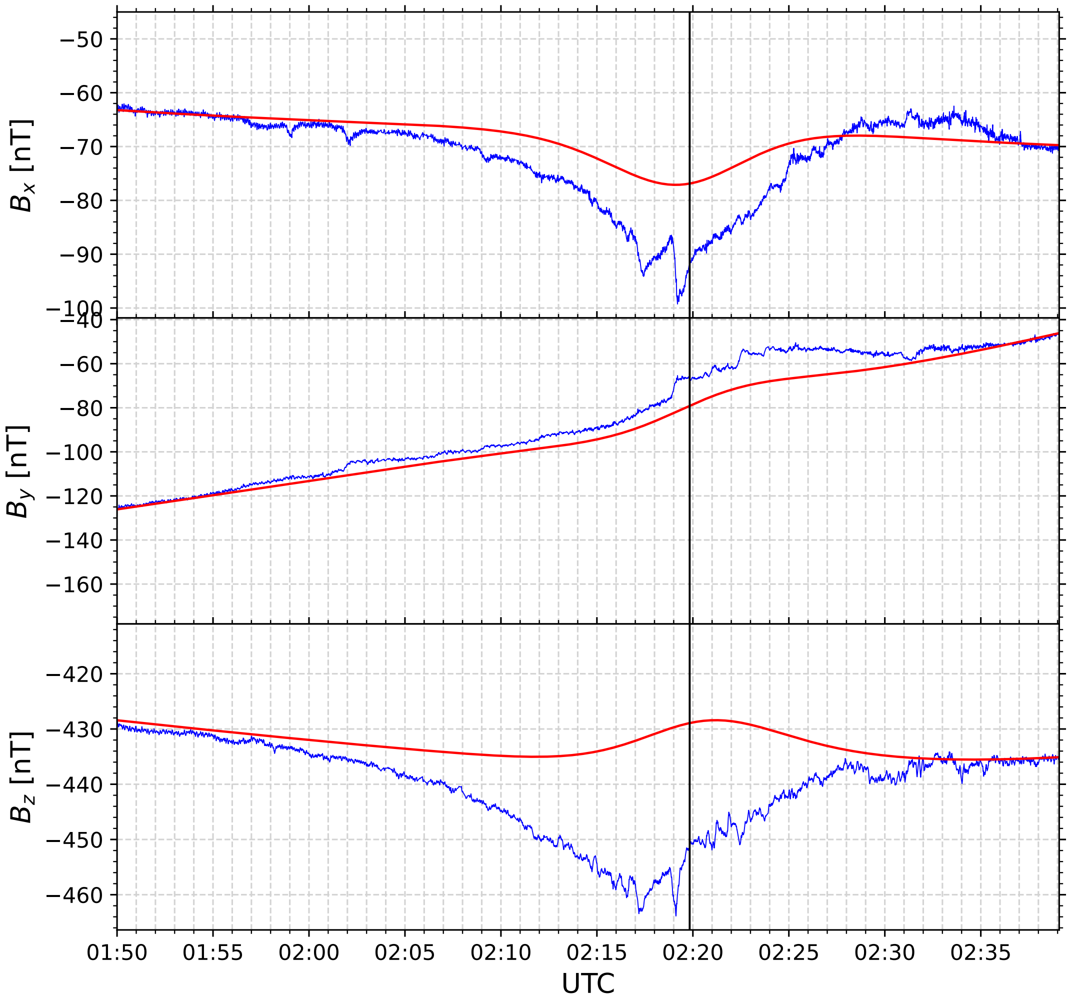

Figure E.6: Magnetic field measurements of the E19 flyby (blue) and the induction response of a perfectly conducting ocean with $A = 1$ and $\phi^{\mathrm{ph}} = 0$ (red). The vertical black line marks the closest approach.

Data Availability Statement

This thesis discussed and analyzed magnetic field measurements recorded with the Galileo spacecraft. These measurements are archived in the Planetary Data System: Planetary Plasma Interactions node both in high resolution (Kivelson et al., 2024a), and low resolution (Kivelson et al., 2024b). Measurements were downloaded in SYS3 coordinates and then transformed to EPhiO. The source code to solve the coupled induction response is publicly available in a repository (Winkenstern, 2023).

Acknowledgements

First and foremost, I like to thank Joachim Saur for his mentorship and supervision. The work across the last four years would not have been possible without his ideas and thought-provoking questions. Further thanks go to my colleagues at the institute for the interesting discussions and fun times during social activities - a particular mention goes to Stephan Schlegel, Filip Elekes, and Anne-Cathrine Dott. I also thank Stephan Schlegel, Wiebke Mörbe, and Isabelle Heßelmann for proofreading my thesis and their insightful comments. Thanks to Sebastian Cervantes for carrying out the MHD simulations required in my final study, as well as his comments on the respective manuscript.

I wish to thank the European Research Council, who funded the project under the grant agreement number 884711. I also acknowledge the computing resources of the Deutsches Klimarechenzentrum (DKRZ), granted by its Scientific Steering Committee (WLA) under project ID 1350. I also thank Karin Boessenkool and the Graduate School of Geosciences, who not only helped to work through the administrative side of being a PhD student, but also provided helpful advice in stressful times. Additionally, I would like to thank Kurt Retherford for the opportunity to be involved with the Europa Clipper mission.

Wholeheartedly, I express my gratitude to my friends for their continuous support throughout the last years. As rough as some days or weeks may have been, these people reminded me to never give up and keep moving forward.

Without everyone mentioned here, this journey would not have been possible, and for that I am forever grateful.

Erklärung zur Dissertation

Hiermit versichere ich an Eides statt, dass ich die vorliegende Dissertation selbstständig und ohne die Benutzung anderer als der angegebenen Hilfsmittel und Literatur angefertigt habe. Alle Stellen, die wörtlich oder sinngemäß aus veröffentlichten und nicht veröffentlichten Werken dem Wortlaut oder dem Sinn nach entnommen wurden, sind als solche kenntlich gemacht. Ich versichere an Eides statt, dass diese Dissertation noch keiner anderen Fakultät oder Universität zur Prüfung vorgelegen hat; dass sie - abgesehen von unten angegebenen Teilpublikationen und eingebundenen Artikeln und Manuskripten - noch nicht veröffentlicht worden ist sowie, dass ich eine Veröffentlichung der Dissertation vor Abschluss der Promotion nicht ohne Genehmigung des Promotionsausschusses vornehmen werde. Die Bestimmungen dieser Ordnung sind mir bekannt. Darüber hinaus erkläre ich hiermit, dass ich die Ordnung zur Sicherung guter wissenschaftlicher Praxis und zum Umgang mit wissenschaftlichem Fehlverhalten der Universität zu Köln gelesen und sie bei der Durchführung der Dissertation zugrundeliegenden Arbeiten und der schriftlich verfassten Dissertation beachtet habe und verpflichte mich hiermit, die dort genannten Vorgaben bei allen wissenschaftlichen Tätigkeiten zu beachten und umzusetzen. Ich versichere, dass die eingereichte elektronische Fassung der eingereichten Druckfassung vollständig entspricht.

Teilpublikationen:
Winkenstern, J., & Saur, J. (2023). Detectability of local water reservoirs in Europa's surface layer under consideration of coupled induction. Journal of Geophysical Research: Planets, 128 (10), e2023JE007992

29.11.2024, Jason Winkenstern